# Circumferential Three-Dimensional Profiling with Specular Micro-Texture Photometry for Dark Objects

Mengyu Song

Dissertation submitted to the Faculty of the
Virginia Polytechnic Institute and State University
in partial fulfillment of the requirements for the degree of

Doctor of Philosophy
in
Mechanical Engineering

Tomonari Furukawa, Chair
John Ferris
Pinhas Ben-Tzvi
A. Lynn Abbott

May 19, 2020
Blacksburg, Virginia

Keywords: Visual-based Measurement, Micro-texture Profiling, Photometric Stereo,
Circumferential 3D Profiling

# Circumferential Three-Dimensional Profiling with Specular Micro-Texture Photometry for Dark Objects

Mengyu Song

(ABSTRACT)

This dissertation proposes a novel approach to achieve circumferential three-dimensional (3D) profiling for dark objects by investigating specular micro-texture protometry. A small patch of a target surface in micro-texture level yields different appearance under different illumination. This photometric property can be used to reconstruct the target surface with pixel-level resolution. However, due to the nature of some material, the surface of whom has stronger specular components than diffuse components, making the usage of general micro-texture photometry more difficult. On the other hand, without using micro-texture photometry, the conventional circumferential 3D approaches only utilizes the geometric property of the target surface, compared to which, the proposed is able to reconstruct the target surface with finer detail.

The original contributions of this dissertation are threefold. To begin with, the specular component in the micro-texture photometry is investigated to propose the pixel-level 3D profiling. The intensities of the same pixel from different images, which are taken under different lighting conditions are different. The specular components are used to recover the surface normal of the corresponding surface patch of the target surface. Consequently, the proposed specular-photometry-based technique produces pixel-wise measurement on surface normal.

Furthermore, the conventional circumferential 3D profiling approach is extended with the

proposed specular-photometry-based technique. The result of 3D profiling via the conventional approach is sparse due to its nature. On the other hand, the result of 3D profiling from the integration using the surface normal obtained from the proposed specular-photometry-based technique suffers from accumulative error. A new approach is then proposed to use the result from the conventional approach as global constraint, for the purpose of reducing the accumulative error. The proposed approach is able to achieve pixel-resolution globally bounded profiling because of the dense surface normal measurement from the proposed specular-photometry-based technique and the constraints from the conventional approach. Lastly, a system is developed to apply the proposed circumferential specular-photometry-based 3D profiling approach. The developed system is not only able to acquire data and but also to provide different lighting conditions for both the specular-photometry-based technique and conventional approach using a digital single-lens reflex camera and different lighting devices. With a step motor to rotate the object for three hundred and sixty degrees, the system is able to achieve circumferential scanning.

# Circumferential Three-Dimensional Profiling with Specular Micro-Texture Photometry for Dark Objects

Mengyu Song

(GENERAL AUDIENCE ABSTRACT)

This dissertation explains a novel approach to fulfill circumferential 3D profiling with high resolution for dark objects. With the proposed approach, the resolution is able to achieve micro-texture level. The high resolution measurement is achieved by investigating specular micro-texture photometry. As for dark objects, the specular components dominate the reflection. The usage of photometry is explained as follow. A small patch of a target surface yields different appearance under different illumination. For the material of the surface of dark objects, the surface reflects stronger specular components than diffuse components. The proposed approach utilizes this photometric property to recover the small patch's surface normal using its specular components. The recovered surface normal is then used to calculate the surface profile through integration. The conventional circumferential 3D profiling approach, which can only produce low-resolution measurement, is also adopted in the proposed approach to enhance its performance, as the integration method suffers from accumulative error. The result from the conventional approach serves as a global constraint to bound the final profiling result. A system is developed to apply the proposed circumferential specular-photometry-based 3D profiling approach, which is equipped with a step motor to rotate the object for three hundred and sixty degrees for the purpose of circumferential scanning. A series of numerical and experimental studies were conducted to validate the performance of the proposed approach. As it is shown in the result, the proposed approach is able to measure the tire tread with 31$\mu$m resolution.

# Dedication

*This dissertation is dedicated to my parents. Without them, I could not even start what I am pursuing.*

# Acknowledgments

There are many people that I want to thank for their contribution to my graduate life. Without them, this dissertation would not have been possible. Firstly, I would like to express my sincere gratitude to my advisor, Prof. Furukawa, for his generous support of my graduate study. He has been a tremendous mentor for me with his knowledge, patience and enthusiasm about research. I am also indebted to Prof. Ferris, Prof. Ben-Tzvi and Prof. Abbott, for their services as my advisory committee. Their suggestions has brought new horizons on my work. Finally, I would like to thank my fellow lab mates and friends in Virginia Tech for their great company, including Boren, Murat, Yazhe, Tian, Hangxin, Yoon, Rich, Chris, Kuya, Orson, Affan, Luan, Josiah, Mickey, Urvi, Diya, Jihong, Jeeseop, Ash, George, Abdullah, David, Phil, Spencer, Ioannis, Tamer, Monir, Cong, Yoshi, Peter, Cameron, Jonathan, Dean, Mingyi, Dewei and Yuantao.

# Contents

# List of Figures

# List of Tables

# Chapter 1

# Introduction

Nowadays, high resolution cameras are used to observe objects, obtaining finely-detailed images, with each pixel contains the information of the pixel-corresponding small patch of the object, in micro-texture level. The information, from the point of view of photometry, reveals the objects' geometric shape. For the material of dark objects, due to its photometric nature, the specular components are stronger than the diffuse components, making its photometric properties difficult to be utilized from a conventional photometry point of view. As from a photometry viewpoint, the appearance of an object depends not only on its geometric shape but also its photometric properties. Which means, under different illumination, the same object exhibits different appearance.

This dissertation presents a comprehensive study about circumferential three-dimensional (3D) profiling by investigating the specular components of the protemetry at micro-texture level. The surface gradient is recovered first with photometry-based technique. The surface profile is then recovered with the obtained surface gradient map with the assistance from the conventional circumferential 3D profiling approach. Difference from the conventional approach, the proposed approach enables the pixel-level profiling with micro-texture resolution and enhances accuracy. In this chapter, the background leading up to the recent interest in circumferential 3D profiling and the current state of knowledge are briefly reviewed first. The primary objectives of this dissertation are then given, along with the approach proposed to achieve the objectives. The original contribution are summarized next, followed by the

list of publications arising from the author during his graduate study. The contents of this dissertation are outlined last in this chapter.

## 1.1 Background

The process of digitizing the shape of real-world objects into a computer understandable code is referred to as 3D profiling. Circumferential 3D profiling is able to generate a full scan data of an object for objects with cylindrical shape. Recent years have witnessed increasing interest in the applications of circumferential 3D profiling. With the popularity of 3D printing into domestic market, a quick data acquisition tool for whole body scan become handy and even necessary for the users. Meanwhile, for the antique industry, a touch-free method to obtain a fine scan of the relief on an antique vase could benefit in a lot ways, such as virtual display, scientific analysis and aesthetic evaluation. It can also be used for industrial inspection. An image-based crankshaft balancing system, which was developed in 2015, displayed the potential of replacing traditional electromechanical systems, which would further improve automation manufacture.

As a specific application of circumferential 3D profiling, tire tread profiling receives a lot attention in the tire society. The shape of the tire tread is important and worth investigating. It can be used for the study of vehicle dynamic analysis when combined with road 3D profiling. With the 3D fine data at micro-texture resolution, the analysis result becomes more realistic and closer to the situation in real world. The scan of circumferential tire tread can also be used in reverse engineering to study the design and performance of a certain tire pattern. Tire wear measurement can also be achieved by comparing before and after profile of the same tire during a tire wear test. With high level of detail of the tire tread, the digital model can also be used to predict the behavior of the tire during its service life. Therefore,

the development of a circumferential 3D profiling system for dark objects with micro-texture resolution is of great significance.

## 1.2 Objectives

The primary objectives of this dissertations are listed as below:

1. To propose an approach for circumferential 3D profiling with micro-texture resolution.
2. To propose an approach to deal with dark surfaces of objects such as tire from a photometric point of view.
3. To develop a system that is capable to apply the proposed micro-texture circumferential 3D profiling approach.

## 1.3 Proposed Approach

In order to achieve these objectives, techniques based on Photometric Stereo (PS) and Laser Section (LS) are investigated to develop a new approach to reconstruct a target surface in micro-texture scale. The drawbacks of the two techniques are compromised in the proposed approach as LS technique is not capable to produce dense measurement while PS technique suffers from accumulative error due to lack of global constraint. In the proposed approach, LS technique is applied to generate a sparse 3D point cloud to represent the surface of target surface. The 3D point cloud is then used to provide a global constraint when applying PS-based surface normal integration for 3D profiling. As conventional PS technique fails on material of dark objects such as tire due to the violation of the Lambertian assumption, Specular Photometric Stereo (SPS) technique is proposed to generate surface normal

for such materials. SPS technique utilizes the specular components to recover the surface normal with pixel by pixel, similar to conventional PS technique, yielding a surface normal measurement with pixel resolution. A system with one high resolution camera and multiple lighting devices, including a laser line generator and sixteen LEDs is developed to apply the proposed approach. A step motor and an encoder are equipped to the system to achieve the circumferential measurement, with the step motor rotating the scanning object and the encoder recording the angular position for each scan.

## 1.4 Principal Contributions

The contributions of this dissertation are threefold:

1. The conventional circumferential 3D profiling approach is used to enhance the 3D profiling using the proposed specular-photometry-based technique. The proposed approach is able to achieve pixel-resolution globally bounded profiling because of the dense surface normal measurement from the proposed specular-photometry-based technique and the constraints from the conventional approach.

2. The specular micro-texture photometry is investigated to propose the pixel-level 3D profiling to develop SPS. The intensities of the same pixel from different images, which are taken under different lighting conditions, are used to recover the surface normal of the corresponding surface patch of the target surface. Consequently, the proposed specular-photometry-based technique produces pixel-wise measurement of surface normal.

3. A system is developed to apply the proposed circumferential specular-photometry-based 3D profiling approach. The developed system is not only able to acquire data

and but also to provide different lighting conditions for both the specular-photometry-based technique and conventional approach using a digital single-lens reflex camera and different lighting devices.

## 1.5 Publications

To date, the graduate work of the author has been summarized into the following publications:

- Mengyu Song and Tomonari Furukawa. Specular photometric stereo for surface normal estimation of dark surfaces. In *Science and Information Conference*, pages 619–637. Springer, 2019

- Mengyu Song, Tomonari Furukawa, Boren Li, and Notomi Shinya. A system for measuring microscopic tire wear using hybrid photometric stereo / light section method. In *JSAE*, 2018

- Mengyu Song, Cong Chen, Tomonari Furukawa, Azusa Nakata, and Shibata Shinsuke. In-crash toeboard deformation measurement towards active crash control. In *Fast Zero*, 2019

- Mengyu Song, Tomonari Furukawa, and Notomi Shinya. High-resolution circumferential tire tread three-dimensional profiling using laser section method and photometric stereo method. *SAE International Journal of Commercial Vehicles*, 1(1):1–26, 2020

- Mengyu Song, Cong Chen, Tomonari Furukawa, Azusa Nakata, and Shinsuke Shibata. A sensor suite for toeboard three-dimensional deformation measurement during crash. *Stapp Car Crash Journal*, 63:331–342, 2019

- Mengyu Song, Cong Chen, Tomonari Furukawa, and Azusa Nakata. In-crash toeboard deformation measurement in vehicle crash tests with recursive estimation. *International Journal of Crashworthiness* (submitted)

- Cong Chen, Mengyu Song, and Tomonari Furukawa. Three-dimensional measurement of crash test frame deformation using high speed camera fusion and motion model. In *JSAE*, 2019

- Cong Chen, Mengyu Song, Tomonari Furukawa, Azusa Nakata, and Shibata Shinsuke. Automobile structure three-dimensional deformation measurement during crash using multi-camera vision. In *Fast Zero*, 2019

- Cong Chen, Mengyu Song, Tomonari Furukawa, Azusa Nakata, and Shinsuke Shibata. Rnn based online automobile deformation measurement for active safety. In *Fast Zero*, 2019

## 1.6 Organization

This disseration is organized as follows:

- Chapter 2 presents literature review of past work on related topics including: vision-base 3D profiling, circumferential profiling and photometry-based techniques.

- Chapter 3 explains the established work on circumferential 3D profiling. LS-based approach and photometry-based technique are formulated in this chapter.

- Chapter 4 presents the proposed circumferential 3D profiling with specular micro-texture photometry with pre-processing step and main processing step.

- Chapter 5 presents the proposed specular photometry-based surface normal recovery technique with mathematical derivation and experimental validation.
- Chapter 6 explains the developed system for applying the proposed approach for circumferential 3D profiling. Calibration procedures of the developed system are also introduced in this chapter.
- Chapter 7 presents the experimental results to validate the performance of the proposed approach and the developed system.
- Chapter 8 summarizes this dissertation and proposes direction for future work.

# Chapter 2

# Review of Literature

This chapter reviews past work regarding related topics of this dissertation from previous literature. Vision-based 3D profiling approaches are first reviewed, followed by a more specific investigation into the field of circumferential 3D profiling, which is further developed into the investigation of tire tread 3D profiling. Past works aiming at applying photometry for 3D profiling are given in the last section.

## 2.1 Vision-based 3D Profiling

3D profiling is the process of capturing the shape and appearance of real objects. It can be used either to get the 3D profile of an object or to know the 3D coordinates of any point on the profile. Applications of 3D profiling including: 1. reverse engineering for rapid prototyping ([55], [89]), shape analysis ([50], [61]) or virtual reality ([78], [9]), 2. 3D modeling for scientific purpose such as 3D particle tracking in PIV (particle image velocimetry) ([57], [62]), 3. industrial defect detection, such as crack detecting for building assessment ([56], [83]) and defect detection for automobile parts ([43], [63]). Vision-based 3D profiling is to obtain the geometric shape of real objects using visual information and is a significant research topic with increasing practical demand in industry [65].

Structured light is one of the widely used approach for 3D profiling [68]. By using light pattern with well-designed pattern, this approach can achieve 3D measurement with only

one camera [20]. Structured light is considered as on of the most reliable techniques to get the objects' profiles, with reasonable accuracy and resolution [69]. LS-based approach, which is a special case of structured light, uses diffracted laser beams and a camera as a transmitter and a receiver respectively [85]. A laser line pattern was projected on a public road surface to get the shape of the road for the purpose of the detection of pothole on the road pavement [97]. A similar approach was used to reconstruct the shape of sea floor to model the acoustic back-scatter from the sea floor [88]. In [87], an LS method and a stereo vision method were fused to obtain detailed 3D road surface data for the characterization of road pavement textures. The LS method can measure 3D surfaces effectively without a complex system. It however has a limited resolution as the transmitted laser beams are finite. Recent years have seen various applications of LS based measurement, for as large as terrestrial scan [19] or as small as microprofilometry for medical inspection [35].

PS based 3D profiling, which uses the observation of the same object from the same viewpoint under different lighting conditions, have also been deployed in various 3D profiling. Li and Furukawa [47] measured road profiles with accuracy in the order of 10 $\mu$m. Hansen, et al. [24] applied it to 3D face reconstruction. Ackermann, et al. [1] reconstructed the shape of the outdoor buildings using the fact that outdoor buildings have different shading appearances under the sun illumination from different angles at different time. Logothetis, et al. [52] combined PS and multi-view vision and created a high quality volumetic reconstruction of objects. The great advantage of the PS is the fine pixel resolution. The PS is however a method for surface normal identification and is thus subject to integration errors in 3D profiling. The surface normal identification could be directly used in surface defect detection [66], which is also an outcome of 3D profiling.

## 2.2 Circumferential 3D Profiling

Most 3D profiling technique can only partially measure the shape of the target object, as the device only faces one side of the object. For a cylindrical object, it is essential to have a circumferential measurement. The previous work of circumferential 3D profiling can be classified into two major categories.

In the first category, 3D measurement techinque is combined with a turntable technique, where the rotation of the scanning object is obtained through the rotation device itself. Line scanning technique was first combined with the turntable technique to compromise its inefficiency on scanning whole objects ([44], [79]). Taubin et al. rotated the laser instead of the object, but applied a similar approach for circumferential 3D profiling [81]. The line scanning technique can get a cross section profile precisely, but low resolution along object moving direction makes the scanning process long. On the contrary, area scanning technique is applied to have fast data acquisition. Fitzgibbon et al. proposed an automatic 3D model construction for turn-table sequences, and tested in virtual environment [18]. Park and Subbarao used the turntable technique combined with stereo vision measured several real objects [59]. Structured light was used by multiple researchers and achieved circumferential 3D profiling ([39], [99], [98]). Hernadez et al. first applied PS technique to get a whole circumferential 3D profiling [26].

The second category utilizes the concept of point registration technique, ([82], [17], [45], [58]). Fringe projection technique, which uses one projector to project a pre-calibrated fringe pattern to the scene, and one camera to observe the appearance of the distortion of the fringe from a different viewpoint, is combined with Iterative Closest Point (ICP) technique ([36]) to register multiple scanning data without prior knowledge on the motion of scanning device. Similar approach can be used for other area scan techniques [95]. The advantage of ICP based

registration technique is that for software-based alignment, it is calibration-free technique, making the system easy to setup and alignment. So that it can be adepted to portable system. But due to the low resolution of most area scanning technique, the resolution and accuracy of such systems are low in general, and for scenes of simple and repeated textures, ICP is prone to fail.

## 2.3 Tire Tread Profiling

High resolution circumferential 3D profiling for objects with complex surface by a fast non-contact method is urgently demanded, especially in the field of industrial inspection [34]. The 3D profiling of tire tread, for example, has been explored for the purpose of tire performance analysis ([8], [46]), tire tread pattern design ([91],[22]), high resolution tire wear measurement ([30], [51]) and so on. The 3D tire data can be also used to study the tire-terrain interaction with finite element method (FEM), for the purpose of vehicle dynamic stability analysis ([80], [49]).

Tire tread is consisted of grooves, sipes and blocks with complex pattern to ensure the safety and stability of a wheeled vehicle. The acquisition of high resolution 3D tire tread data has been delved into two categories by previous researchers. Contact methods such as the ones described in [10] and [42] were first developed for the purpose of tire tread measurement. A contact probe is used for point measurement of the groove depth. Computer vision and laser measurement methods then started to be applied for contact-less data acquisition [90]. Huang et al. [31] applied stereo vision algorithm to measure the shape of tire tread and achieved $1mm$ accuracy in depth measurement. Coe, et al. [15] developed a Time-of-Flight (TOF) measurement method using laser. While the computer vision method excels in achieving high horizontal resolution, the TOF measurement method can achieve high resolution in vertical

depth measurement. Simulated tire surface with detailed tread block has been developed for tire analysis to overcome the poor analysis quality resulted from over-simplified models ([14]).

## 2.4 Photometry-based Techniques

Photometric Stereo (PS), originally introduced by Woodham [92], uses multiple digital images taken from one viewpoint but under different lighting conditions to determine surface's orientation. Originally, PS has a strong assumption on the reflection property of the concerned surface. By inversing the diffuse reflection model and image formation, surface normal can be solved mathematically. Different from conventional PS, Specular Photometric Stereo uses the specular components from the reflection of a dark surface, which violates the Lambertian assumption of PS. The surface of materials like rubber has a low diffuse albedo but a wide specular reflection region, which provides information cue to recover its shape.

Point lighting sources were used in conventional photometric stereo method (Diffuse Photometric Stereo (DPS), [47]). Lambertian reflection model was assumed for DPS so that the image formation procedure could be reversed linearly, easing the procedure of obtaining numerical solutions. However, it also restricts the application of DPS. To apply DPS on complex reflection surface, violation of Lambertian assumption needs to be dealt with, and the ways to handle the non-Lambertian effects can be separated into 3 categories.

To begin with, early researches made the assumption that non-Lambertian effects appears in real world scene but with only rarely and can be treated as outliers through comparison with the majority of the observations. Three lighting sources are necessary for PS to recover a surface normal while four were used by Coleman Jr and Jain, so that the algorithm could choose the optimal three out of the four lighting sources while reject the one which seems

to violate the Lambertian assumption most [16]. Miyazaki et al. used a median criteria to reject surface normal candidates calculated by all combination of three lighting sources were rejected based on in , so that only inliers contributes to the calculation [54]. As the number of lighting sources increases, more complex statistical tools were used for outlier rejection. Hernandez et al. developed A RANSAC (random sample consensus) scheme to determine the three inliers [27], EM (Expectation Maximum, [94]), ML (Maximum Likelihood, [86]), Max-FS (maximum feasible subsystem, [96]) were also employed in previous research.

A large amount of research uses more complex parameterized reflection model and is also devoted to recover the reflectance parameters. Parametric PS can provide more accurate numerical result. DPS is widely utilized due to its ease of computation. Extending DPS from Lambertian reflectance model to a complex reflectance model introduces a high non-linearity. The main trend to deal with complex reflection surfaces is to fit a parameterized reflection model [53]. For example Georghiades used Torrance-Sparrow model [21] and Ruiters and Klein used Cook-Torrance model [67], Due to the existence of specular components, the parameterized reflection model is highly non-linear. Solving for its parameters, which include the surface orientation, requires a non-linear regression approach and a good initial guess of all the parameters [23]. Instead of using complex nonlinear reflection model, dichromatic reflectance model (DRM, [70]) was applied by Li and Furukawa [48]. DRM employs the difference of chromaticity between the lighting source and the reflecting surface to separate specular components from diffuse components in the reflection light. It has been proved to be effective for regular surfaces. But for dark surfaces, whose diffuse albedo is small, the separation of reflecting surface's chromaticity using the image from a digital camera contains a large error, resulting in an unsound reflection components decomposition.

Due to the high computational cost of parametric methods, research working towards non-parametric solutions has been fulfilled. Horn used an reference object with similar material

and known geometry (normally as a sphere) and it was observed together with the target object under the same illumination conditions. The surface normal of the target object can be obtained based on the similarity of appearance between the target object and the geometry-known example object [29]. The work was later extended to unknown lighting environments and color images ([84], [28]). Instead of having one reference object, Alldrin et al. assumed that the reflection function of all material can be considered as a linear combination of the reflection functions of some basis materials in their paper. With known the reflection functions of the basis materials, the surface normal can be easily solved by calculating the weights for those basis materials [2].

When the diffuse reflection is insufficient, specular components can also provide useful visual cue for image-based algorithms ([40], [41]). Blake and Brelstaff applied two cameras to observe a specular surface under point illumination, and used the position of specular highlight to determine the surface's curvature properties [5]. Ikeuchi employed a Lambertian board to extend a point lighting source to a plane lighting source to illuminate a mirror-type surface. By changing the position of the point lighting source, the lighting condition on the specular surface from the extended lighting source changes accordingly, therefore the surface's orientation was able to be determined [32]. Both cases assumed a narrow specular reflection region, which is valid for surfaces of mirror-like material, like metal. However, this approach cannot be utilized directly on dark surfaces of material like rubber, for its wide specular reflection region.

## 2.5 Chapter Summary

The chapter has presented the extensive efforts of previous researchers in their state-of-the-art investigation to the topics covered in this dissertation. Four topics have been reviewed.

Visual-based 3D profiling approaches were first investigated, followed by more and more specific topic, which are circumferential 3D profiling and tire tread 3D profiling. The state-of-the-art research on photometry-based 3D profiling was explored at last.

# Chapter 3

# Circumferential 3D Profiling and Photometry-based 3D Profiling

In this chapter, the established work from previous research is summarized to provide fundamental base to describe the original contributions of this dissertation. The concept of visual-based circumferential 3D profiling for cylindrical objects is introduced first. The fundamental of the conventional approach, LS technique-based approach, is then explained in detail. The general photometry-based 3D profiling technique is established in the last section of this chapter.

## 3.1 Circumferential Profiling

### 3.1.1 Representation of Cylindrical Objects

Figure 3.1(a) shows an example of cylindrical objects, which is a tire. Parametric equations tend to be the most accurate way to represent the continuous surface. However, due to the complexity of most real-world objects, it is difficult, or even impossible to find the exact parametric equations to the surface shape. Discrete representation, on the other hand, can be used to satisfy different requirement in terms of resolution. Figure 3.1(b) shows the point-cloud representation of the tire tread in a Cartesian coordinate system (CS). $\{E\}$ is used to

represent the Cartesian CS. It is noted that $\{E\}$ is randomly chosen, with its orientation and origin unspecified. Notice the color of a point of the point cloud is defined on the distance from the object center axis to the point.

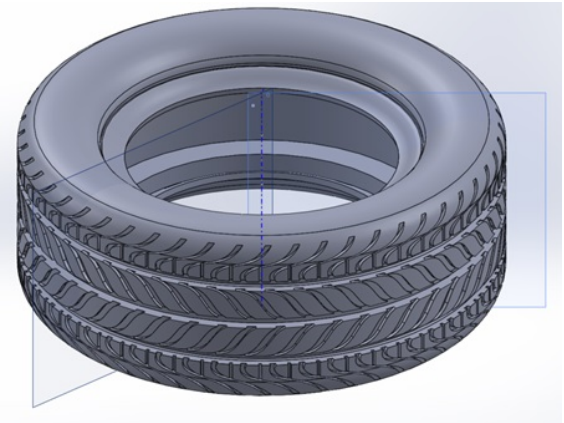

(a) Example of cylindrical object

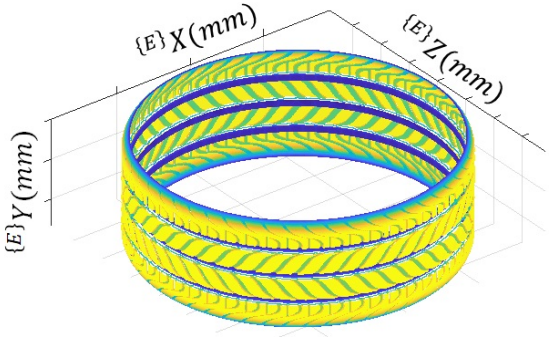


(b) Point cloud representation in a Cartesian CS

Figure 3.1: Point cloud representation of a cylindrical object in Cartesian CS

Figure 3.2 shows the conversion from the Cartesian CS $\{E\}$ to a Cylindrical CS $\{T\}$. A rotation axis is defined in $\{E\}$ by a unit vector ${}^{\{E\}}\bar{\boldsymbol{v}}$ and a point ${}^{\{E\}}\boldsymbol{C}$. Then the conversion from the Cartesian coordinates ${}^{\{E\}}\boldsymbol{P} = \left[{}^{\{E\}}X, {}^{\{E\}}Y, {}^{\{E\}}Z\right]^\top$ to Cylindrical coordinates $\left[{}^{\{T\}}r, {}^{\{T\}}\theta, {}^{\{T\}}z\right]^\top$ is formed using ${}^{\{E\}}\bar{\boldsymbol{v}}$ and ${}^{\{E\}}\boldsymbol{C}$ as:

$$
\begin{aligned}
{}^{\{T\}}z &= \left({}^{\{E\}}\boldsymbol{P} - {}^{\{E\}}\boldsymbol{C}\right) \cdot {}^{\{E\}}\bar{\boldsymbol{v}} && \text{(3.1a)}\\
{}^{\{T\}}r &= \left|{}^{\{E\}}\boldsymbol{P} - {}^{\{E\}}\boldsymbol{C} - {}^{\{T\}}z\,{}^{\{E\}}\bar{\boldsymbol{v}}\right| && \text{(3.1b)}\\
{}^{\{T\}}\theta &= \arccos \frac{\left({}^{\{E\}}\boldsymbol{P} - {}^{\{E\}}\boldsymbol{C} - {}^{\{T\}}z\,{}^{\{E\}}\bar{\boldsymbol{v}}\right) \cdot \left({}^{\{E\}}\boldsymbol{P}_0 - {}^{\{E\}}\boldsymbol{C} - {}^{\{T\}}z_0\,{}^{\{E\}}\bar{\boldsymbol{v}}\right)}{\left|{}^{\{E\}}\boldsymbol{P} - {}^{\{E\}}\boldsymbol{C} - {}^{\{T\}}z\,{}^{\{E\}}\bar{\boldsymbol{v}}\right| \left|{}^{\{E\}}\boldsymbol{P}_0 - {}^{\{E\}}\boldsymbol{C} - {}^{\{T\}}z_0\,{}^{\{E\}}\bar{\boldsymbol{v}}\right|} && \text{(3.1c)}
\end{aligned}
$$

where ${}^{\{E\}}\boldsymbol{P}_0 = \left[{}^{\{E\}}X_0, {}^{\{E\}}Y_0, {}^{\{E\}}Z_0\right]^\top$ is a point at ${}^{\{T\}}\theta = 0$, and ${}^{\{T\}}z_0$ is the corresponding depth coordinate in $\{T\}$ for $\boldsymbol{P}_0$.

Figure 3.3(a) shows the conversion result of one cross section. Figure 3.3(b) shows the 3D representation of the Cylindrical coordinates of the whole surface. Figure 3.3(c) shows

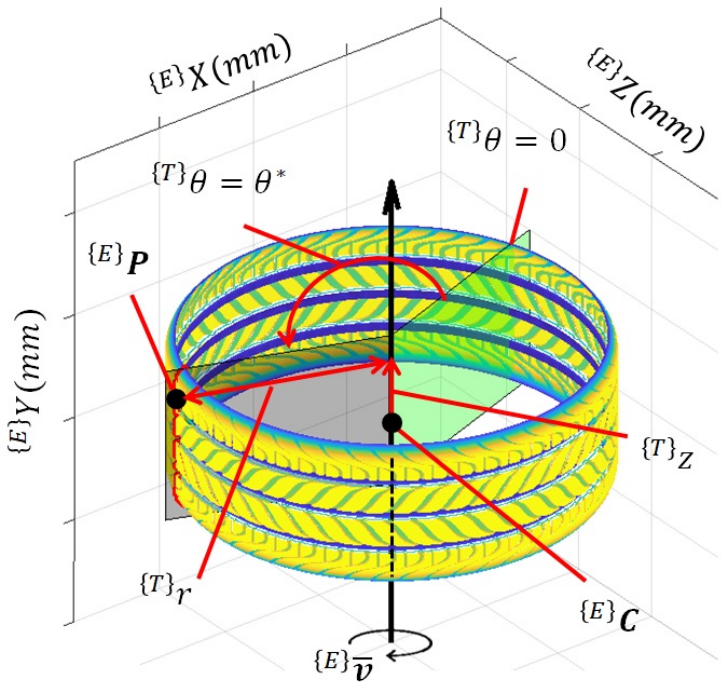


Figure 3.2: Conversion from Cartesian CS to Cylindrical CS

the two-dimensional (2D) representation of the Cylindrical coordinates of the whole surface, where ${}^{\{T\}}r$ is shown as a function of ${}^{\{T\}}\theta$ and ${}^{\{T\}}z$. Nortice that for a cylindrical objects, ${}^{\{T\}}\theta$ and ${}^{\{T\}}z$ can be evenly distributed, so that ${}^{\{T\}}r$ is in a grid manner. The 2D representation makes it easier to visualize, store and further analysis. Therefore, it is the same to obtain the coordinates in either Cartesian CS or Cylindrical CS.

### 3.1.2 Imaging Geometry

In previous section, the Cartesian CS is not specified as it can be chosen as any rectangular coordinate system in 3D space. But with visual based measurement system, it is straightforward to use the camera CS, $\{C\}$, as the main 3D CS. Figure 3.4 shows the CSs used in a regular visual based measurement system. In general two CS are involved in such a system, namely 3D camera CS, $\{C\}$, and 2D pixel CS, $\{p\}$. The setups of $\{C\}$ and $\{p\}$ follow the

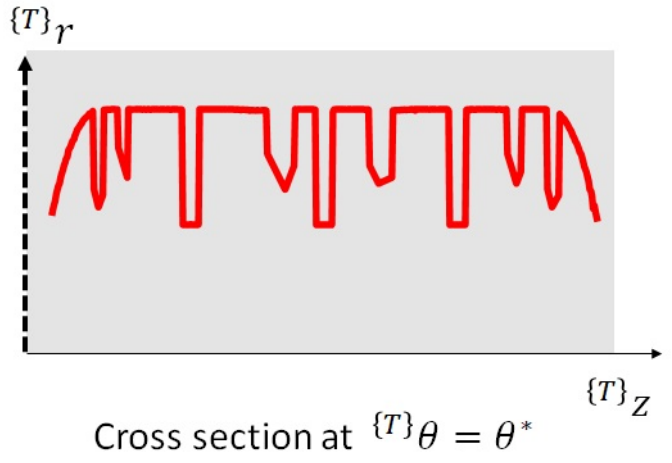


(a) One cross section in Cartesian CS

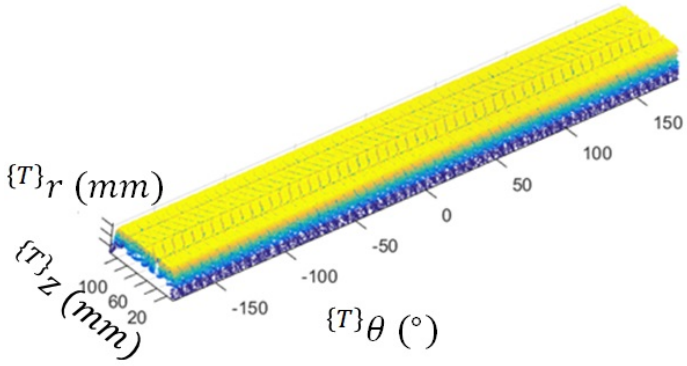


(b) 3D representation in Cylindrical CS

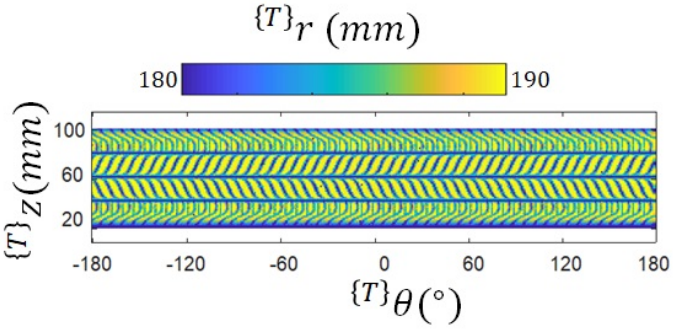


(c) 2D representation in Cylindrical CS

Figure 3.3: Representation of a cylindrical object in Cylindrical CS

convention given in [25].

According to pin-hole camera model, the ray that reflects from the $(i, j)^{th}$ patch of the target

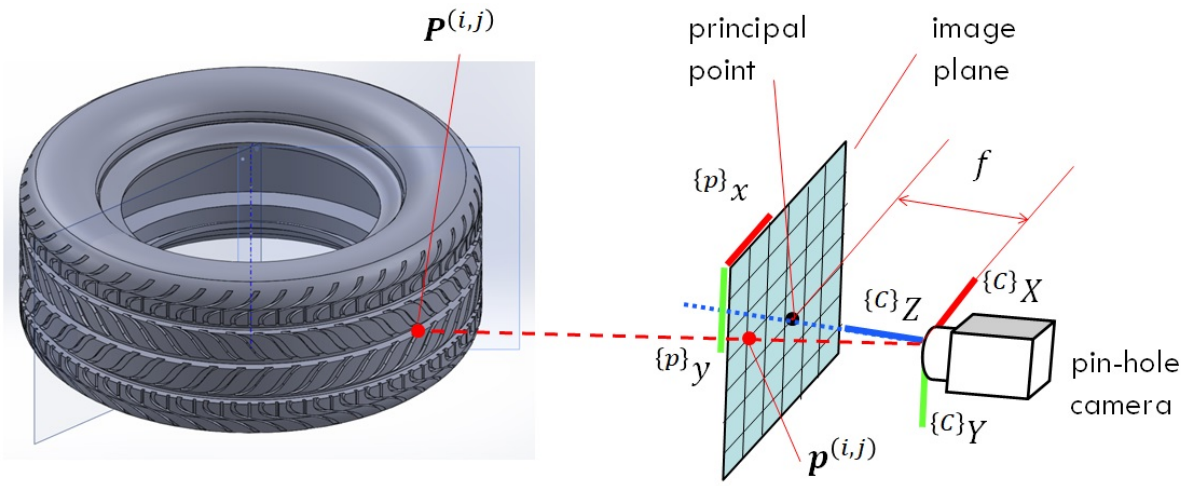


Figure 3.4: Imaging geometry

surface, whose center is at $\boldsymbol{P}^{(i,j)}$, passing through the entrance aperture, falls on the $(i,j)^{th}$ sensing cell of the camera, which is at $\boldsymbol{p}^{(i,j)}$ in the image plane. The distance from the origin of $\{C\}$ to the image plane is the focal length, $f$, and the $Z$-axis of $\{C\}$ intersects the image plane at principal point, whose coordinates are $[{}^{\{p\}}c_x, {}^{\{p\}}c_y]^\top$.

Given the coordinates of $\boldsymbol{P}^{(i,j)}$ and $\boldsymbol{p}^{(i,j)}$ at $\{C\}$ and $\{p\}$ are

$$ {}^{\{C\}}\boldsymbol{P}^{(i,j)} = \left[{}^{\{C\}}X^{(i,j)}, {}^{\{C\}}Y^{(i,j)}, {}^{\{C\}}Z^{(i,j)}\right]^\top \tag{3.2a} $$

$$ {}^{\{p\}}\boldsymbol{p}^{(i,j)} = \left[{}^{\{p\}}x^{(i,j)}, {}^{\{p\}}y^{(i,j)}\right]^\top \tag{3.2b} $$

respectively. According to perspective projection model [3]. :

$$ \frac{{}^{\{C\}}X^{(i,j)}}{{}^{\{C\}}Z^{(i,j)}} = \frac{{}^{\{p\}}x^{(i,j)} - {}^{\{p\}}c_x}{f} \tag{3.3a} $$

$$ \frac{{}^{\{C\}}Y^{(i,j)}}{{}^{\{C\}}Z^{(i,j)}} = \frac{{}^{\{p\}}y^{(i,j)} - {}^{\{p\}}c_y}{f} \tag{3.3b} $$

$f$, $c_x$, $c_y$ are camera intrinsic parameters which can be calibrated through camera intrinsic calibration [100].

As it can be seen from Equation 3.3a and 3.3b, the information of one dimension, ${}^{\{C\}}Z^{(i,j)}$, is lost during perspective projection. And one of the tasks of 3D profiling techniques is then to use images to recover the lost dimension, which is normally depth information of the given object.

## 3.2 Conventional 3D Profiling Approach

### 3.2.1 Overview

Laser Section (LS) technique is often used in conventional approaches for 3D profiling [33]. Figure 3.5(a) illustrates the concept of the LS-based approach. A laser device generates a narrow light beam, which is splitted into a sheet of light by a splitter. The sheet of light, which is referred to as laser plane in the remaining of this dissertation, intersects tire surface in a line. This line diffusely reflects the laser light to the camera, forming an image with bright pixels, which contains information cues to reveal the profile of one cross section of the tire tread.

Figure 3.5(b) shows the block diagram, with the graphic illustration of key variables shown in Figure 3.5(c). The camera takes a picture of the tire surface under laser illumination. Due to the ambient reflection from the tire surface, the image contains not only tire surface that under laser illumination, but also the one without laser illumination. A laser pixel detection step is necessary to remove the influence of unnecessary background, resulting a set of 2D pixel points $\left\{{}^{\{p\}}\boldsymbol{p}_l\right\}_{ls}$, With pre-calibrated camera and laser parameters, the result from laser pixel detection part is used to generate a set of 3D points in $\{C\}$, $\left\{{}^{\{C\}}\boldsymbol{P}_l\right\}_{ls}$, using triangulation. $\left\{{}^{\{C\}}\boldsymbol{P}_l\right\}_{ls}$ is the profile of the one cross section generated from one LS measurement through two steps, namely laser pixel detection and triangulation. The details

of the two steps are introduced in the following section.

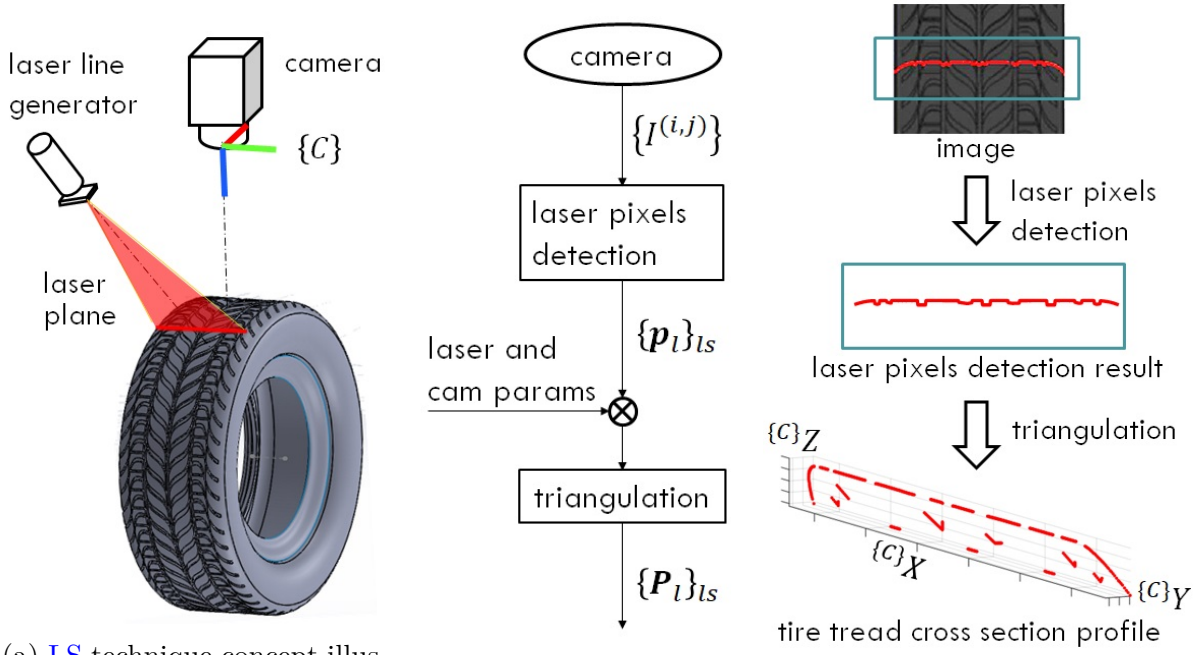


(a) LS technique concept illustration

(b) LS technique block diagram

(c) LS technique block diagram illustration

Figure 3.5: LS method schematic diagram

### 3.2.2 Laser Pixel Detection

Figure 3.6(a) shows the image of the tire under the illumination of the laser line generator. By using a red laser device, it is reasonable only to use the red channel for the purpose of laser pixel detection, which is shown in Figure 3.6(b). Notice the color in Figure 3.6(b) represents the red channel intensity of the pixels. The color scale map is shown in Figure 3.6(c) as dark red represent saturation in red channel while dark blue represent zero intensity. As digital cameras are subjected to all kinds of errors including Gaussian noise, salt and pepper noise and quantization noise, and due to the diffuse reflection of the laser light to other region of the tire other than the intersection of the laser plane and the tire, Figure 3.6(b) presents a noisy trend. It is conventional to apply a Gaussian low-pass filter and a global thresholding

to remove the noise. The filtered result is shown in Figure 3.6(d). The final detection result is shown in Figure 3.6(e). The processing from Figure 3.6(d) to Figure 3.6(e) is through a local threshoulding and is explained as below.

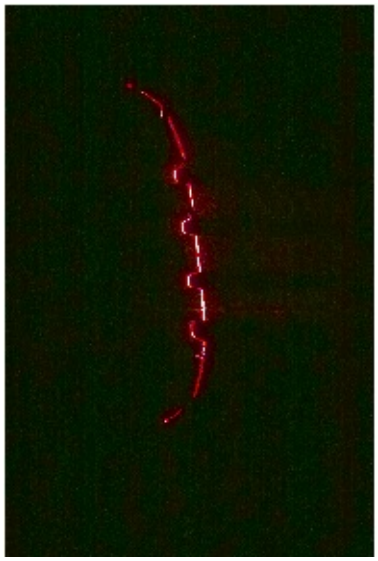

(a) LS image

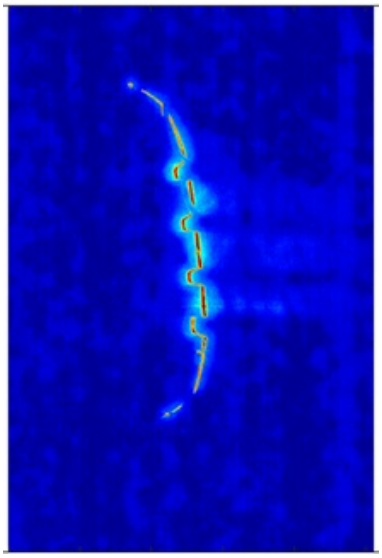

(b) Red channel of LS image

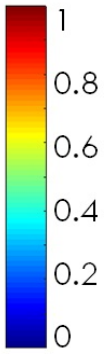


(c) Color map

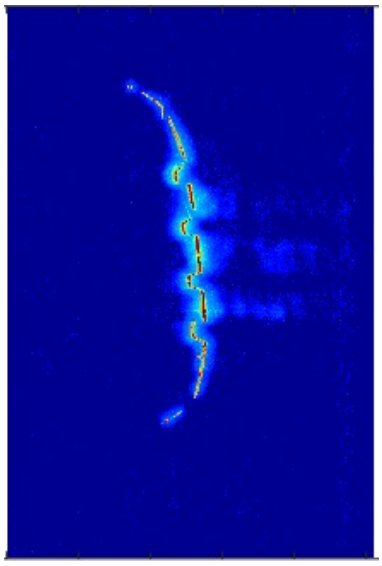

(d) Red channel after global thresholding

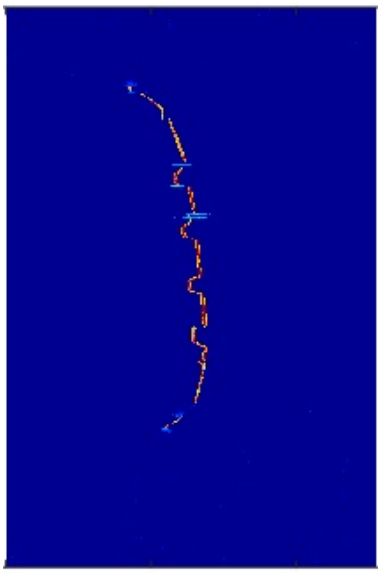

(e) Red channel after local thresholding

Figure 3.6: Laser image

As shown in Figure 3.6(d), although errors are removed from the original image, due to the

width of the laser line, its image is wider than one pixel. Figure 3.7(a) shows the schematic diagram of the reason of the width of laser line. Figure 3.7(b) displays a close look of the laser image, which shows the width of laser line. Figure 3.7(c) shows the red channel intensity of the $2000^{th}$ row. It is obvious from the figure that the width of the laser line is obout 100 pixels. As it is shown both theoretically and experimentally, yhe laser image is not a line with one pixel width as desired. The following part of this section is proposed to deal with this situation.

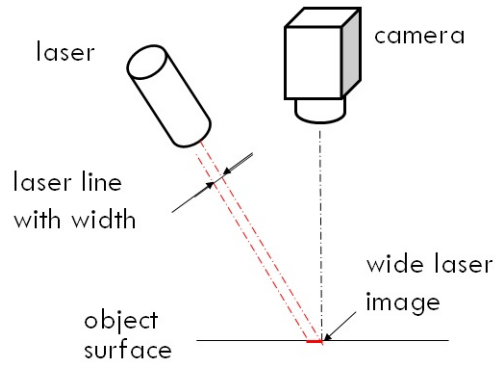


(a) Schematic explanation of laser line width

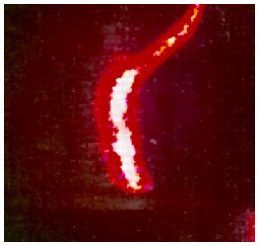

(b) Close look of laser line width

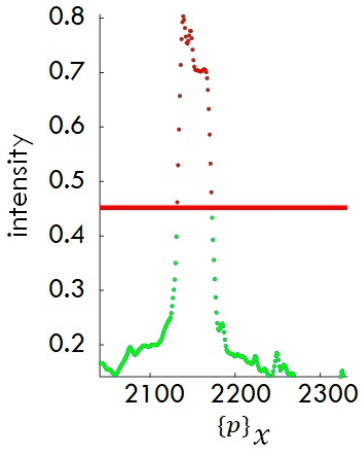


(c) Pixel intensity of the $2000^{th}$ row

Figure 3.7: Laser pixel detection

As the laser line generator is placed in a way that the laser plane is vertical (or almost vertical). Then the locus of laser pixels captured by the camera can be described with the x-coordinate, given as a function of ${}^{\{p\}}y$ coordinates ${}^{\{p\}}x = f_{laser}({}^{\{p\}}y)$. In other words, the laser image can be processed row by row. A local thresholding value, which is the red line in Figure 3.7(c), is determined by the half maximum of the concerned row to threshold the useful pixels. Then the intensity-weighted centroid method is determined as the laser pixel for concerned row as:

$$ {}^{\{p\}}x_{t,j} = \frac{\sum_{{}^{\{p\}}x_k \in {}^{\{p\}}\boldsymbol{\chi}_j} {}^{\{p\}}x_k r_k}{\sum_{{}^{\{p\}}x_k \in {}^{\{p\}}\boldsymbol{\chi}_j} r_k} \tag{3.4} $$

where ${}^{\{p\}}\boldsymbol{\chi}_j$ is the region of the $j^{th}$ row where red channel value is greater than the local threshold value and ${}^{\{p\}}x_k$ is the ${}^{\{p\}}x$ coordinate of the pixel and $r_k$ is the corresponding red channel value. Notice the ${}^{\{p\}}y$ coordinate of the $j^{th}$ row is $j$. Then a laser pixel is obtained for the $j^{th}$ row. Repeat this process for all rows, then a set of points in pixel plane $\left\{{}^{\{p\}}\boldsymbol{p}_l\right\}$ are obtained as output of the laser pixel detection step.

### 3.2.3 Triangulation

Given a set of laser pixels as $\left\{{}^{\{p\}}\boldsymbol{p}_l\right\}$, the 3D coordinates of laser pixels are obtained through triangulation method. Assume ${}^{\{p\}}\boldsymbol{p}_l = [{}^{\{p\}}x_l, {}^{\{p\}}y_l]^\top \in \left\{{}^{\{p\}}\boldsymbol{p}_l\right\}$, and its corresponding 3D point in $\{C\}$, is ${}^{\{C\}}\boldsymbol{P}_l = [{}^{\{C\}}X_l, {}^{\{C\}}Y_l, {}^{\{C\}}Z_l]^\top$. The coordinates first satisfy Equation 3.3a and 3.3b. It is noted that ${}^{\{C\}}\boldsymbol{P}_l$ is on the laser plane. In other words, the coordinates also satisfies

$$A_{lp}{}^{\{C\}}X_l + B_{lp}{}^{\{C\}}Y_l + C_{lp}{}^{\{C\}}Z_l + D_{lp} = 0 \tag{3.5}$$

where $[A_{lp}, B_{lp}, C_{lp}, D_{lp}]$ defines the laser plane which is pre-calibrated.

Then the 3 unknowns ${}^{\{C\}}X_l, {}^{\{C\}}Y_l, {}^{\{C\}}Z_l$ can be solved using the 3 linear equations as:

$${}^{\{C\}}\boldsymbol{P}_l = \begin{bmatrix} {}^{\{C\}}X_l \\ {}^{\{C\}}Y_l \\ {}^{\{C\}}Z_l \end{bmatrix} = \begin{bmatrix} A_{lp} & B_{lp} & C_{lp} \\ f & 0 & {}^{\{p\}}x_l - {}^{\{p\}}c_x \\ 0 & f & {}^{\{p\}}y_l - {}^{\{p\}}c_y \end{bmatrix}^{-1} \begin{bmatrix} -D_{lp} \\ 0 \\ 0 \end{bmatrix} \tag{3.6}$$

For each ${}^{\{p\}}\boldsymbol{p}_l \in \left\{{}^{\{p\}}\boldsymbol{p}_l\right\}$ a ${}^{\{p\}}\boldsymbol{p}_l$ can be solved. Then the point cloud of the cross section, ${}^{\{C\}}\boldsymbol{P}_l$, can be obtained.

## 3.3 Photometry-based 3D Profiling

Figure 3.8 illustrates a schematic process of 3D reconstruction using Photometric Stereo (PS), which is a photometry-based surface normal recovery technique, and Surface Normal Integration (SNI). The fixed camera observes the same object $M_{led}$ times under point illumination from $M_{led}$ point light sources at fixed and pre-calibrated positions, resulting $M_{led}$ images of the object. PS technique employs the different appearances from the $M_{led}$ images to solve for the surface normal pixel by pixel, resulting a surface normal map with pixel resolution. The shape of the object then can be integrated from the surface normal map using SNI technique. The following subsections describe the fundamentals of PS and SNI to explain how photometry-based 3D profiling approach works.

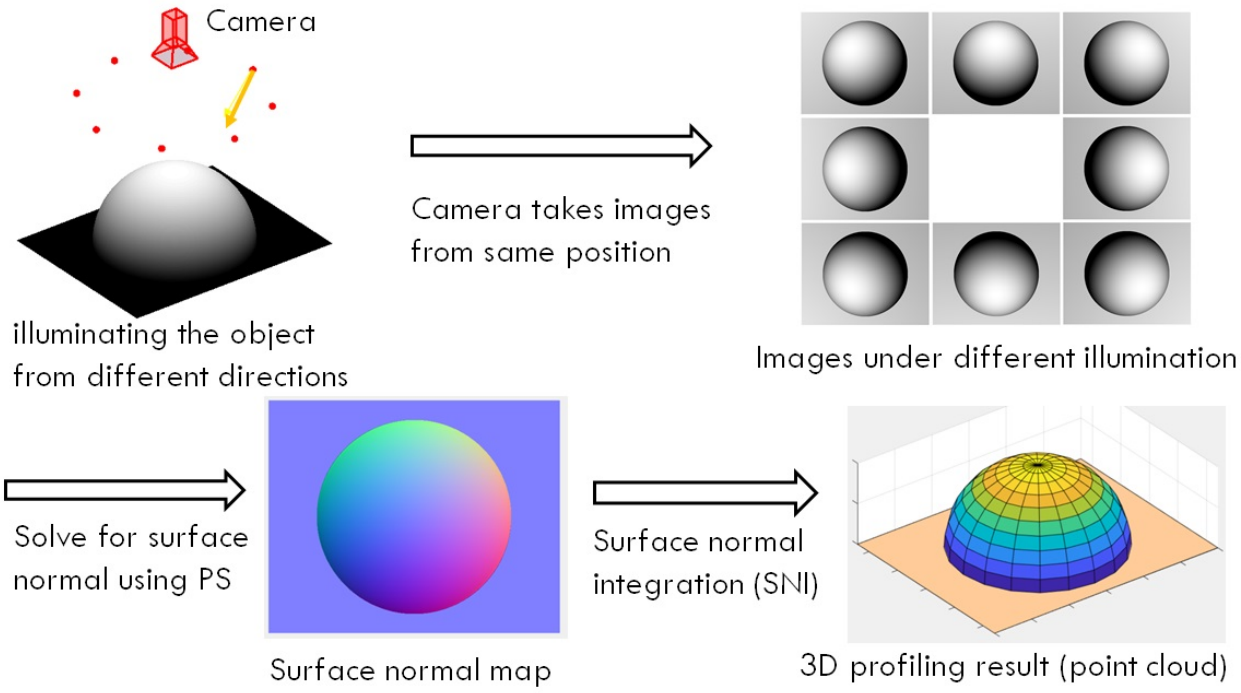


Figure 3.8: 3D reconstruction using PS and SNI

### 3.3.1 Image Formation

As PS is a reverse process of image formation, it is necessary to review how a digital image is formed to understand the motivation behind PS. Figure 3.9 shows a schematic diagram of image formation. A digital camera observes an object under illumination from a point light source. The appearance of the $(i,j)^{th}$ patch on the surface can be represented using the intensity of the $(i,j)^{th}$ pixel, $I^{(i,j)}$. The $(i,j)^{th}$ patch is assumed to be planar, with $\bar{\boldsymbol{n}}^{(i,j)}$ denoting its surface normal. The lighting direction, scene irradiance, and the viewing direction of this patch is given as $\bar{\boldsymbol{l}}^{(i,j)}$, $E^{(i,j)}$, and $\bar{\boldsymbol{v}}^{(i,j)}$.

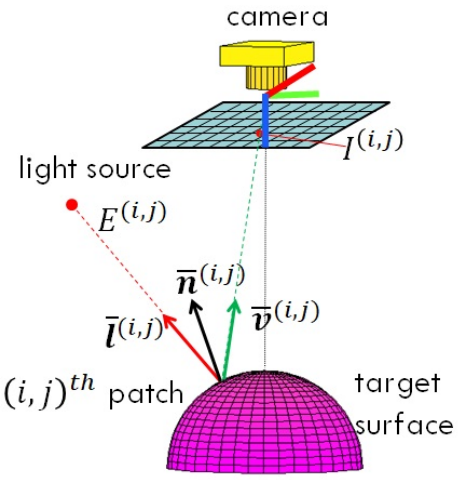


Figure 3.9: Image formation schematic diagram

Figure 3.10 shows the block diagram of the process of image formation. As the analysis is for $(i,j)^{th}$ patch, the superscript $\cdot^{(i,j)}$ is omitted in the remaining of this section, if there is no ambiguity.

The $(i,j)^{th}$ patch of surface reflects some fraction of incident light from the point illumination to the camera. The relation of the power irradiates from the lighting source to the $(i,j)^{th}$ patch, or scene irradiance $E$, and the power reflects from the patch to the camera, or scene

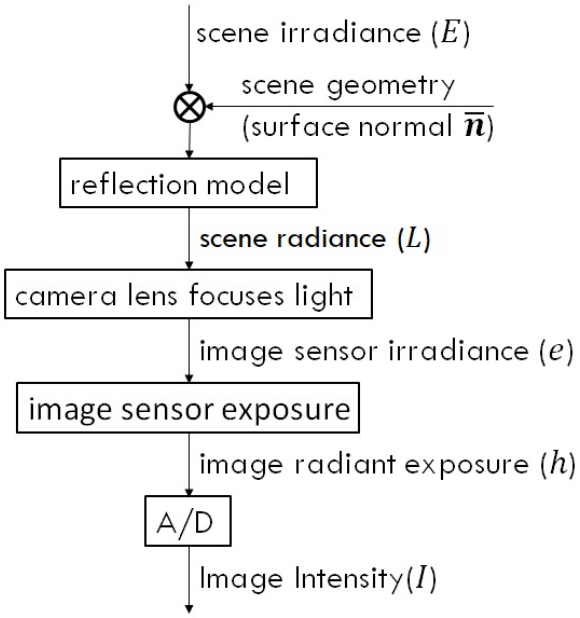


Figure 3.10: Image formation block diagram

radiance $L$, is defined by the reflection model, which is a function of $\bar{\boldsymbol{n}}$, $\bar{\boldsymbol{l}}$ and $\bar{\boldsymbol{v}}$ as:

$$L = Ef(\bar{\boldsymbol{n}}, \bar{\boldsymbol{l}}, \bar{\boldsymbol{v}}) \tag{3.7}$$

Notice that $f(\bar{\boldsymbol{n}}, \bar{\boldsymbol{l}}, \bar{\boldsymbol{v}})$ is a scene related function, which depends on the reflection properties of the material of the small patch.

The camera lens focuses the energy to the $(i, j)^{th}$ image sensor. The power received by the image sensor, or image sensor irradiance $e$, is proportional to $L_r$ as:

$$e = k_{lens}L = Ek_{lens}f(\bar{\boldsymbol{n}}, \bar{\boldsymbol{l}}, \bar{\boldsymbol{v}}) \tag{3.8}$$

where $k_{lens}$ is a lens based parameter.

The energy collected by the image sensor during the exposure, or image radiant exposure $h$,

can be calculated by integration through exposure time $t_e$ as:

$$h = \int_0^{t_e} e(\tau) d\tau \tag{3.9}$$

With the assumption that the scene is stationary during the exposure, $e(\tau)$ is time invariant. Therefore Equation 3.9 yields:

$$h = \int_0^{t_e} e(\tau) d\tau = E t_e k_{lens} f(\bar{\boldsymbol{n}}, \bar{\boldsymbol{l}}, \bar{\boldsymbol{v}}) \tag{3.10}$$

The image radiant exposure is then boosted by a sensor amplifier, usually referred to as the file speed or ISO speed, and then digitized by an A/D converter to form the image intensity $I$ as

$$I = k_{iso} h = E k_{iso} t_e k_{lens} f(\bar{\boldsymbol{n}}, \bar{\boldsymbol{l}}, \bar{\boldsymbol{v}}) \tag{3.11}$$

where $k_{iso}$ is a scaling factor defined by ISO standard.

Notice $k_{iso}$, $t_e$, $k_{lens}$ in Equation 3.11 are camera-related parameters, which are the same for all pixels once the camera is setup for a visual observation. Define $\gamma = k_{iso} t_e k_{lens}$, then Equation 3.11 can be rewritten for the $(i,j)^{th}$ pixel as:

$$I^{(i,j)} = \gamma E^{(i,j)} f^{(i,j)}(\bar{\boldsymbol{n}}^{(i,j)}, \bar{\boldsymbol{l}}^{(i,j)}, \bar{\boldsymbol{v}}^{(i,j)}) \tag{3.12}$$

where $\gamma$ is a camera related parameter which is fixed for all pixels.

### 3.3.2 Photometric Stereo in General

As indicated in Equation 3.12, the image intensity, $I^{(i,j)}$, depends on surface lighting condition $E$, incident light direction $\bar{\boldsymbol{l}}^{(i,j)}$, camera scaling factor $\gamma$, viewing direction $\bar{\boldsymbol{v}}^{(i,j)}$, surface

geometry $\bar{\boldsymbol{n}}^{(i,j)}$ and surface photometric reflection function $f^{(i,j)}(\cdot)$. It means that with fixed surface parameters, $\bar{\boldsymbol{n}}^{(i,j)}$ and $f^{(i,j)}(\cdot)$, and fixed camera parameters, $\gamma$ and $\bar{\boldsymbol{v}}^{(i,j)}$, by changing the lighting condition, $E^{(i,j)}$ and $\bar{\boldsymbol{l}}^{(i,j)}$, the appearance from the observation, $I^{(i,j)}$, changes accordingly. PS technique employs this fact, using pre-calibrated lighting conditions and camera parameters to recover the surface parameters by placing multiple point lighting sources at different positions and capturing multiple images of the fixed surface using the same fixed camera.

Assume $M_{led}$ point light sources are used, and for the $l^{th}$ point light source, Equation 3.12 is satisfied. Divide $\gamma E^{(i,j)}$ on both sides of Equation 3.12, yields:

$$\hat{I}_m^{(i,j)} = f^{(i,j)}(\bar{\boldsymbol{n}}^{(i,j)}, \bar{\boldsymbol{l}}_m^{(i,j)}, \bar{\boldsymbol{v}}^{(i,j)}) \tag{3.13}$$

where $\hat{I}_m^{(i,j)}$ is referred to as corrected intensity, which is defined as:

$$\hat{I}_m^{(i,j)} \equiv \frac{I_m^{(i,j)}}{\gamma E_m^{(i,j)}} \tag{3.14}$$

With $M_{led}$ images collected under $M_{led}$ point light sources, surface normal map $\left\{\bar{\boldsymbol{n}}^{(i,j)}\right\}$ can be calculated pixel-wise as:

$$\bar{\boldsymbol{n}}^{(i,j)} = \arg\min_{\bar{\boldsymbol{n}}^{(i,j)}} \sum_{m=1}^{M_{led}} \left( \hat{I}_{ps,m}^{(i,j)} - f^{(i,j)}(\bar{\boldsymbol{n}}^{(i,j)}, \bar{\boldsymbol{l}}_m^{(i,j)}, \bar{\boldsymbol{v}}^{(i,j)}) \right)^2 \tag{3.15}$$

### 3.3.3 Diffuse Photometric Stereo

Conventional PS approaches only deal with Lambersian surface for the ease of reflection model, which satisfies Lambersian assumption ([4]) as:

$$f_{Lamb}^{(i,j)}(\bar{\boldsymbol{n}}^{(i,j)}, \bar{\boldsymbol{l}}_m^{(i,j)}, \bar{\boldsymbol{v}}^{(i,j)}) = k_d^{(i,j)} \left( \bar{\boldsymbol{n}}^{(i,j)} \cdot \bar{\boldsymbol{l}}_m^{(i,j)} \right) \tag{3.16}$$

where $k_d^{(i,j)}$ is diffuse reflectance factor, which can be considered as the proportion of diffuse reflection of the incident light. As the diffuse components are employed for surface normal estimation, the technique is referred to as DPS in this dissertation.

The substitution of Equation 3.16 into Equation 3.15 yields

$$\bar{\boldsymbol{n}}^{(i,j)} = \arg\min_{\bar{\boldsymbol{n}}^{(i,j)}} \sum_{m=1}^{M_{led}} \left( \hat{I}_{ps,m}^{(i,j)} - k_d^{(i,j)} \left( \bar{\boldsymbol{n}}^{(i,j)} \cdot \bar{\boldsymbol{l}}_m^{(i,j)} \right) \right)^2 \tag{3.17}$$

For a 3D scene, $\bar{\boldsymbol{n}}^{(i,j)}$ and $k_d^{(i,j)}$ are determined by two and one variables, respectively. $M_{led}(\geq 3)$ measurements, each with a different light direction, are required to uniquely identify $\bar{\boldsymbol{n}}^{(i,j)}$ and $k_d^{(i,j)}$.

The mathematical solution for $\bar{\boldsymbol{n}}^{(i,j)}$ and $k^{(i,j)}$ is as follows. The superscript $\cdot^{(i,j)}$ is again omitted in the remaining of this section for the simplicity of derivation.

Let $\boldsymbol{N} = k_d \bar{\boldsymbol{n}}$ and the substitution of Equation 3.17 becomes

$$\boldsymbol{N} = \arg\min_{\bar{\boldsymbol{n}}} \sum_{m=1}^{M_{led}} \left( \hat{I}_{ps,m} - \bar{\boldsymbol{N}} \cdot \bar{\boldsymbol{l}}_m \right)^2 \tag{3.18}$$

$\boldsymbol{N}$ can be solved as:

$$\boldsymbol{N} = (\boldsymbol{\mathcal{L}}^\top \boldsymbol{\mathcal{L}})^{-1} \boldsymbol{\mathcal{L}}^\top \boldsymbol{\mathcal{I}} \tag{3.19}$$

where $\boldsymbol{\mathcal{L}} = \left[\bar{\boldsymbol{l}}_1, ..., \bar{\boldsymbol{l}}_{M_{led}}\right]^\top$ and $\boldsymbol{\mathcal{I}} = \left[\hat{I}_1, ..., \hat{I}_{M_{led}}\right]^\top$. Then albedo and surface normal can be calculated as:

$$k_d = \|\boldsymbol{N}\| = \left\| \left(\boldsymbol{\mathcal{L}}^\top \boldsymbol{\mathcal{L}}\right)^{-1} \boldsymbol{\mathcal{L}}^\top \boldsymbol{\mathcal{I}} \right\|, \tag{3.20a}$$

$$\bar{\boldsymbol{n}} = \frac{\boldsymbol{N}}{\|\boldsymbol{N}\|} = \frac{\left(\boldsymbol{\mathcal{L}}^\top \boldsymbol{\mathcal{L}}\right)^{-1} \boldsymbol{\mathcal{L}}^\top \boldsymbol{\mathcal{I}}}{\left\| \left(\boldsymbol{\mathcal{L}}^\top \boldsymbol{\mathcal{L}}\right)^{-1} \boldsymbol{\mathcal{L}}^\top \boldsymbol{\mathcal{I}} \right\|}, \tag{3.20b}$$

### 3.3.4 Surface Normal Integration

The lighting direction $\bar{\boldsymbol{l}}^{(i,j)}$ and viewing direction $\bar{\boldsymbol{v}}^{(i,j)}$ in Figure 3.9 can be obtained in $\{C\}$. Therefore the surface normal $\bar{\boldsymbol{n}}^{(i,j)}$ calculated using $\bar{\boldsymbol{l}}^{(i,j)}$ and $\bar{\boldsymbol{v}}^{(i,j)}$ is also in $\{C\}$. As in this section, all parameters are described in $\{C\}$, the front superscript ${}^{\{C\}}\cdot$ is omitted. With orthographic projection assumption, for the $(i,j)^{th}$ image sensor cell, the projection of the corresponding reflectance patch onto image plane has a uniform size. In other words, uniform distribution surface space in $X$ and $Y$ direction is assumed with grid size as $\Delta$.

Write $\bar{\boldsymbol{n}}^{(i,j)} = [n_x^{(i,j)}, n_y^{(i,j)}, n_z^{(i,j)}]^\top$, and $\boldsymbol{P}^{(i,j)} = \left[X^{(i,j)}, Y^{(i,j)}, Z^{(i,j)}\right]^\top$, then the plane equation can be written as:

$$n_x^{(i,j)}(X - X^{(i,j)}) + n_y^{(i,j)}(Y - Y^{(i,j)}) + n_z^{(i,j)}(Z - Z^{(i,j)}) = 0 \tag{3.21}$$

Figure 3.11 shows the schematic diagram for SNI. As three points are necessary to determine a plane, the $(i,j)^{th}$ planar patch is assumed to be determined by point $\boldsymbol{P}^{(i,j)}$, $\boldsymbol{P}^{(i+1,j)}$, and $\boldsymbol{P}^{(i,j+1)}$. Substitute point $\boldsymbol{P}^{(i+1,j)}$ and $\boldsymbol{P}^{(i,j+1)}$ into Equation 3.21, yield:

$$n_x^{(i,j)}(X^{(i+1,j)} - X^{(i,j)}) + n_y^{(i,j)}(Y^{(i+1,j)} - Y^{(i,j)}) + n_z^{(i,j)}(Z^{(i+1,j)} - Z^{(i,j)}) = 0 \tag{3.22a}$$

$$n_x^{(i,j)}(X^{(i,j+1)} - X^{(i,j)}) + n_Y^{(i,j)}(Y^{(i,j+1)} - Y^{(i,j)}) + n_z^{(i,j)}(Z^{(i,j+1)} - Z^{(i,j)}) = 0 \tag{3.22b}$$

Notice $X^{(i+1,j)} = X^{(i,j)}$, $Y^{(i+1,j)} = Y^{(i,j)} + \Delta$, $X^{(i,j+1)} = X^{(i,j)} + \Delta$, $Y^{(i,j+1)} = Y^{(i,j)}$, then

$$\frac{Z^{(i+1,j)} - Z^{(i,j)}}{\Delta} = -\frac{n_y^{(i,j)}}{n_z^{(i,j)}} = \hat{q}^{(i,j)} \tag{3.23a}$$

$$\frac{Z^{(i,j+1)} - Z^{(i,j)}}{\Delta} = -\frac{n_x^{(i,j)}}{n_z^{(i,j)}} = \hat{p}^{(i,j)} \tag{3.23b}$$

where $\hat{p}^{(i,j)}$ and $\hat{q}^{(i,j)}$ are calculated surface gradient along $x$ and $y$ direction.

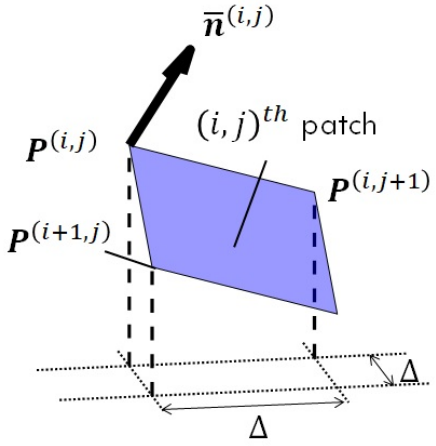


Figure 3.11: Schematic diagram for SNI

Having the surface gradient represented by the surface depth, the residual to minimize for identifying the surface depth can be formulated as

$$\epsilon = \sum_{i=1}^{R}\sum_{j=1}^{C}\left(\left(\frac{Z^{(i,j+1)} - Z^{(i,j)}}{\Delta} - \hat{p}^{(i,j)}\right)^2 + \left(\frac{Z^{(i+1,j)} - Z^{(i,j)}}{\Delta} - \hat{q}^{(i,j)}\right)^2\right) \tag{3.24}$$

where $R$ and $C$ are the numbers of rows and columns of imaging cells of the camera respectively. The SNI minimizes this cost function by taking the partial derivative of $\epsilon$ with respect to each $Z^{(i,j)}$ and forcing the partial derivative to be 0. This is equivalent to satisfying the

following linear equation:

$$\begin{aligned} & Z^{(i,j+1)} + Z^{(i+1,j)} - 4Z^{(i,j)} + Z^{(i,j-1)} + Z^{(i-1,j)} \\ = \; & \Delta\left(-\hat{p}^{(i,j)} - \hat{q}^{(i,j)} + \hat{p}^{(i,j-1)} + \hat{q}^{(i-1,j)}\right) \end{aligned} \tag{3.25}$$

For linear equations, there are $R \times C$ unknowns. Then the $R \times C$ equations can be represented in the format of matrix:

$$\boldsymbol{M}\boldsymbol{Z} = \boldsymbol{V} \tag{3.26}$$

where $\boldsymbol{M} \in \mathcal{R}^{RC \times RC}$ is a sparse positive definite matrix, $\boldsymbol{V} \in \mathcal{R}^{RC \times 1}$ is a vector calculated by the linear combination of $p^{(i,j)}$ and $q^{(i,j)}$ and $\boldsymbol{Z} = \left[Z^{(1,1)}, Z^{(1,2)}, ..., Z^{(1,C)}, Z^{(2,1)}, ..., Z^{(R,C)}\right]^\top \in \mathcal{R}^{RC \times 1}$ is the vector of surface depth to derive.

The $X$ and $Y$ coordinates can be calculated using the uniform distribution assumption as:

$$X^{(i,j)} = X_{min} + j\Delta \tag{3.27a}$$

$$Y^{(i,j)} = Y_{min} + i\Delta \tag{3.27b}$$

where $X_{min}$ and $Y_{min}$ are the $X$ and $Y$ coordinates of left upper corner point. The processes of the PS and SNI result in a point cloud

$$\{\boldsymbol{P}_{ps}\} = \left\{\boldsymbol{P}^{(i,j)} = [X^{(i,j)}, Y^{(i,j)}, Z^{(i,j)}]^\top | \forall (i,j) \in \{(1,1), ..., (R,C)\}\right\} \tag{3.28}$$

with pixel resolution.

While the PS enables 3D reconstruction in high resolution, the fundamental issue is the depth accuracy. Since the surface depth is determined by integrating the surface gradients,

the depth measurement could be subject to significant errors if the gradients are not identified accurately.

## 3.4 Chapter Summary

This chapter has presented the concept of circumferential profiling and general visual-based 3D reconstruction techniques. The LS technique, which is adopted in the conventional approach, was introduced with details, whilst PS-based technique was explained from forward problem, image formation, first to derive the general solution for surface normal, which can be further processed to obtain surface profile via SNI. The two techniques are essential for the further development of the proposed approach for the specular micro-texture photometry-based 3D profiling.

# Chapter 4

# Micro-texture Circumferential 3D Profiling with Photometry-based Surface Normal Recovery

In this chapter, the mathematical description and solution of the micro-texture circumferential 3D profiling photometry-based surface normal recovery are presented. The proposed approach first utilizes the conventional circumferential 3D profiling to create a global constraint and a photometry-based technique to obtain the surface normal map. With circumferential pre-processing step, multiple PS measurements are converted into circumferential representation. The circumferential measurement from the conventional approach provides a global bounding effect when using the circumferential surface normal to recover the circumferential profile, yielding a high resolution circumferential shape measurement of the target object, with micro-texture geometric features.

## 4.1 Proposed Solution

Like all other techniques that use first integration from first or even higher order derivative, the result of SNI suffers from accumulative error, due to aliasing error, quantization error, system error and so on. This kind of error is referred to as 'dead reckoning' in the field of

navigation, and results in a large difference between the ground truth value to the integrated value. Inspired from the field of navigation, which occasionally uses global reference on the map to correct the calculated position from dead reckoning, the surface normal from PS technique is used together with the LS measurements as global constraint. As a consequence, the result is more accurate.

Figure 4.1 shows the schematic diagram of the proposed approach for circumferential 3D profiling with micro-texture photometry. To start with, the object is observed by $K_{ps}$ PS measurements from different angular position. The $M_{led}$ images taken for the ${k_{ps}}^{th}$ PS measurement are referred to as $\{\{I_{ps,1:M_{led}}\}\}^{k_{ps}}$, with the angular position as $\theta_{k_{ps}}$. The corresponding surface normal measurement is $\left\{\{C_{k_{ps}}\}\bar{\boldsymbol{n}}\right\}^{k_{ps}}$ as the measurement is with respect to the $\{C_{k_{ps}}\}$ CS. The circumferential surface normal measurement step first converts the measurement into a uniform CS for all the $K_{ps}$ measurement, with the angular positions measured by the encoder and the rotation axis which is represented by a unit vector $\bar{\boldsymbol{v}}$ passing a point $\boldsymbol{C}$ in $\{C_0\}$. The circumferential surface normal is then obtained by combining all the $K_{ps}$ PS measurements with respect to $\{C_0\}$ as $\left\{^{\{C_0\}}\bar{\boldsymbol{n}}\right\}^{all}$.

The same object is observed by $K_{ls}$ LS measurements. Similarly as the previous step. The $K_{ls}$ LS measurements eventually result as a point cloud in $\{C_0\}$ CS as $\left\{^{\{C_0\}}\boldsymbol{P}_{ls}\right\}^{all}$. This point cloud is sparse in nature, which serves as a supporting component in the final step, which is named as 3D profiling from surface normal with global constraint. This step works similarly as SNI, but with $\left\{^{\{C_0\}}\boldsymbol{P}_{ls}\right\}^{all}$ as a global constraint to reduce accumulative error. The final result is referred to as $\left\{^{\{C_0\}}\boldsymbol{P}\right\}^{final}$.

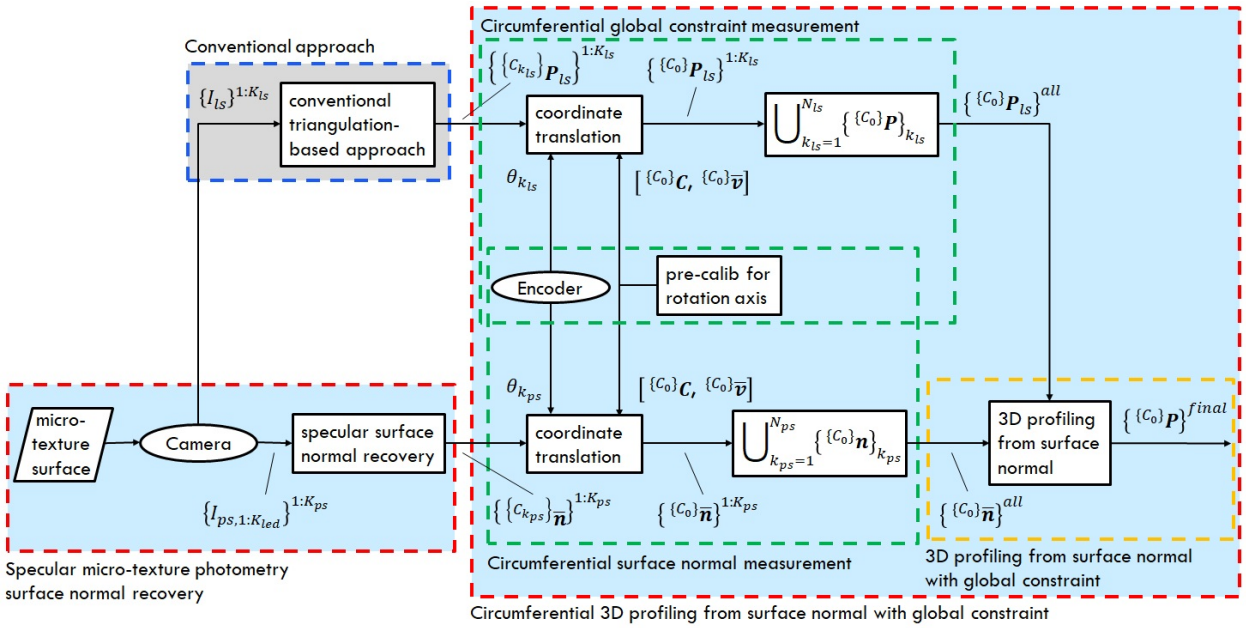


Figure 4.1: Circumferential 3D profiling with micro-texture photometry

## 4.2 Circumferential Measurement

Neither LS technique nor PS technique is able to measure the the whole object circumferentially at one time. LS technique is able to measure a cross section of the object at one scan while PS technique a small region. It is necessary to rotate the object in front of the camera, so that the whole object can be scanned. The rotation is achieved through a step motor, while the rotation angle is measured through an encoder. The individual measurement along with the angular position of the measurement will be combined together to generate the circumferential measurement.

In reality, what is actually moving is the object while the camera is fixed. However, for the ease of the derivation, the proposed approach reinterprets this as a fixed object with a moving camera, rotating along the same axis but towards opposite direction. $\{C_{k_{ls}}\}(\cdot)$ is used to indicate a quantity with respect to the CS of the camera pose for ${k_{ls}}^{th}$ LS measurement.

$\{C_{k_{ps}}\}(\cdot)$ is similarly used to indicate a quantity with respect to the CS of the $k_{ps}{}^{th}$ PS measurement. It is to be noted that $\{C_0\} = \{C_{k_{ls}=1}\} = \{C_{k_{ps}=1}\}$, which is the initial camera CS for both LS and PS measurements.

As the same camera, object and rotation axis are used for both LS measurements and PS measurements, the rotation axis can be pre-calibrated and represented in the camera CS as a unit vector, ${}^{\{C_0\}}\bar{\boldsymbol{v}}$, passing a fixed point ${}^{\{C_0\}}\boldsymbol{C}$.

### 4.2.1 Circumferential Global Constraint Measurement

Starting from the LS measurement, at angular position $\theta^{k_{ls}}$, the laser line generator projects the laser plane which intersects with the object surface. The camera captures a LS image of the object with such LS illumination. Using the technique described in Section 3.2, a point cloud can be obtained as $\left\{\{C_{k_{ls}}\}\boldsymbol{P}_{ls}\right\}^{k_{ls}}$. For a circumferential measurement, $K_{ls}$ LS measurement is required. The problem of LS circumferential measurement can then be described as:

Given:

1. ${}^{\{C_0\}}\bar{\boldsymbol{v}}$ and ${}^{\{C_0\}}\boldsymbol{C}$, which can be used to describe the rotation axis,

2. $K_{ls}$ LS angular positions, $\left\{\theta^{k_{ls}} \middle| \forall k_{ls} \in \{1, ..., K_{ls}\}\right\}$, at which LS measurements are taken,

3. $K_{ls}$ point clouds, $\left\{\left\{\{C_{k_{ls}}\}\boldsymbol{P}_{ls}\right\}^{k_{ls}} \middle| \forall k_{ls} \in \{1, ..., K_{ls}\}\right\}$, from LS measurement at all LS angular positions, with respect to the $ls^{th}$ LS .

Solve for:

1. A point cloud, $\left\{{}^{\{C_0\}}\boldsymbol{P}_{ls}\right\}^{all}$, which is the combination of all the $K_{ls}$ LS measurements, with respect to the initial camera CS.

This problem can be solved in two steps: to begin with, convert all the $K_{ls}$ point clouds from their own measuring CS to a uniform CS. As each image of the LS technique is taken with a different camera pose, it is necessary to describe them with respect to the uniform CS. In the proposed approach, the initial camera CS, $\{C_0\}$, where the first LS and PS measurements are taken, is used as the uniform CS.

The conversion from coordinate in $\{C_{k_{ls}}\}$ to $\{C_0\}$ is given as below. Given $\boldsymbol{P} \in \left\{{}^{\{C_{k_{ls}}\}}\boldsymbol{P}_{ls}\right\}^{k_{ls}}$, which is a point from the measurement CS and $\boldsymbol{P'} \in \left\{{}^{\{C_0\}}\boldsymbol{P}_{ls}\right\}^{k_{ls}}$, which is a point from the uniform CS. Write $\theta^{k_{ls}}$ as $\theta$, ${}^{\{C_0\}}\bar{\boldsymbol{v}}$ as $\bar{\boldsymbol{v}}$, and ${}^{\{C_0\}}\boldsymbol{C}$ as $\boldsymbol{C}$, for simplicity, then according to coordinate transformation, $\boldsymbol{P}$ and $\boldsymbol{P'}$ satisfies:

$$\boldsymbol{P'} = \boldsymbol{C} + (\boldsymbol{P} - \boldsymbol{C})^{\top}\bar{\boldsymbol{v}}(1 - \cos\theta)\bar{\boldsymbol{v}} + (\boldsymbol{P} - \boldsymbol{C})\cos\theta + \bar{\boldsymbol{v}} \times (\boldsymbol{P} - \boldsymbol{C})\sin\theta \tag{4.1}$$

This results in $K_{ls}$ sets of point cloud in $\{C_0\}$, which can be used in the second step of the proposed solution: merging all the $K_{ls}$ sets of point cloud into one set of point cloud in $\{C_0\}$ as:

$$\left\{{}^{\{C_0\}}\boldsymbol{P}_{ls}\right\}^{all} = \bigcup_{k_{ls}=1}^{K_{ls}} \left\{{}^{\{C_0\}}\boldsymbol{P}_{ls}\right\}^{k_{ls}} \tag{4.2}$$

Figure 4.2 shows the result of circumferential LS measurement. A point cloud which combines all $K_{ls}$ measurements is obtained after the two steps described above. Figure 4.3 shows the result of circumferential LS measurements in cylindrical CS. It is obvious from the results that the result is a sparse point cloud.

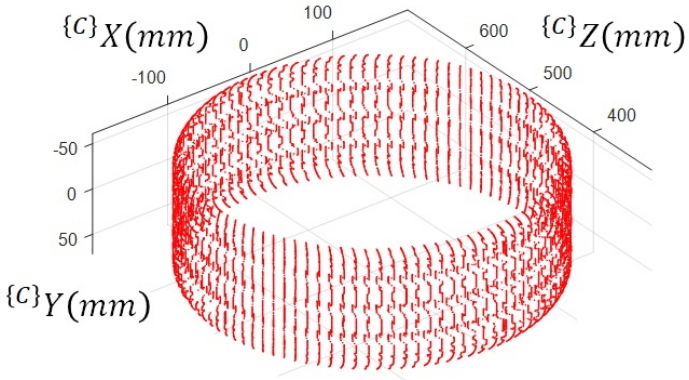


Figure 4.2: Circumferential LS measurement

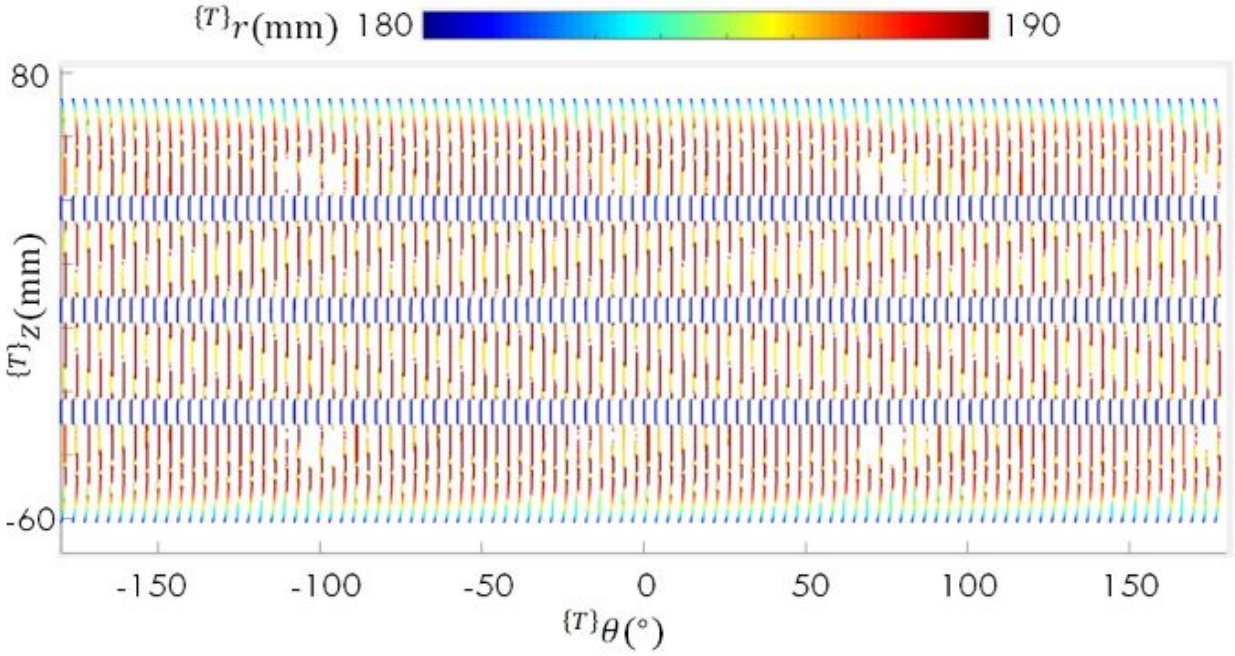


Figure 4.3: Circumferential LS measurement in Cylindrical CS

### 4.2.2 Circumferential Surface Normal Measurement

The next step is to obtain the circumferential surface normal measurements. At angular position $\theta^{k_{ps}}$, the lighting system and the camera measure the surface normal map, $\left\{ {}^{\{C_{k_{ps}}\}}\bar{\boldsymbol{n}} \right\}^{k_{ps}}$, of the object within the Field of View (FoV) of the camera using the a photometry-based surface normal recovery technique. For a circumferential measurement, $K_{ps}$ PS measurement is required. Similar to LS circumferential measurement, all $K_{ps}$ measurement need to be converted to the uniform frame $\{C_0\}$. The problem of PS circumferential measurement can then be described as:

Given:

1. ${}^{\{C_0\}}\bar{\boldsymbol{v}}$ and ${}^{\{C_0\}}\boldsymbol{C}$, which can be used to describe the rotation axis,
2. $K_{ps}$ PS angular positions, $\left\{ \theta^{k_{ps}} \middle| \forall k_{ps} \in \{1, ..., K_{ps}\} \right\}$, at which PS measurements are taken,
3. $K_{ps}$ sets of surface normal, $\left\{ \left\{ {}^{\{C_{k_{ps}}\}}\bar{\boldsymbol{n}} \right\}^{k_{ps}} \middle| \forall k_{ps} \in \{1, ..., K_{ps}\} \right\}$, from PS measurement at all PS angular positions .

Solve for:

1. A surface normal map, $\left\{ {}^{\{C_0\}}\bar{\boldsymbol{n}} \right\}^{all}$, which is the combination of all the $K_{ps}$ PS measurements.

The surface normal map from the $k_{ps}{}^{th}$ PS measurement, $\left\{ {}^{\{C_{k_{ps}}\}}\bar{\boldsymbol{n}} \right\}^{k_{ps}}$, needs to be converted to $\{C_0\}$ first. Denote $\bar{\boldsymbol{n}} = {}^{\{C_{k_{ps}}\}}\bar{\boldsymbol{n}}^{(i,j)} \in \left\{ {}^{\{C_{k_{ps}}\}}\bar{\boldsymbol{n}} \right\}$ as the surface normal of the point at $\boldsymbol{P} = {}^{\{C_{k_{ps}}\}}\boldsymbol{P}_{ps}^{(i,j)}$, where ${}^{\{C_{k_{ps}}\}}\boldsymbol{P}_{ps}^{(i,j)} = \left[ {}^{\{C_{k_{ps}}\}}X_{ps}^{(i,j)}, {}^{\{C_{k_{ps}}\}}Y_{ps}^{(i,j)}, {}^{\{C_{k_{ps}}\}}Z_{ps}^{(i,j)} \right]^\top$ can be calculated using Equation 3.3a and 3.3b. The corresponding coordinates of ${}^{\{C_0\}}\boldsymbol{P}_{ps}^{(i,j)}$ in $\{C_0\}$ are

calculated using Equation 4.1, whose surface normal in $\{C_0\}$, $\boldsymbol{n'} \in \left\{^{\{C_0\}}\boldsymbol{n}\right\}^{all}$ can be derived as:

$$\boldsymbol{n'} = \boldsymbol{n}^\top \bar{\boldsymbol{v}}(1 - \cos\theta)\bar{\boldsymbol{v}} + \boldsymbol{n}\cos\theta + \bar{\boldsymbol{v}} \times \boldsymbol{n}\sin\theta \tag{4.3}$$

Figure 4.4 shows the result of circumferential PS measurement. A surface normal map attached to a cylindrical object is shown in the figure. Notice that the surface normal is presented using RGB color through the following formula:

$$[r, g, b]^\top = \frac{1 - \bar{\boldsymbol{n}}}{2} \tag{4.4}$$

Figure 4.5 shows the surface normal map in cylindrical CS. This figure shows the strength of representing properties of cylindrical objects in Cylindrical CS.

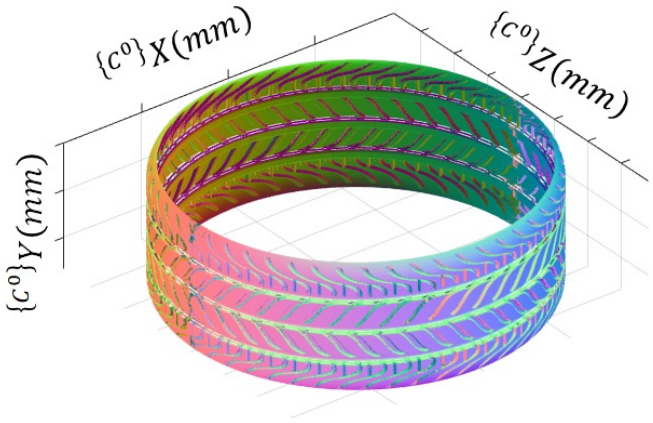


Figure 4.4: Circumferential surface normal map

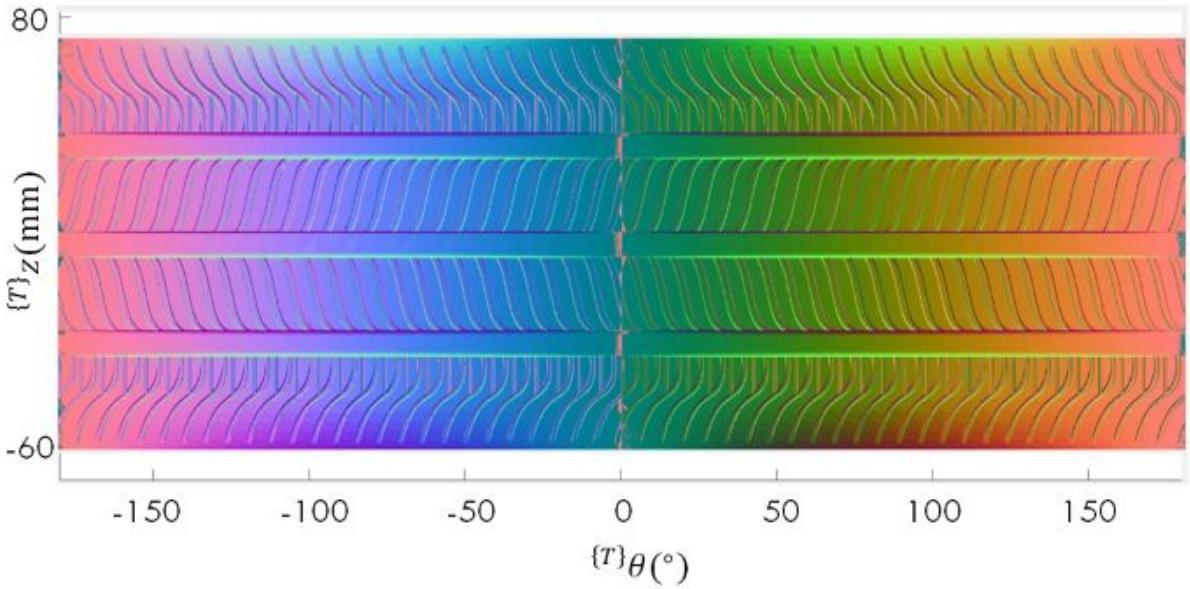


Figure 4.5: Circumferential surface normal map in Cylindrical CS

## 4.3 3D Profiling from Surface Normal Map with Global Constraint

The problem of using surface normal map only for surface profiling is the same as integration from first order derivative, which is referred to as 'dead reckoning' using inertial measurement data. The result always suffers from accumulative error, and could differ significantly from the ground truth. The approach to reduce accumulative error is to use sparse direct measurement as global correction. In this section, the proposed approach is illuminated with one field of view.

Figure 4.6(a) explains the geometric setup for one FoV scan, as the camera can only observe a small portion of the cylindrical object. The measured surface normal map from the photometry-based surface normal recovery technique only covers a small region, which is shown in Figure 4.6(c). Using the technique described in Section 4.2.1, a circumferential LS measurement could be obtained. Trim the result that outside the FoV out, a sparse

point cloud inside the FoV is obtained. Figure 4.6(b) shows the trimmed sparse point cloud measurement in side the FoV. It is noted that the dark blue color indicates no measurement at that pixel position.

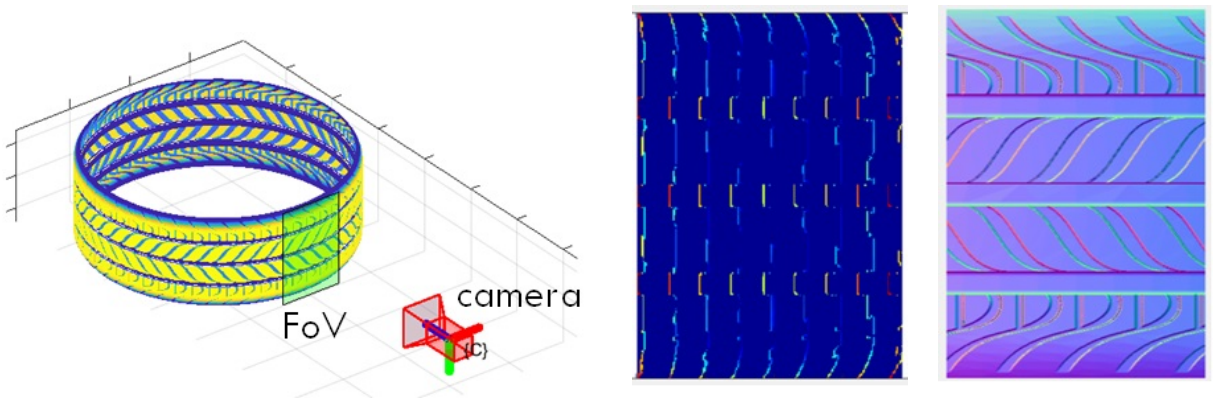


(a) Field of view of one measurement

(b) LS measurement of one FoV

(c) Surface normal map of one FoV

Figure 4.6: Input of hybrid approach

The solution of the proposed 3D profiling from surface normal map with global constraint is shown below. Similar as the description of SNI in Section 3.3.4, denote $\hat{p}^{(i,j)} = \frac{\hat{n}_x^{(i,j)}}{\hat{n}_z^{(i,j)}}$ and $\hat{q}^{(i,j)} = \frac{\hat{n}_y^{(i,j)}}{\hat{n}_z^{(i,j)}}$, where $[\hat{n}_x^{(i,j)}, \hat{n}_y^{(i,j)}, \hat{n}_z^{(i,j)}]^\top = \bar{\boldsymbol{n}}^{(i,j)} \in \left\{{}^{\{C_0\}}\boldsymbol{n}\right\}_{ps,all}$, which is the corresponding surface normal of $\boldsymbol{P}^{(i,j)} \in \left\{{}^{\{C_0\}}\boldsymbol{P}\right\}^{final}$, then the geometric cost of the $(i,j)^{th}$ point of the target surface is defined as:

$$e_{geo}^{(i,j)} = \left( \left( \frac{Z^{(i,j+1)} - Z^{(i,j)}}{\Delta} - \hat{p}^{(i,j)} \right)^2 + \left( \frac{Z^{(i+1,j)} - Z^{(i,j)}}{\Delta} - \hat{q}^{(i,j)} \right)^2 \right) \tag{4.5}$$

where $Z^{(i,j)}$ is the $Z$ coordinate of the $(i,j)^{th}$ point in $\{C_0\}$, and $\Delta$ is the spacial resolution. Assume that the point $\hat{\boldsymbol{P}} \in \left\{{}^{\{C_0\}}\boldsymbol{P}_{ls}\right\}^{all}$ measures the same point at the object surface with the $Z$ coordinate as $\hat{Z}^{(i,j)}$, then the positional cost of the $(i,j)^{th}$ point of the target surface is defined as:

$$e_{pos}^{(i,j)} = \left( Z^{(i,j)} - \hat{Z}^{(i,j)} \right)^2 \tag{4.6}$$

Notice that LS technique only produces sparse measurement, which means that there might not be a point in $\left\{{}^{\{C_0\}}\boldsymbol{P}_{ls}\right\}^{all}$ that measures the concerned point. $\omega_{pos}^{(i,j)}$ is then adopted to describe the existence of measurement of $\boldsymbol{P}^{(i,j)}$ in $\left\{{}^{\{C_0\}}\boldsymbol{P}_{ls}\right\}^{all}$:

$$\omega_{pos}^{(i,j)} = \begin{cases} 1, & \text{if } \exists \hat{\boldsymbol{P}}^{(i,j)} \in \left\{{}^{\{C_0\}}\boldsymbol{P}_{ls}\right\}^{all} \text{ measures } \boldsymbol{P}^{(i,j)} \in \left\{{}^{\{C_0\}}\boldsymbol{P}\right\}^{final} \\ 0, & \text{otherwise} \end{cases} \tag{4.7}$$

Then the cost function for the proposed approach is then defined as:

$$\epsilon = \sum_{i=1}^{R}\sum_{j=1}^{C}\left(e_{geo}^{(i,j)} + \lambda\omega_{pos}^{(i,j)}e_{pos}^{(i,j)}\right) \tag{4.8}$$

where $\lambda$ is a weighting factor, which can be used to adjust the relative effect between the LS measurement and PS measurement.

Similarly as the way of minimizing cost function Equation 3.24, taking partial derivative of $\epsilon$ with respect to each $Z^{(i,j)}$ is taken for the cost function Equation 4.8 and forcing it to be 0, it gives the following linear equation:

$$\begin{aligned} & Z^{(i,j+1)} + Z^{(i+1,j)} - \left(4 + \omega_{pos}^{(i,j)}\Delta^2\lambda\right) Z^{(i,j)} + Z^{(i,j-1)} + Z^{(i-1,j)} \\ = \quad & \Delta\hat{p}^{(i,j)} + \Delta\hat{q}^{(i,j)} - \omega_{pos}^{(i,j)}\Delta^2\lambda\hat{Z}^{(i,j)} - \Delta\hat{p}^{(i,j-1)} - \Delta\hat{q}^{(i-1,j)} \end{aligned} \tag{4.9}$$

Similar to the case in 3.3.4, by combining all the $R \times C$ equations, a set of equations in the format of matrix can be obtained:

$$\boldsymbol{M}\boldsymbol{Z} = \boldsymbol{V} \tag{4.10}$$

Different from the $\boldsymbol{M}$ matrix in Equation 3.26, the $((i-1)*C+j)^{th}$ diagonal element of $\boldsymbol{M}$ matrix in Equation 4.10 can be $-4$ if there is no LS measurement, or $-\left(4+\Delta^2\lambda\right)$ if the

LS measurement exists. Similarly, the value of the $((i-1)*C+j)^{th}$ element at the $RC \times 1$ vector $\boldsymbol{V}$ in Equation 4.10 also differs from the one in Equation 3.26 based on the existence of LS measurement.

As can be seen from previous explanation, Equation 4.10, or the set of Equation 4.9, combines the measurement from both technique, making the measuring result more robust. Notice $\lambda$ can be used to change the relative effect between the LS measurement and PS measurement. Increasing $\lambda$ makes the measurement from LS technique dominating the final result. By contrast, the PS technique will have a strong influence on the 3D profiling result when choosing a small $\lambda$.

Figure 4.7 shows the output of the proposed approach.

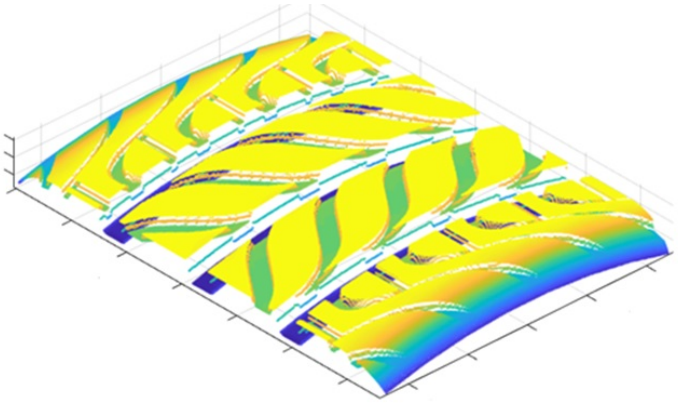

Figure 4.7: Output of hybrid approach

## 4.4 Conclusions and Future Works

This chapter has presented the methodology to use the proposed specular photometry-based surface normal recovery technique and the result from conventional circumferential approach for the purpose of circumferential micro-texture 3D profiling. A sparse circumferential point cloud was generated from the conventional approach to provide a global constraint for further

usage by surface normal integration. A 3D micro-texture 3D profile was generated due to the global-bounding effect from the conventional approach and the pixel-level surface normal measurement from the proposed SPS technique.

This chapter mainly focused on the derivative of circumferential in Cartesian CS. The variation in Cylindrical CS may ease the calculation and improve the accuracy, which remains open for exploration.

# Chapter 5

# Specular Micro-texture Photometry for Surface Normal Recovery

In this chapter, a micro-texture photometry inspired technique, Specular Photometric Stereo (SPS), is proposed to recover surface normal pixel-wisely. The proposed technique utilizes the specular components of the same micro-texture patch under different lighting conditions to mathematically determine the surface normal of the pixel-corresponding patch. The proposed technique is supposed to deal with dark surfaces, where conventional PS techniques fail due to the violation of Lambertian assumption of such surfaces. The recovered surface normal is then used to iteratively refine other photometric parameters in order to improve the performance of the proposed technique.

## 5.1 Problem Overview

Figure 5.1(a) and (b) shows the difference between a Lambertian ball and a ball with dark material under point illumination. As it can be seen from the figure, the intensity of the image of the Lambertian ball drops smoothly from the brightest region to the dark region, while for the rubber ball, a specular highlight region can be easily noticed and the off-specular region is almost dark. The intensity drop shows an exponentially trend. Figure 5.1(c) shows the tire surface image under point illumination. It is obvious that the surface of

dark object highly violates Lambertian assumption, making the application of DPS on such surfaces inappropriately.

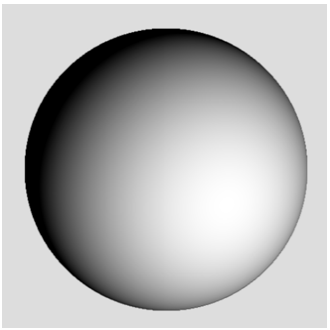

(a) Lambertian ball under point illumination

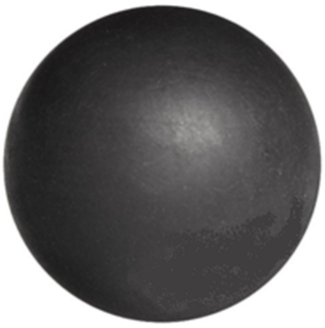

(b) Rubber ball under point illumination

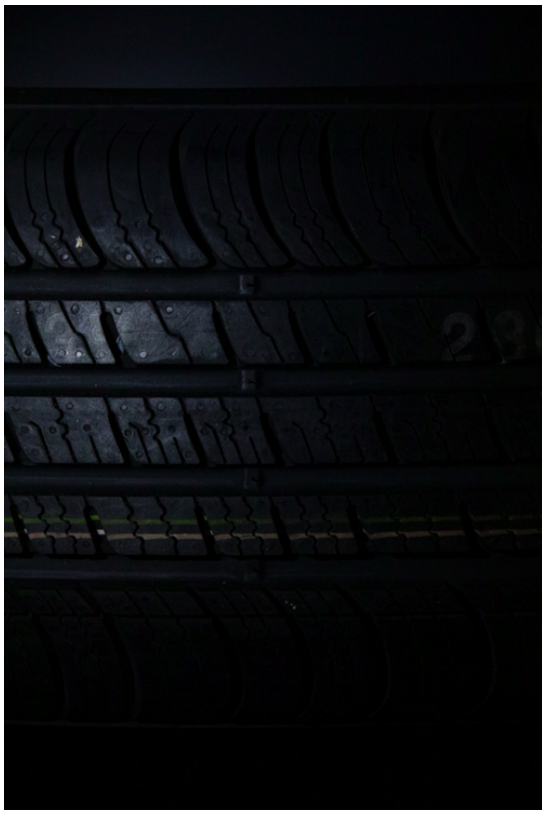

(c) Tire surface under point illumination

Figure 5.1: Violation of Lambertian assumption on dark objects

As the Lambertian assumption is violated, DPS cannot be applied for dark surface surface normal recovery. The reason why DPS is utilized widely due to its simplicity on mathematical derivation and linearity, which leads to robust result. On the other hand, Non-linear Iterative Photometric Stereo (NIPS), which is described in the literature review, assumes a complex, highly non-linear reflection model and solves for surface normal through non-linear iteration method. Though the reflection model suits the dark objects, the non-linear iteration method is notorious for its un-robustness.

In this chapter, a robust solution is proposed for the specific application of photometry-based

technique, which is inspired from DPS, but with more complicated reflection model, trying to minimize the non-linearity of the reflection model.

## 5.2 Specular Micro-texture Photometry

As shown in Equation 3.13, the corrected pixel intensity depends on the reflection model $f^{(i,j)}(\bar{\boldsymbol{n}}^{(i,j)}, \bar{\boldsymbol{l}}^{(i,j)}, \bar{\boldsymbol{v}}^{(i,j)})$. In Section 3.3.2, the solution to general PS problem is given, whereas in Section 3.3.3, diffuse reflection model is assumed to derive the solution for the calculation of surface normal. The real world material is, however, rarely Lambertian. A more general reflection model is desired to solve for the real world situation, to deal with the violation of Lambertian assumption. Blinn-Phong reflection model [6] is used in this dissertation for its efficiency on its usage in computer vision applications. Blinn Phong reflection model formulates the reflection intensity as a combination of diffuse reflection and specular reflection when there is no ambient light as below:

$$f_{BP}^{(i,j)}(\bar{\boldsymbol{n}}^{(i,j)}, \bar{\boldsymbol{l}}_m^{(i,j)}, \bar{\boldsymbol{v}}^{(i,j)}) = k_d^{(i,j)} \left(\bar{\boldsymbol{n}}^{(i,j)} \cdot \bar{\boldsymbol{l}}_m^{(i,j)}\right) + k_s^{(i,j)} \left(\bar{\boldsymbol{n}}^{(i,j)} \cdot \bar{\boldsymbol{h}}_m^{(i,j)}\right)^{\alpha^{(i,j)}} \tag{5.1}$$

where $k_s^{(i,j)}$ is the specular reflectance factor, which can be considered as the proportion of specular reflection from the incident light. $\alpha^{(i,j)}$ is shininess constant, which is larger for surfaces that are smoother and of more mirror-like reflection. $\bar{\boldsymbol{h}}_m^{(i,j)}$ is the halfway vector calculated as:

$$\bar{\boldsymbol{h}}_m^{(i,j)} = \frac{\bar{\boldsymbol{l}}_m^{(i,j)} + \bar{\boldsymbol{v}}^{(i,j)}}{\left\| \bar{\boldsymbol{l}}_m^{(i,j)} + \bar{\boldsymbol{v}}^{(i,j)} \right\|} \tag{5.2}$$

$\bar{\boldsymbol{h}}$ bisects the angle between $\bar{\boldsymbol{l}}$ and $\bar{\boldsymbol{v}}$ as shown in Figure 5.2 As shown in Equation 5.1, the first part of the reflection, the diffuse component, is formulated as same as the one in Lambertian model (Equation 3.16), whereas the second part of reflection, the specular

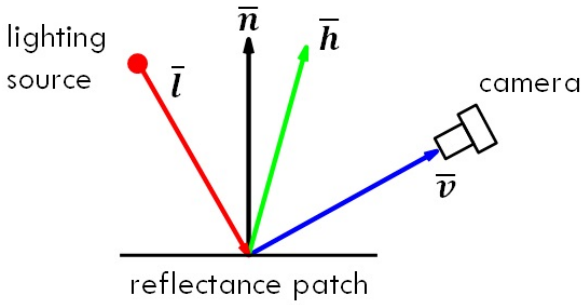


Figure 5.2: Halfway vector

component, drops exponentially when $\bar{\boldsymbol{h}}$ being more away from $\bar{\boldsymbol{n}}$, which indicates a less critical reflection, as normally, $\alpha^{(i,j)} \gg 1$.

The substitution of Equation 5.1 into Equation 3.13 yields

$$\hat{I}_m^{(i,j)} = f_{BP}^{(i,j)}(\bar{\boldsymbol{n}}^{(i,j)}, \bar{\boldsymbol{l}}_m^{(i,j)}, \bar{\boldsymbol{v}}^{(i,j)}) = k_d^{(i,j)} \left(\bar{\boldsymbol{n}}^{(i,j)} \cdot \bar{\boldsymbol{l}}_m^{(i,j)}\right) + k_s^{(i,j)} \left(\bar{\boldsymbol{n}}^{(i,j)} \cdot \bar{\boldsymbol{h}}_m^{(i,j)}\right)^{\alpha^{(i,j)}} \tag{5.3}$$

Table 5.1 shows the the reflection parameters of some typical materials [7]. From the comparison of the black rubber with the other two material, the diffuse reflectance factor is much smaller than the specular reflectance factor,

$$k_s \gg k_d \approx 0. \tag{5.4}$$

In other words, for a dark surface, the brightness of bright pixels mainly comes from specular reflectance rather than the diffuse reflection:

$$\hat{I}_{s,k}^{(i,j)} \gg \hat{I}_{d,k}^{(i,j)} \approx 0. \tag{5.5}$$

where $\hat{I}_{d,k}^{(i,j)}$ and $\hat{I}_{s,k}^{(i,j)}$ is defined as the corrected diffuse component and the corrected specular

component respectively as:

$$\hat{I}_{d,m}^{(i,j)} = k_d^{(i,j)} \left( \bar{\boldsymbol{n}}^{(i,j)} \cdot \bar{\boldsymbol{l}}_m^{(i,j)} \right) \tag{5.6a}$$

$$\hat{I}_{s,m}^{(i,j)} = k_s^{(i,j)} \left( \bar{\boldsymbol{n}}^{(i,j)} \cdot \bar{\boldsymbol{h}}_m^{(i,j)} \right)^{\alpha^{(i,j)}} \tag{5.6b}$$

The overall intensity of pixel with little specular reflectance tends to be small.

| material | black rubber | chrome | white plastic |
|---|---|---|---|
| $k_d$ | 0.05 | 0.25 | 0.55 |
| $k_s$ | 0.4 | 0.4 | 0.7 |
| $\alpha$ | 40 | 300 | 100 |

Table 5.1: Typical material reflection parameters

Assume that the corrected diffuse component and the corrected specular component can be separated from the overall intensity, Equation 5.6a can be utilized in a similar way as conventional DPS approaches to calculate the surface normal. As a matter of fact, most outlier rejection approach assume $\hat{I}_{s,k}^{(i,j)} \approx 0$ for the inliers [93]. However, applying such approach is error prone for dark surfaces as the diffuse component is small and therefore has a relatively large signal error ratio. The proposed SPS technique, on the contrary, assumes $\hat{I}_{d,k}^{(i,j)} \approx 0$ and utilizes Equation 5.6b to calculate the surface normal. Due to the small shininess constant of dark objects, the larger specular highlight makes the usable pixels a larger amount compared to other typical material.

## 5.3 Specular Micro-texture Photometry for Surface Normal Recovery

### 5.3.1 Variation of Parameters

Inspired by DPS, Equation 5.6b can also be reversed to calculate surface normal. Assume $k_d^{i,j} = 0$, then the corrected intensity only contains specular components as:

$$\hat{I}_m^{(i,j)} = \hat{I}_{s,m}^{(i,j)} = k_s^{(i,j)} \left( \bar{\boldsymbol{n}}^{(i,j)} \cdot \bar{\boldsymbol{h}}_m^{(i,j)} \right)^{\alpha^{(i,j)}} \tag{5.7}$$

However, the equation itself, along with the unit vector constrain,

$$\|\bar{\boldsymbol{n}}\| = 1, \tag{5.8}$$

contains a high level of non-linearity when solving for $\bar{\boldsymbol{n}}$. As a consequence, this equation cannot be solved through the same way as DPS, which utilizes Least Square Regression (LSR). To contour this problem, a variation of parameters is proceeded, and the problem becomes a non-linear problem but with only one non-linear parameter. The procedure is derived as:

Define

$$\boldsymbol{N}_s = k_s^{1/\alpha} \bar{\boldsymbol{n}}. \tag{5.9}$$

Notice that

$$k_s = \|\boldsymbol{N}_s\|^{\alpha}, \tag{5.10a}$$

$$\bar{\boldsymbol{n}} = \tfrac{\boldsymbol{N}_s}{\|\boldsymbol{N}_s\|}. \tag{5.10b}$$

Substitution to Equation 5.7 yields:

$$\hat{I}_m = \left(\boldsymbol{N}_s \cdot \bar{\boldsymbol{h}}_m\right)^{\alpha}. \tag{5.11}$$

Raise both sides to the power of $1/\alpha$, and then move the left hand side of the equation to the right, gives

$$\left(\hat{I}_m\right)^{1/\alpha} - \boldsymbol{N}_s \cdot \bar{\boldsymbol{h}}_m = 0. \tag{5.12}$$

It is noted that, the previous high non-linear equations have been modified to a 4-unknown ($\alpha$ and 3 in $\boldsymbol{N}_s$) equations with only one non-linear variable ($\alpha$), which can be solved using the technique described in next section.

### 5.3.2 Numerical Solution for the Non-linear Equation with Only One Non-linear Unknown

The convergence, overall problem property and a mathematical pipeline to solve of non-linear system with only one non-linear unknown is discussed by Shen and Ypma ([71]). The general problem can be described as:

Assume $N+1$ non-linear equations of $N+1$ unknowns, $[y, \boldsymbol{z}]^{\top}$, where $y \in R$ and $\boldsymbol{z} \in R^N$, of the form

$$\boldsymbol{A}(y)\boldsymbol{z} + \boldsymbol{b}(y) = \boldsymbol{0}, \tag{5.13}$$

where $\boldsymbol{A}(y)$ is an $(N+1) \times N$ matrix, which contains a scalar unknown $y$, and $\boldsymbol{b}(y)$ is an $(N+1) \times 1$ vector which is also a functions of $y$. The solution to this general problem is summarized in Algorithm 1.

The approach applies to solve the specific problem in this paper is inspired by Algorithm

**Algorithm 1**

1: Select a value for $y$.
2: Solve for the remaining $N$ unknowns $\boldsymbol{z}$ using LSR.
3: Determine whether the selected $y^*$ and corresponding computed $\boldsymbol{z}^*$ satisfy the equations, by compare the cost $\|\boldsymbol{A}(y^*)\boldsymbol{z}^* + \boldsymbol{b}(y^*)^2\|$ and the tolerance $\epsilon$.
4: If $\|\boldsymbol{A}(y^*)\boldsymbol{z}^* + \boldsymbol{b}(y^*)^2\| < \epsilon$, return $y^*$ and $\boldsymbol{z}^*$, otherwise pick a new $y$ based on previous solutions, go back to step 1.

1. The difference is instead of calculating the unknowns iteratively, multiple values are selected for the non-linear unknown first to calculate the remaining linear unknowns. The corresponding cost is also calculated. Then the set of unknowns which gives the minimum cost is picked. The modification is efficient due to the widely usage of graphics processing units (GPU). With applying parallel computing, the proposed approach is much faster and more accurate than the iterative one.

To be more specific in the content of the concerning case, the algorithm is described in Algorithm 2.

### 5.3.3 Redesign Cost Function

Due to the existence of various sources of error, such as image noise and quantization error, the number of measurement is chosen to be much larger than the number of unknowns to improve the performance. In other words, the system of equations is over-constrained. As a result, some data may disagree with the reflection model to some extent. In Equation 5.15, the term, $\left(\left(\hat{I}_m\right)^{1/\alpha_n} - \bar{\boldsymbol{h}}_m \cdot \boldsymbol{N}_{s,n}\right)^2$, can be seen as the penalty of the disagreement between the $m^{th}$ data and the reflection model. It is noticed that Equation 5.15 assumes an identical influence for each term, which means each input data have the same power on the fitted model. However, some data should have more voting power than others, such as the

**Algorithm 2**

1: Select $N_\alpha$ different values of $\alpha$, as $\alpha_n \in [1, 1024]$ for $n = 1, ..., N_\alpha$.

2: Calculate $\boldsymbol{N}_{s,n}$ as

$$\boldsymbol{N}_{s,n} = \left(\boldsymbol{H}^\top \boldsymbol{H}\right)^{-1} \boldsymbol{H}^\top \boldsymbol{\mathcal{I}}_n, \tag{5.14}$$

where $\boldsymbol{H} = \left[\bar{\boldsymbol{h}}_1, ..., \bar{\boldsymbol{h}}_{M_{led}}\right]^\top$, $\boldsymbol{\mathcal{I}}_n = \left[\left(\hat{I}_1\right)^{1/\alpha_n}, ..., \left(\hat{I}_{M_{led}}\right)^{1/\alpha_n}\right]^\top$.

3: Calculate cost $\epsilon_n$ as

$$\epsilon_n = \sum_{m=1}^{M_{led}} \left(\left(\hat{I}_m\right)^{1/\alpha_n} - \bar{\boldsymbol{h}}_m \cdot \boldsymbol{N}_{s,n}\right)^2. \tag{5.15}$$

4: Find the $(n^*)^{th}$ set, which gives the minimum cost:

$$n^* = \underset{n \in [1,...,N_\alpha]}{\arg\min}\ \epsilon_n \tag{5.16}$$

5: Return

$$\alpha = \alpha_{n^*}, \tag{5.17a}$$

$$k_s = \|\boldsymbol{N}_{s,n^*}\|^{\alpha_{n^*}}, \tag{5.17b}$$

$$\bar{\boldsymbol{n}} = \frac{\boldsymbol{N}_{s,n^*}}{\|\boldsymbol{N}_{s,n^*}\|}. \tag{5.17c}$$

one with stronger specular components. Rewriting the cost function in a weighted manner:

$$\epsilon = \sum_{m=1}^{M_{led}} w_m \left( \left( \hat{I}_m \right)^{1/\alpha} - \bar{\boldsymbol{h}}_m \cdot \boldsymbol{N}_s \right)^2, \tag{5.18}$$

Notice that Equation 5.15 is a specifica case of Equation 5.18 with the weights selected as: $w_m = 1$, for $m = 1, ..., M_{led}$.

As mentioned by Kay and Caelli ([38]), the weights have a strong influence on the fitted parameters. If incorrect weights were applied, the result would be away from the ground truth. For the case with equal weight, the parameters that minimize cost function 5.15 is the solution to

$$\left( \hat{I}_m \right)^{1/\alpha} = k_s^{1/\alpha} \left( \bar{\boldsymbol{h}}_m \cdot \bar{\boldsymbol{n}} \right), \tag{5.19}$$

for $m = 1, ..., M_{led}$, rather than the original specular reflectance model (Equation 5.7), whose solution should be the parameters which minimize the following cost function:

$$\epsilon = \sum_{m=1}^{M_{led}} \left( \hat{I}_m - k_s \left( \bar{\boldsymbol{h}}_m \cdot \boldsymbol{n} \right)^{\alpha} \right)^2. \tag{5.20}$$

As discussed above, the parameters which directly minimize cost function 5.20 cannot be derived due to the high level of non-linearity. And the difference between cost function 5.15 and cost function 5.20 comes from the application of the dark surface.

As for dark surface, the majority of the $\left\{ \hat{I} \right\}_{1:M_{led}}$ are small, because of the narrowness of specular highlight. For small $\hat{I}_m$, the penalty calculated by $\left( \left( \hat{I}_m \right)^{1/\alpha} - \bar{\boldsymbol{h}}_m \cdot \boldsymbol{N}_s \right)^2$ is enlarged compared to the penalty calculated by $\left( \hat{I}_m - k_s \left( \bar{\boldsymbol{h}}_m \cdot \boldsymbol{n} \right)^{\alpha} \right)^2$, due to the power of relatively large $\alpha$. As a conclusion, result using $w_m = 1, m = 1, ..., M_{led}$ is not a good approximation of result of cost function 5.20. Alternatively, $w_m = \left( \hat{I}_m \right)^2, m = 1, ..., M_{led}$ is

proposed, then the cost function becomes:

$$\epsilon = \sum_{m=1}^{M_{led}} \left(\hat{I}_m\right)^2 \left(\left(\hat{I}_m\right)^{1/\alpha} - \bar{\boldsymbol{h}}_m \cdot \boldsymbol{N}\right)^2 = \sum_{m=1}^{M_{led}} \left(\left(\hat{I}_m\right)^{1+1/\alpha} - \hat{I}_m \bar{\boldsymbol{h}}_m \cdot \boldsymbol{N}\right)^2. \tag{5.21}$$

It is noticed that $\left(\hat{I}_m\right)^{1+1/\alpha} \approx \hat{I}_m$ for large $\alpha$. In cost function 5.21, penalty for each˘input data is weighted by its own value, which indicates that small˘$\hat{I}_m$) does not result in large penalty. It is similar to the case if cost function 5.20 is used, and also agree with the fact that SPS relies more on pixels with strong specular components.

Then previous algorithm is upgraded to Algorithm 3.

**Algorithm 3**

1: Select $N_\alpha$ different values of $\alpha$, as $\alpha_n \in [1, 1024]$ for $n = 1, ..., N_\alpha$.

2: Calculate $\boldsymbol{N}_{s,n}$ as

$$\boldsymbol{N}_{s,n} = \left(\boldsymbol{H}^\top \boldsymbol{H}\right)^{-1} \boldsymbol{H}^\top \boldsymbol{\mathcal{I}}_{\boldsymbol{n}}, \tag{5.22}$$

where $\boldsymbol{H} = \left[\hat{I}_1 \bar{\boldsymbol{h}}_1, ..., \hat{I}_{M_{led}} \bar{\boldsymbol{h}}_{M_{led}}\right]^\top$, $\boldsymbol{\mathcal{I}}_{\boldsymbol{n}} = \left[\left(\hat{I}_1\right)^{1+1/\alpha_i}, ..., \left(\hat{I}_{M_{led}}\right)^{1+1/\alpha_n}\right]^\top$.

3: Calculate cost $\epsilon_n$ as

$$\epsilon_n = \sum_{m=1}^{M_{led}} \left(\left(\hat{I}_m\right)^{1+1/\alpha_n} - \hat{I}_m \bar{\boldsymbol{h}}_m \cdot \boldsymbol{N}_{s,n}\right)^2. \tag{5.23}$$

4: Find the $(n^*)^{th}$ set, which gives the minimum cost:

$$n^* = \underset{n \in [1,...,N_\alpha]}{\arg\min}\ \epsilon_n. \tag{5.24}$$

5: Return

$$\alpha = \alpha_{n^*}, \tag{5.25a}$$

$$k_s = \left\|\boldsymbol{N}_{s,n^*}\right\|^{\alpha_{n^*}}, \tag{5.25b}$$

$$\bar{\boldsymbol{n}} = \frac{\boldsymbol{N}_{s,n^*}}{\left\|\boldsymbol{N}_{s,n^*}\right\|}. \tag{5.25c}$$

### 5.3.4 Parameter Refinement

Although for dark surfaces, $k_s \gg k_d$, $\hat{I}_s$ drops faster than $\hat{I}_d$ due to the higher power in its formulation when the reflection angle goes away from the critical reflection angle. Consequently, for fixed lighting direction and viewing direction, there are surface whose normal causes $\hat{I}_s \approx \hat{I}_d$ or even $\hat{I}_s < \hat{I}_d$. For these cases, it is then incorrect to assume that the corrected image intensity from measurement approximately equal to $\hat{I}_s$. Therefore it is reasonable to remove the diffuse part $\hat{I}_d$ from the original measurement $\hat{I}$. The algorithm to refine the parameter by removing $\hat{I}_d$ is shown in Algorithm 4.

**Algorithm 4**

1: Assume $\hat{I}_{d,m} = 0$, then $\hat{I}_{s,m} = \hat{I}_m$.
2: Use Algorithm 3 to calculate surface normal $\bar{\boldsymbol{n}}$ and specular reflectance parameters $k_s$ and $\alpha$ from $I_{s,m}$, $m = 1, ..., M_{led}$.
3: Find the lighting direction which will give the smallest specular components among all the $M_{led}$ lights:

$$m^* = \underset{m=1,...,M_{led}}{\arg\min} \left(\bar{\boldsymbol{n}} \cdot \bar{\boldsymbol{h}}_m\right). \tag{5.26}$$

4: Calculate the diffuse reflectance factor using the $(m^*)^{th}$ illumination as:

$$k_d = \frac{\hat{I}_{m^*} - k_s \left(\bar{\boldsymbol{n}} \cdot \bar{\boldsymbol{h}}_{m^*}\right)^{\alpha}}{\bar{\boldsymbol{n}} \cdot \bar{\boldsymbol{l}}_{m^*}}. \tag{5.27}$$

5: Update $I_{s,m}$ by subtract the diffuse part from the corrected image as:

$$\hat{I}_{s,m} = \hat{I}_m - k_d \left(\bar{\boldsymbol{n}} \cdot \bar{\boldsymbol{l}}_m\right), \tag{5.28}$$

for all $m = 1, ..., M_{led}$.
6: Repeat step 2-5 till $\bar{\boldsymbol{n}}$ converge.
7: Return $\bar{\boldsymbol{n}}, k_d, k_s, \alpha$.

The parameter refinement part is important, especially for a relatively small $k_s/k_d$ case. Since the specular reflectance model is used only to recover the surface normal, the deposition of the diffuse component will make the input data fit the reflection model better compared to the raw data.

The reason why the diffuse component is taken out from the corrected intensity and use specular photometric stereo, instead of taking out specular one and using diffuse ps is specular information provide more powerful image cue to recover the surface normal, especially for the case where specular highlight is obvious. And more error tolerant due to the high power.

## 5.4 Validation

### 5.4.1 Simulated Scene

Figure 5.3 shows a simulation setup to validate the proposed SPS technique. The simulated scene contains a semi-sphere, whose reflectance parameters can be adjusted to do the parameter study. The semi-sphere shape is selected as such shape contains all the possible surface normal directions. The semi-sphere is observed from a digital camera, far enough from the scene. The generated resolution of the output images is 100 pixel by 100 pixel, with the diameter of the semisphere being 80 pixels. The scene is under sixteen well-distributed point illuminations, with only one is lit at each time.

Figure 5.4 shows the synthesized image under the $9^{th}$ illumination with $\alpha \approx 40$ and $k_d/k_s \approx 0.1$. It is noticed that the synthesized images are generated using an open source computer graphic software, POV-Ray [60], to avoid overfitting. It is worth mentioning that as POV-Ray uses a physics-based reflection model rather than Blinn-Phong reflection model. Consequently, the reflection parameters, $\alpha$, $k_d$ and $k_s$, are not assigned directly, but approximate the desired value through adjusting the actual reflection parameters used by the software. Table 5.2 summarizes the experimental parameters. The ratio between diffuse reflection factor and specular reflection factor is used to study the performance of the pro-

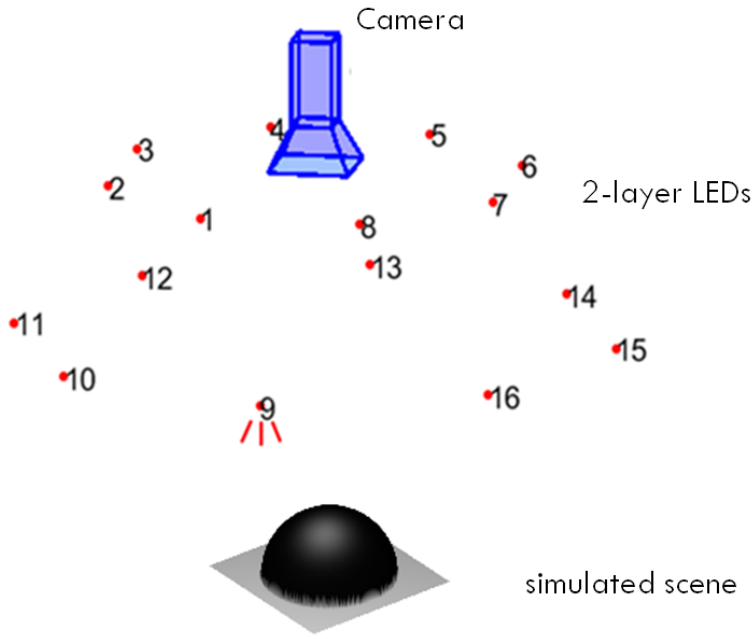


Figure 5.3: Simulated scene

posed SPS technique, as the absolute values of the two parameters can be adjusted through the camera scaling factor.

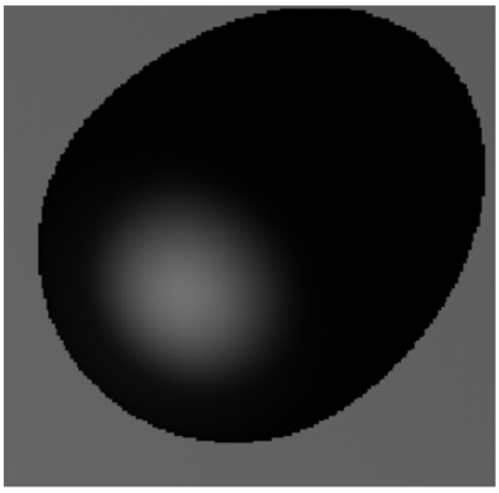

Figure 5.4: Synthesized image with $\alpha = 40$ and $k_d/k_s = 0.1$

Two other techniques, DPS and NIPS, are implemented together with the proposed SPS technique on the synthesized data to evaluate the performance of the proposed SPS tech-

| object | semi-sphere |
|---|---|
| simulation software | POV-Ray |
| image resolution | 100pixel × 100pixel |
| # of point illumination | 16 |
| $\alpha$ | 40 |
| $k_d/k_s$ | $[10^{-2}, 10^{-1.8}, ..., 10^{2}]$ |

Table 5.2: Simulated scene parameters

nique. Normally, the performance are evaluated in two-ways, angular error and rerendering error.

Angular error can be calculated through the comparison between the ground truth surface normal and calculated surface normal. As the synthesized data is used, the ground truth is availability for comparison. To be more specific, the angular error map at pixel $(i, j)$ can be calculated as

$$e_{\theta}^{(i,j)} = \arccos\left(\bar{\boldsymbol{n}}_{gt}^{(i,j)} \cdot \bar{\boldsymbol{n}}_{cal}^{(i,j)}\right), \tag{5.29}$$

where $\bar{\boldsymbol{n}}_{gt}^{(i,j)}$ is the surface normal from ground truth, and $\bar{\boldsymbol{n}}_{cal}^{(i,j)}$ is the surface normal from calculation.

Rerendering error, on other hand, can be used for the case when ground truth is absent. It applies the fitted reflectance model and image formation procedure to rerender the image of the scene, and then compares the rerendered image with the captured image. The formulation to calculate the rerender error at pixel $(i, j)$ can be calculated as

$$e_{\hat{I}}^{(i,j)} = \sum_{m=1}^{M_{led}} \left( \frac{\left| \hat{I}_{m,gt}^{(i,j)} - f(\bar{\boldsymbol{l}}_{m}^{(i,j)}, \bar{\boldsymbol{v}}^{(i,j)}, \bar{\boldsymbol{n}}_{cal}^{(i,j)}, \boldsymbol{p}_{cal}^{(i,j)}) \right|}{\hat{I}_{m,gt}^{(i,j)}} \right), \tag{5.30}$$

where $\hat{I}_{m,gt}^{(i,j)}$ is the corrected intensity of pixel $(i, j)$ under $m^{th}$ illumination, $f(\bar{\boldsymbol{l}}_{m}^{(i,j)}, \bar{\boldsymbol{v}}^{(i,j)}, \bar{\boldsymbol{n}}_{cal}^{(i,j)}, \boldsymbol{p}_{cal}^{(i,j)})$

is the fitted forward reflectance and image formation model and $\boldsymbol{p}_{cal}^{(i,j)}$ is the fitting parameters for the forward model.

Figure 5.5 shows the experimental results for the case of $\alpha = 40$ and $k_d/k_s = 0.1$. The angular errors and rerendering errors are shown in the second and third row respectively, with the second, third and fourth column showing the results for SPS, DPS, NIPS technique respectively. The last column shows the color scale for the angular errors and rerendering errors. As it is shown in Figure 5.5, for the case of $\alpha = 40$ and $k_d/k_s = 0.1$, the angular error is way much smaller than the two other techniques, while some larger error around the boundary due to the lack of specular reflection from that region. Though the rerendering error of the propose SPS is also smaller, this criteria is in general not suitable for evaluation for dark surfaces as the term $\hat{I}_{m,gt}^{(i,j)}$ might be very small for some pixels. Consequently, the following analysis bases on the angular error only.

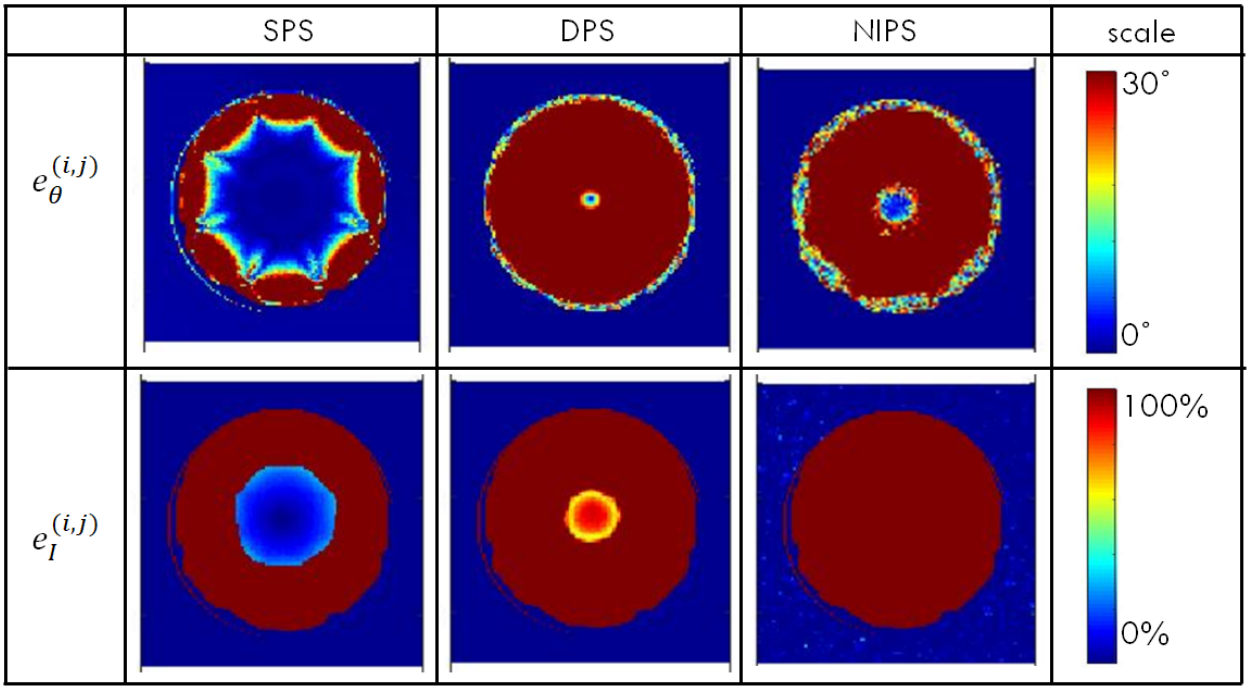


Figure 5.5: Error analysis with $\alpha = 40$ and $k_d/k_s = 0.1$

Figure 5.6 shows the angular error v.s. the ratio of $k_d$ and $k_s$ to evaluate the effectiveness

of the proposed SPS technique. The red line represents the performance of SPS while the yellow and blue ones the performance of DPS and NIPS. As it can be seen from the Figure, SPS performs much better than the other two techniques when the specular components are dominating, while when $k_d \approx 0.3k_s$, the other two performs better as the violation on Lambertian assumption loosens. As the reflection property of the tire surface falls in the range where SPS outperforms the conventional approach, the effectiveness of the proposed SPS technique is confirmed in simulated environment.

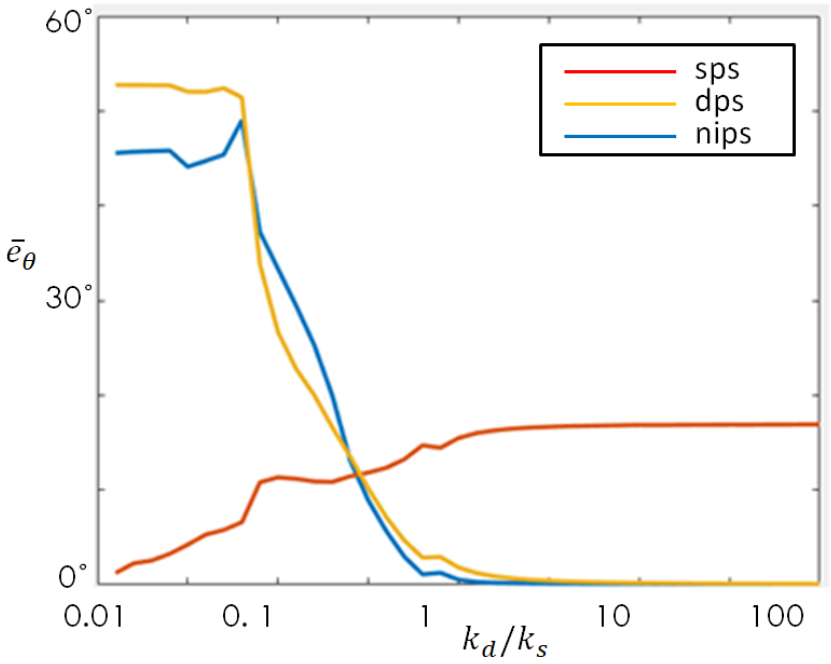


Figure 5.6: Parameter study using simulated scene

### 5.4.2 Real World Objects

The next step of the evaluation of the proposed technique is to apply it on real world objects. Figure 5.7 shows the system to collect data in the real world to verify SPS. The system contains a digital camera for data collection and sixteen LEDs for point illumination. The scanning objects need to be placed in front of the camera and the lighting system. The whole

system need to be placed in totally dark environment to illuminate the influence of ambient light, as for a quick setup for validation, there is no black cover for blocking environment light.

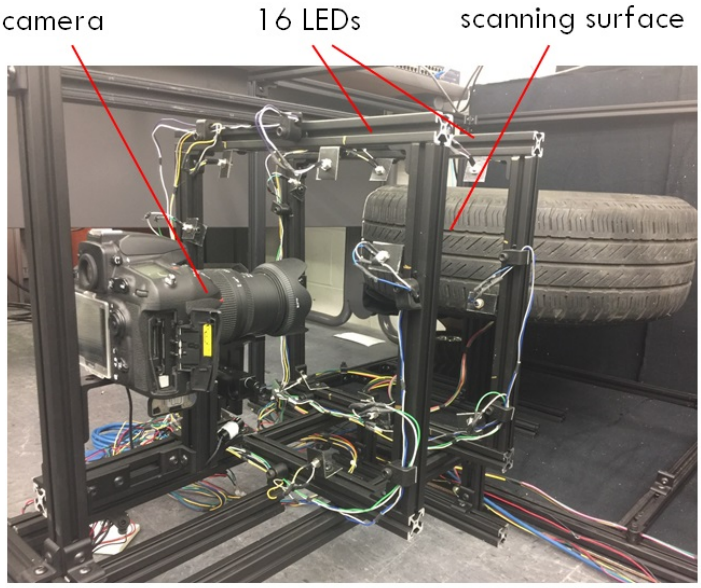


Figure 5.7: Real world experiment setup

Figure 5.8 shows the two real world objects, oreo cookie (Figure 5.8(a)) and tire tread (Figure 5.8(b)), used for the experiments. Due to the absence of ground truth of real world subjects, only rerendering error can be calculated and is used to evaluate though it is not the best criteria for dark surfaces. The mean rerendering error using SPS for the cookie is 9.3%, while the one for tire is 12.4%. Meanwhile, the mean rerendering errors of NIPS and DPS exceed 50% for all cases. It is noticed that the main reason for the poor performance of NIPS is the poor quality of initial values for the parameters of the parameterized model. Since NIPS is not designed specifically for the dark surfaces, the performance could be improved if some extra pre-processing steps have been done, which is beyond the scope of this dissertation.

Furthermore, Figure 5.9(a) and Figure 5.9(b) shows the depth maps generated using SNI from the calculated surface normal map, which can be used to qualitatively evaluate the


(a) cookie (b) tire

Figure 5.8: Scanning objects

performance of the proposed SPS technique. It is obvious from the figure that the shapes of both surfaces are recovered with fine details.

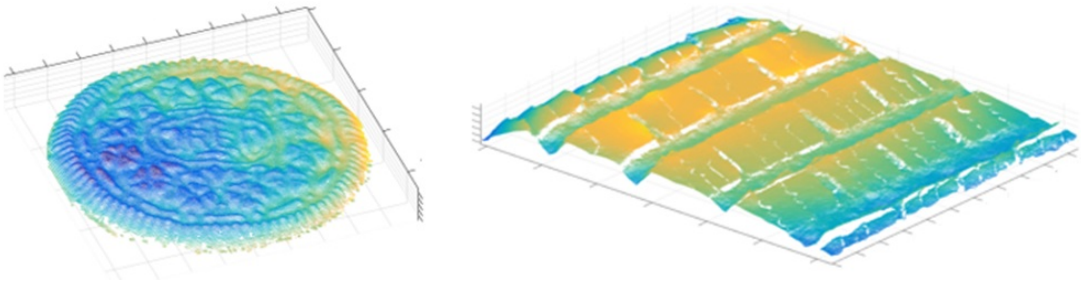

(a) cookie (b) tire

Figure 5.9: Constructed depth map using SNI

## 5.5 Conclusions and Future Works

This chapter has presented the technical details of specular photometry-based surface normal recovery technique, SPS, which obtains surface orientation through reversing specular micro-texture photometry and image formation procedure. The specular micro-texture photometry was introduced first, followed by the numerical solution of SPS problem with details. The proposed SPS was compared with state-of-the-art photometric stereo technique, NIPS,

on dark surfaces, with both synthesized scene and real world surfaces. For this specific application, SPS achieved better performance with shorter processing time.

This chapter has mainly focused on the derivative of SPS and much work is still left open, particularly the exploration of applications of SPS. It is also of particular interest for parameter studies of how lighting conditions will effect the performance of SPS.

# Chapter 6

# Circumferential Micro-texture 3D Profiling System

In this chapter, a system which is designed and developed to apply the proposed circumferential micro-texture 3D profiling approach is introduced. The measurement objectives are given at first, followed by the details on mechanical design and electrical design. The calibration procedures, which are necessary for the system to operate, are also presented in this chapter.

## 6.1 Measurement Objectives

The design objectives of the proposed system is to obtain a high resolution circumferential 3D profile of a cylindrical object such as tire tread. Real world surfaces are continuous surfaces and the traditional way to represent a continuous surface in 3D space is using parametric equations ([37]). However, due to the high resolution requirement and complexity of real world surfaces, it is difficult to find a universal parametric representation for all types of objects. On the other hand, point cloud, a set of data points in 3D space, is widely used as output format for 3D scanners. It can be directly converted to triangle mesh models ([64]) for the purpose of display, making both numerical analysis and visualization convenient. In this paper, point clouds will be used to represent 3D profiling result. It is noticed that in

this part, the tire tread is used as the example object, but the application can be extended to any cylindrical objects.

## 6.2 System Design

Figure 6.1 shows the mechanical design of the proposed system, which contains five parts: the main structure frame, the rotating sub-system, the lighting sub-system, the imaging sub-system, and a micro controller used to synchronize all the electrical components in the former three sub-systems. The total size of the proposed system is 1700mm×610mm×760mm. The system is designed to measure a 215/70R16 tire with a radius of 355mm and a width of 215mm. The main frame is constructed using t-slot aluminum extrusion. Black aluminum sheets are assembled to the system's six exterior surfaces to fully block ambient light. It is noted that all the black covers and some frames in Figure 6.1 are hidden for the purpose of clear visualization.

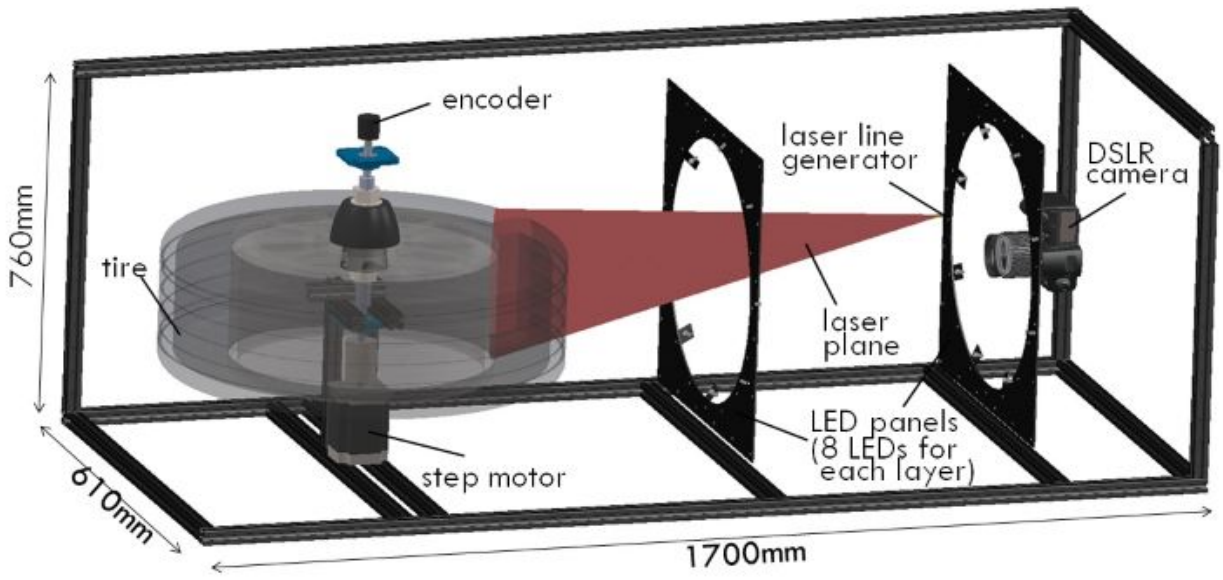


Figure 6.1: Mechanical design

Figure 6.2 shows the rotating sub-system. The rotating sub-system is constructed to rotate the tire for the purpose of circumferential scan. The tire is mounted on a rim and inflated. The rim is fixed on a rotation shaft through a cone and drum pair. The cone and drum pair is applied to guarantee that the rotation shaft and tire are coaxial. The rotation shaft has thread in the middle, so that the nuts can be employed to fasten the cone and drum to fix the rim on the rotation shaft. The rotation shaft is connected to a step motor through a shaft coupler. A rotatory encoder is connected to the other end of the rotation shaft. Two bearings are used at the top and bottom of the rotation shaft to fix the whole rotation sub-system to the main frame.

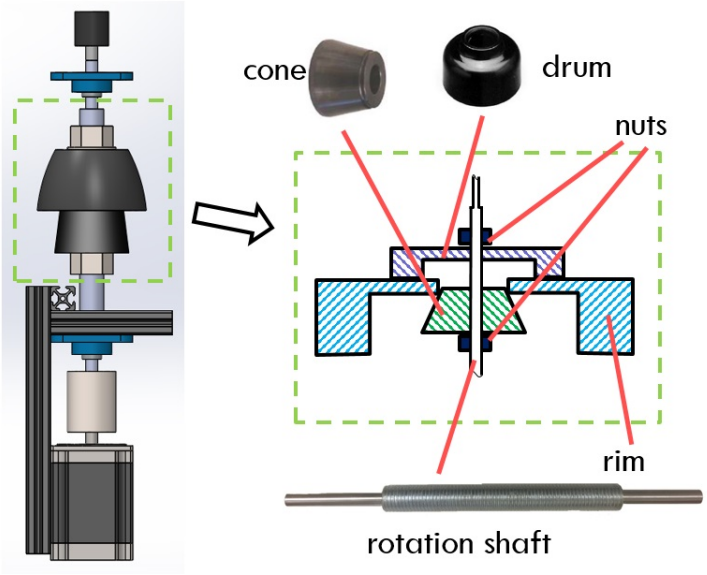


Figure 6.2: Rotating sub-system

The lighting sub-system is consisted of two layers of LEDs and one laser line generator. Each layer of LEDs contains eight white 5mm LEDs. The sixteen LEDs are uniformly distributed azimuth angles in 360°. All the first layer LEDs have a zenith angle of 35° while the second layer LEDs have a zenith angle of 15°. The laser line generator is composed by a laser and a splitter. The laser emits a narrow beam and the splitter splits the laser light beam into

a sheet-of-light, which is shown as a red triangular plane in Figure 6.1 and is referred to as laser plane in this dissertation. The laser line generator is placed such that the laser plane intersect with the tire in the middle of the field of view of the camera. The laser plane has a zenith angle of 15°.

The imaging sub-system contains a digital camera single-lens reflex camera with a resolution of 7680×5120. Give a tire (215/70R16) with a radius of 355mm and a width of 215mm and the tire's width covering ninety percents of the image's long side, the spatial resolution of the proposed system is $31\mu m$ per pixel, which means that the smallest element that can be profiled by the proposed system is $31\mu m \times 31\mu m$. The camera can observe a width of 140mm along tangent direction. To cover the whole tire with a tangent perimeter of 2230.5mm, a total number of seventeen PS measurements is required.

Figure 6.3 shows the electrical components of the proposed system. An MCU (Micro Control Unit) is used to synchronize the trigger of the DSLR camera, the line generator, the sixteen LEDs, the step motor and the encoder. A 110V power supply is used to provide the electrical power of the whole system. The 110V power is converted to 24V by the motor driver to drive the step motor and to 5V by a 110V/24V converter to provide power for the MCU. The proposed system needs to achieve two types of measurement, namely LS measurement and PS measurement. For LS measurement, the camera captures an image of the tire with the laser line projector on and for PS scanning, the camera captures 16 images of the tire under sixteen different single point lighting conditions by only turning on one of the LEDs at each time. One LS measurement gets the height profile of one cross-section of the tire surface whereas one PS measurement observes the tire surface area with a width of 140mm along tangent direction. In total two hundreds LS measurements and seventeen PS measurements will be conducted to measure the tire's circumferential surface.

Figure 6.4 shows the process chart of the proposed system. The system will automatically

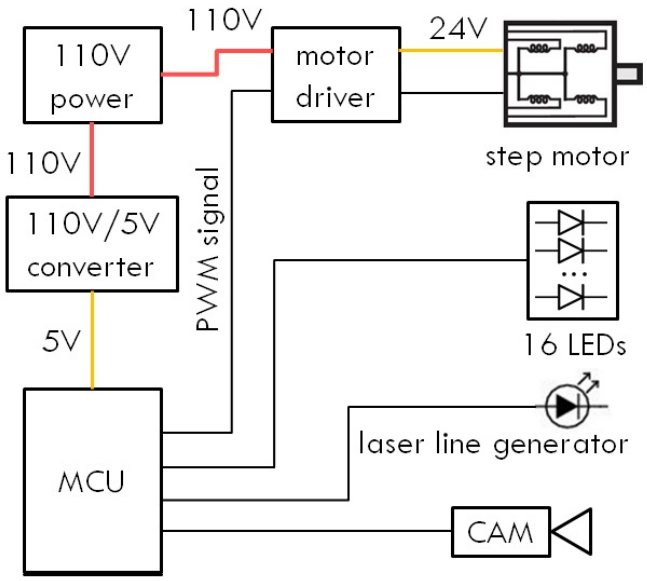


Figure 6.3: Electrical wiring

finish all the two type of measurement after a 'start' signal received. At first, the motor will continuously rotating with a slow speed with laser projector on. The camera captures the image of the tire surface under the illumination of the laser projector. Since a small exposure speed (50ms) is selected, the motion of the rotation will not blur the image. Then after the LS measurements, it will start to conduct PS measurements. For one PS measurement, the system turns on only one of the LEDs at one time, and the camera captures the image of the tire surface under the illumination of only that LED. In one PS measurement, the system takes sixteen images in total. After one PS measurement, the step motor rotates 21.2° to get all 360° measurement. The scanning time for the LS part is less than 10 minutes, while the total scanning time less than 30 minutes.

Figure 6.5 shows the image of the real developed system, which follows the mechanical and electrical design described above.

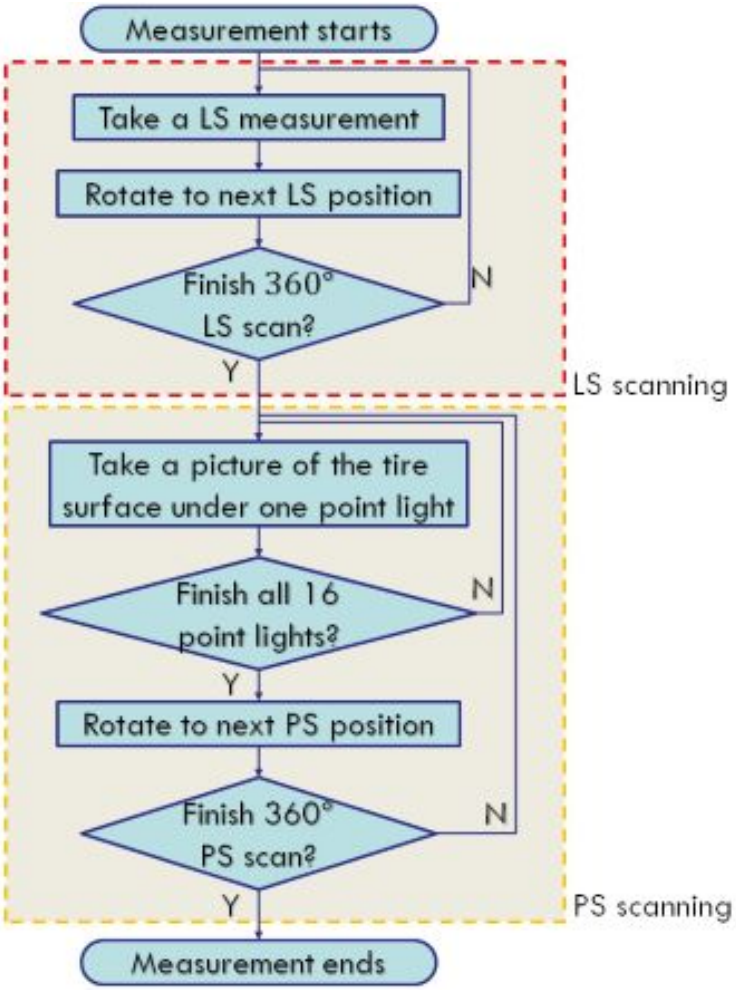


Figure 6.4: Measurement process chart

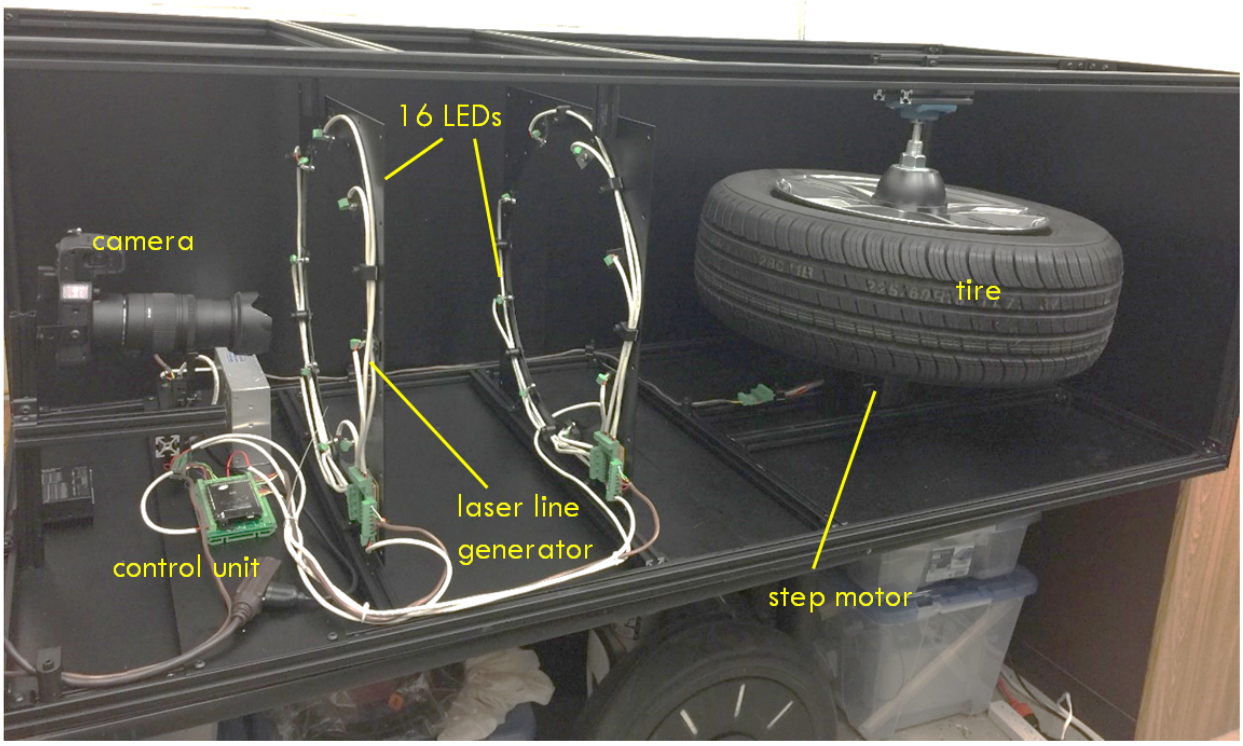


Figure 6.5: Developed measurement system

## 6.3 Calibration Procedures

To improve the performance of purposed system, several essential parameters need to be pre-calculated before the measurement process through calibration processes. More specifically, camera intrinsic parameters can be get from camera intrinsics calibration, the plane equation of the laser plane can be obtained through laser plane calibration, the illumination strength of each LEDs on the scene can be pre-determined via scene illumination calibration, and the lighting direction of the scene from each point illumination can be calculated in light direction calibration step.

### 6.3.1 Camera Intrinsics Parameters Calibration

To obtain camera intrinsic parameters, $f, o_x, o_y$, an approach similar to [100] is applied. A checkerboard is observed in multiple positions with various poses inside the field of view of the digital camera. Knowing the exact dimension of the checkerboard, the camera intrinsic parameters can be accurately determined through a closed-form solution and a nonlinear refinement. This approach can additionally estimate the extrinsic parameters of the checkerboard, namely $\boldsymbol{R}$ and $\boldsymbol{T}$, which are the position and orientation of camera with respect to the checkerboard. $\boldsymbol{R}$ and $\boldsymbol{T}$ will be used in following calibration steps.

### 6.3.2 Laser Plane Calibration

Parameters, $A_l, B_l, C_l, D_l$, of laser plane in Equation 3.5 are calculated through laser plane calibration. In this step, the same checkerboard is utilized again and observed by the same camera, but with additional laser illumination. Similar to camera Intrinsics calibration step, the checkerboard is placed in front of the camera and the laser line generator. The laser plane generated by the laser line generator intersects with the checkerboard and leaves a red line on its surface.

The position and orientation can be extracted using the approach described in [100]. Write the camera extrinsic parameters, the rotation matrix and transforming vector from the camera CS to the CS defined by the checkerboard, as $\boldsymbol{R}_c$ and $\boldsymbol{T}_c$, where $\boldsymbol{R}_c$ is a $3 \times 3$ matrix and $\boldsymbol{T}_c$ is a $3 \times 1$ vector. $\boldsymbol{R}_c$ can be written as $\boldsymbol{R}_c = [\boldsymbol{r}_1, \boldsymbol{r}_2, \boldsymbol{r}_3]$, where $\boldsymbol{r}_i (i = 1, 2, 3)$ is a $3 \times 1$ vector. The plane equation for the checkerboard can in camera CS be expressed using $\boldsymbol{r}_1$, $\boldsymbol{r}_2$, and $\boldsymbol{T}_c$ as:

$$A_c X + B_c Y + C_c Z + D_c = 0 \tag{6.1}$$

where

$$A_c = [1,0,0]^\top \cdot (\boldsymbol{r}_1 \times \boldsymbol{r}_2) \tag{6.2a}$$

$$B_c = [0,1,0]^\top \cdot (\boldsymbol{r}_1 \times \boldsymbol{r}_2) \tag{6.2b}$$

$$C_c = [0,0,1]^\top \cdot (\boldsymbol{r}_1 \times \boldsymbol{r}_2) \tag{6.2c}$$

$$D_c = -(\boldsymbol{r}_1 \times \boldsymbol{r}_2) \cdot \boldsymbol{T}_c \tag{6.2d}$$

Equation 6.1, combined with 3.3a and 3.3b, constitutes a system of linear equations with three equations and three unknowns, and the unknowns, which are the 3D coordinates in camera CS, of a laser dot, $[X_l, Y_l, Z_l]^\top$. The solution towards the 3D coordinate of the laser dot is given as:

$$X_l = \frac{x_l - c_x}{f} Z_l \tag{6.3a}$$

$$Y_l = \frac{y_l - c_y}{f} Z_l \tag{6.3b}$$

$$Z_l = -D_c \left( \frac{x_l - c_x}{f} A_c + \frac{y_l - c_y}{f} B_c + C_c \right)^{-1} \tag{6.3c}$$

where $x_l$ and $y_l$ are the pixel coordinates of the corresponding laser dot on the checkerboard. A dot is classified as a laser dot using a thresholding approach, similar to the one described in Section 3.2.

Figure 6.6 shows an example of images for laser plane calibration. As it is shown in the figure, multiple laser pixels can be detected as a point cloud, whose coordinates can be written as $\{\boldsymbol{p}_l\}^{k_{lc}}$. The superscript $\cdot^{k_{lc}}$ indicates the property of the ${k_{lc}}^{th}$ checkerboard pose for laser plane calibration. The corresponding coordinates of the laser points in camera CS is written as $\{\boldsymbol{P}_l\}^{k_{lc}}$. It is noted that $\{\boldsymbol{P}_l\}^{k_{lc}}$ represents the laser line on the checkerboard at the ${k_{lc}}^{th}$ checkerboard pose. With the checkerboard placed at $K_{lc}$ different pose, $K_{lc}$ different point

clouds are obtained as $\left\{ \{\boldsymbol{P}_l\}^{k_{lc}} \middle| k_{lc} \in \{1, ..., K_{lc}\} \right\}$. A plane equation can then be fitted using the laser points from the $K_{lc}$ point clouds as they belong to the same plane, which is the laser plane as:

$$[A_l, B_l, C_l, D_l]^T = \underset{A_l, B_l, C_l, D_l}{\arg\min} \sum_{l_{lc}=1}^{L_{lc}} \left(A_l X_{lc} + B_l Y_{lc} + C_l Z_{lc} + D_l\right)^2 \tag{6.4}$$

where $L_{lc}$ is the total number of points from all the $K_{lc}$ point clouds.

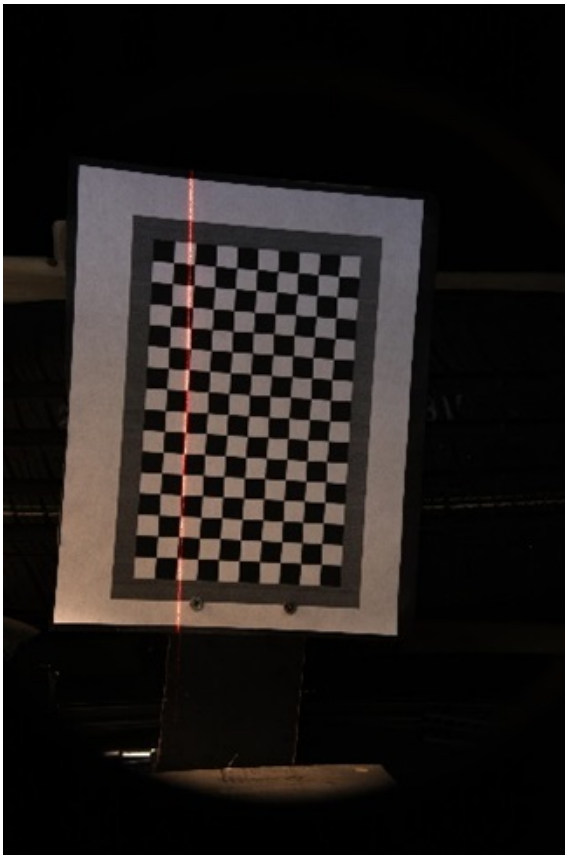

Figure 6.6: Image for laser plane calibration

### 6.3.3 Light Direction Calibration

The surface lighting direction $\bar{\boldsymbol{l}}_m^{(i,j)}$ for each pixel $(i,j) = (1,1),...,(R,C)$ under $k^{th}$ point light is calculated through this step.

Since the distance from the LEDs, which are used as light sources in the proposed system, to the scene and the size of the scene are of the same order of magnitude, the light sources cannot be considered as a remove illumination. The largest angle difference between the lighting directions of two points of the scene under the same point illumination could as large as 30°. In other words, the difference among the lighting directions across the scene is not negligible. Therefore the lighting direction across the whole scene need to be calculated in advance pixel by pixel.

Given the position of $m^{th}$ point illumination as $\boldsymbol{L}_m$, then the lighting direction of the $(i,j)^{th}$ reflectance patch of the scene, which is at $\boldsymbol{P}_{sc}^{(i,j)}$, can be calculated as the direction vector from $\boldsymbol{P}_{sc}^{(i,j)}$ to $\boldsymbol{L}_m$:

$$\bar{\boldsymbol{l}}_{sc,m}^{(i,j)} = \frac{\boldsymbol{L}_m - \boldsymbol{P}_{sc}^{(i,j)}}{||\boldsymbol{L}_m - \boldsymbol{P}_{sc}^{(i,j)}||} \tag{6.5}$$

where the subscript $\cdot_{sc}$ indicates the property of the scene. The problem of light direction calculation is then converted to obtain light position $\boldsymbol{L}_m$ for all the point illumination and the scene coordinate $\boldsymbol{P}_{sc}^{(i,j)}$ over the FoV of the camera.

Notice $\boldsymbol{P}_{sc}^{(i,j)}$ is actually the ultimate goal of the proposed system, which cannot be obtained during the calibration step. Instead, an appropriation of $\boldsymbol{P}_{sc}^{(i,j)}$ is used here for the calculation of $\bar{\boldsymbol{l}}_{sc,m}^{(i,j)}$. A reference plane, which is perpendicular to the camera's optical axis, in front of the camera and close enough to the observing scene, is created in the lighting direction calibration step. The plane equation of the reference plane is obtained using a checkerboard via the technique similar to the one in Section 6.3.1. Since the maximum depth difference between the reference board and the scene is less than 20mm, given the point illumination

is about 400mm away from the scene and the scene size is 215mm×140mm, the maximum angular difference between the calculated light direction and the exact light direction is 0.7°, which is neglectable.

The plane equation for the reference plane can be written as

$$A_r X + B_r Y + C_r Z + D_r = 0 \tag{6.6}$$

where $A_r, B_r, C_r, D_r$ can be calculated using Equation 6.2a-6.2d. It is noted that the coordinate on the reference plane $\boldsymbol{P}_r^{(i,j)} = [X_r^{(i,j)}, Y_r^{(i,j)}, Z_r^{(i,j)}]^\top$ also satisfies Equation 3.3a and 3.3b. The three unknown coordinates in $\boldsymbol{P}_r^{(i,j)}$ can then be calculated using the three linear equations, similarly to Equation 6.3a - 6.3c. Equation 6.5 can be then approximated using $\boldsymbol{P}_r^{(i,j)}$ as:

$$\bar{\boldsymbol{l}}_{sc,m}^{(i,j)} \approx \bar{\boldsymbol{l}}_{r,m}^{(i,j)} = \frac{\boldsymbol{L}_m - \boldsymbol{P}_r^{(i,j)}}{||\boldsymbol{L}_m - \boldsymbol{P}_r^{(i,j)}||} \tag{6.7}$$

The problem then becomes how to calibrate the position of the lighting source, $\boldsymbol{L}_m$. Figure 6.7 demonstrates the concept to calibrate $\boldsymbol{L}_m$. A chrome ball is placed on the reference plane, with its center at $\boldsymbol{C}$. A bright spot due to the $m^{th}$ illumination is observed from camera center at position $\boldsymbol{S}$. Notice that $\boldsymbol{C}$ and $\boldsymbol{S}$ can be both determined with the image captured by the camera and the plane equation of reference board. With the perfect sphere assumption, the surface normal at $\boldsymbol{S}$ can be expressed as:

$$\bar{\boldsymbol{n}} = \frac{\overrightarrow{\boldsymbol{CS}}}{\left|\overrightarrow{\boldsymbol{CS}}\right|} \tag{6.8}$$

The viewing direction can be calculated as

$$\bar{\boldsymbol{v}} = -\frac{\overrightarrow{\boldsymbol{OS}}}{\left|\overrightarrow{\boldsymbol{OS}}\right|} \tag{6.9}$$

where $\boldsymbol{O}$ is the origin of camera CS.

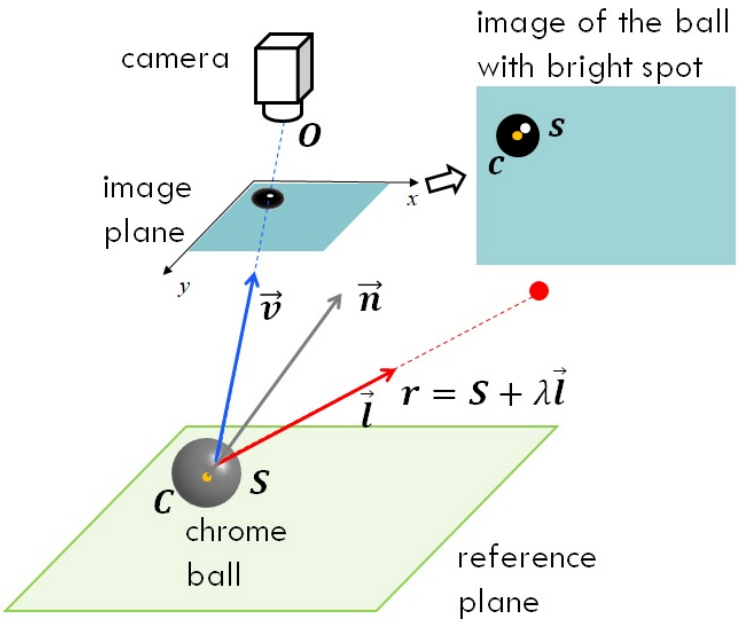


Figure 6.7: Schematic diagram in 2D with multiple chrome ball

Due to the specular reflection of the surface of the chrome ball, at $\boldsymbol{S}$, the normal vector, $\bar{\boldsymbol{n}}$, the incident vector (lighting direction), $\bar{\boldsymbol{l}}$, and the reflected vector (viewing direction), $\bar{\boldsymbol{v}}$ are in the same plane and $\bar{\boldsymbol{n}}$ bisects the angle between $\bar{\boldsymbol{v}}$ and $\bar{\boldsymbol{l}}$:

$$\bar{\boldsymbol{l}} = 2\left(\bar{\boldsymbol{v}} \cdot \bar{\boldsymbol{n}}\right)\bar{\boldsymbol{n}} - \bar{\boldsymbol{v}} \tag{6.10}$$

Then the vector expression of a line that passes the position of $m^{th}$ illumination is obtained as:

$$\boldsymbol{r} = \boldsymbol{S} + \lambda\bar{\boldsymbol{l}} \tag{6.11}$$

where $\lambda$ is a scalar.

Figure 6.8 uses 2D schematic diagram to show how to obtain the position of point illumination using the lines which suppose to pass it. By placing the chrome ball at different positions,

multiple lines, that pass the same point illumination, are obtained as $\boldsymbol{r}_1, ..., \boldsymbol{r}_K$.

The distance from the position of $m^{th}$ point illumination, $\boldsymbol{L}_m$, to the $k^{th}$ line $\boldsymbol{r}_k$ is calculated as:

$$\begin{aligned} \|\boldsymbol{d}_{m,k}\| &= \left\|(\boldsymbol{L}_m - \boldsymbol{S}_{m,k}) - \left((\boldsymbol{L}_m - \boldsymbol{S}_{m,k}) \cdot \bar{\boldsymbol{l}}_{m,k}\right) \bar{\boldsymbol{l}}_{m,k}\right\| \\ &= \left\|\left(\boldsymbol{I}_{3\times 3} - \bar{\boldsymbol{l}}_{m,k}\bar{\boldsymbol{l}}_{m,k}^T\right)(\boldsymbol{L}_m - \boldsymbol{S}_{m,k})\right\| \end{aligned} \tag{6.12}$$

If $\boldsymbol{r}_k$ passes $\boldsymbol{L}_m$, $\|\boldsymbol{d}_{m,k}\|$ should equal to 0 and two lines are sufficient to determine $\boldsymbol{L}_i$. However, due to the violation of assumptions such as perfect sphere and ideal specular reflection and also due to the existence of noises, the chrome ball need to be placed at $K(K \gg 2)$ different positions inside the camera's FoV to minimize the error. Then $\boldsymbol{L}_m$ can be calculated as:

$$\boldsymbol{L}_m = \arg\min_{\boldsymbol{L}_m} \sum_{k=1}^{K} \|\boldsymbol{d}_{m,k}\|^2 \tag{6.13}$$

The lighting direction can then be calculated using Equation 6.7.

### 6.3.4 Scene Illumination Calibration

The surface irradiance map, also known as scene illumination map, of the scene $E_m^{(i,j)}$, $(i,j) = (1,1), ...(R,C)$ and $m = 1, ..., M$ in Equation 3.14 can be calibrated through this step. It is noted that the image intensity map of tire surface $I_m^{(i,j)}$ under the $m^{th}$ point light in Equation 3.12 is a measurement parameter during the measurement step.

Figure 6.9 demonstrates the schematic diagram for scene illumination calibration. A gray card is placed at the same reference plane as described in Section 6.3.3. The camera takes $M$ pictures of the gray card under $M$ different lighting conditions. Each time only one LED is on. Gray card, mainly used as a standard reference object for exposure determination

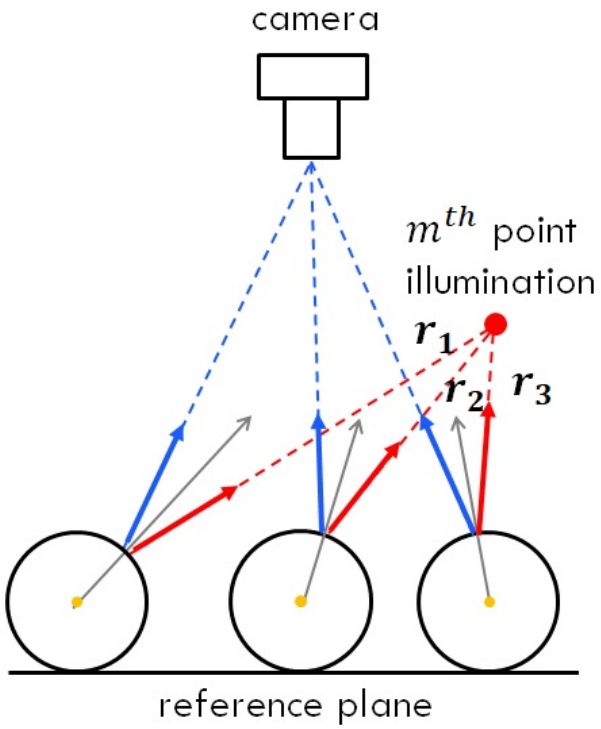


Figure 6.8: Schematic diagram in 3D with one chrome balls

in photography, can be considered as a Lambertian planar surface, whose reflection model satisfies Equation 3.16. The intensity is then calculated as:

$$I_{gc,m}^{(i,j)} = \gamma E_{gc,m}^{(i,j)} k_{gc}^{(i,j)} \left( \bar{\boldsymbol{n}}_{gc}^{(i,j)} \cdot \bar{\boldsymbol{l}}_{gc,k}^{(i,j)} \right) \tag{6.14}$$

$I_{gc,m}^{(i,j)}$ is the measurement of image intensity from camera, $\bar{\boldsymbol{n}}_{gc}^{(i,j)} = \bar{\boldsymbol{n}}_{ref}$, which is the pre-obtained surface normal of the reference plane, $\bar{\boldsymbol{l}}_{gc,k}^{(i,j)}$ is the lighting direction whose approach of calculation is introduced in Section 6.3.3. Given the homogeneous material across the gray card, $k_{gc}^{(i,j)}$ is assumed to be identical in the whole plane and assigned 1 without loss to generality. Move all the unknowns in Equation 6.14 to the left side of the equation and the

knowns parameters to the right, the equation becomes:

$$\gamma E_{gc,m}^{(i,j)} = \frac{I_{gc,m}^{(i,j)}}{k_{gc}^{(i,j)} \left( \bar{\boldsymbol{n}}_{gc}^{(i,j)} \cdot \bar{\boldsymbol{l}}_{gc,k}^{(i,j)} \right)} \tag{6.15}$$

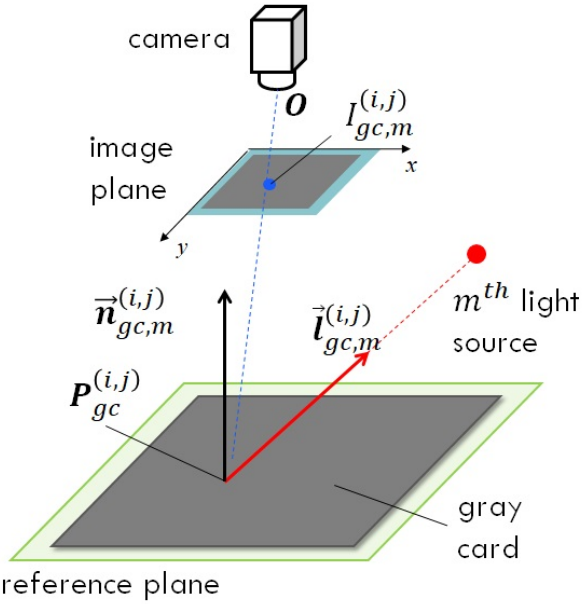


Figure 6.9: Schematic diagram of scene illumination calibration

Similar to the situation in Section 6.3.3, the calculation of $E_{sc,m}^{(i,j)}$ requires the knowledge of $\boldsymbol{P}_{sc}^{(i,j)}$, which is unknown at this stage. An approximation using $E_{gc,m}^{(i,j)}$ is used as the 20mm depth difference between the scene and reference plane makes little difference on the calculation of intensity of illumination. The corrected intensity at $\boldsymbol{P}^{(i,j)}$ of the scene can then calculated as

$$\hat{I}_{sc,m}^{(i,j)} = \frac{I_{sc,m}^{(i,j)}}{\gamma E_{sc,m}^{(i,j)}} \approx \frac{I_{sc,m}^{(i,j)}}{\gamma E_{gc,m}^{(i,j)}} = \frac{I_{sc,m}^{(i,j)} k_{gc}^{(i,j)} \left( \bar{\boldsymbol{n}}_{gc}^{(i,j)} \cdot \bar{\boldsymbol{l}}_{gc,k}^{(i,j)} \right)}{I_{gc,m}^{(i,j)}} \tag{6.16}$$

## 6.4 Conclusions and Future Works

In this chapter, the system which is designed and built to apply the proposed circumferential micro-texture 3D profiling approach has been introduced. The mechanical and electrical design of the system were described with details. Four calibration procedures, namely camera parameters calibration, laser plane calibration, light direction calibration, and scene illumination calibration, were explained.

The developed system mainly focuses on the measurement on tire with diameter smaller than 360mm. The extension of the system to objects with more general size remains unfinished. Furthermore, the modification of the system to a more portable version would also be interesting for future work.

# Chapter 7

# Experimental Results

In this chapter, experimental results using the developed system are given for the purpose of validation of the key techniques and display of the system's overall performance. The accuracy of the calibration procedures is given at first to ensure the precision of the pre-obtained parameters. The 3D profiling from one scan is shown next, followed by the circumferential 3D profiling result of a 215/70R16 tire.

## 7.1 Evaluation on Calibration Procedures

### 7.1.1 Camera Parameters Calibration

The experiment aims to evaluate the camera parameter calibration. The calibration process follows the standard procedure given by [100]. Thirty-five images of the same checkerboard with different positions and orientations were taken for this experiment. The checkerboard was placed at the camera's working distance, which is about 800mm in front of the camera inside the FoV of the camera. Figure 7.1 shows the relative positions and orientations with respect to the camera CS.

Figure 7.2(a) shows an example of the corner detection result of the checkerboard. Reprojection errors of the corners of the checkerboards are used to evaluate the camera parameters calibration result, which is shown in Figure 7.2(b). As it is shown in the figure, the mean

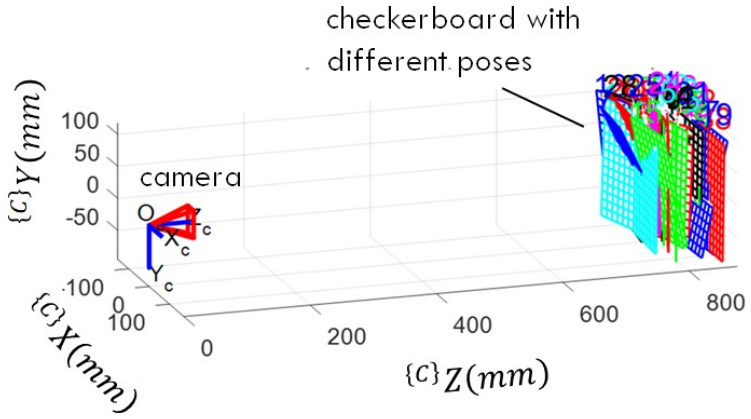


Figure 7.1: Relative poses of the checkerboard with respect to camera CS

reprojection errors are 1.538 pixels and 1.549 pixels in the $x$ and $y$ direction in image plane. Given the camera's resolution as $7680 \times 5120$, the reprojection percent errors are 0.02% and 0.03%.

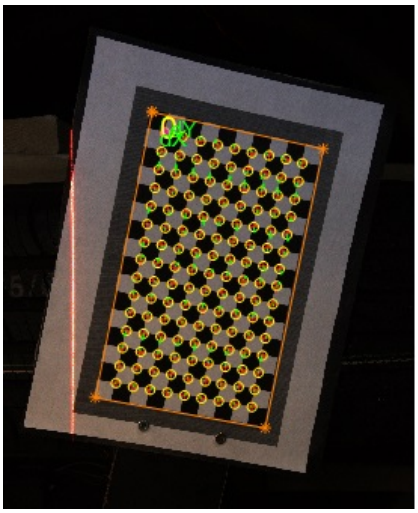

(a) Example of checkerboard corner detection

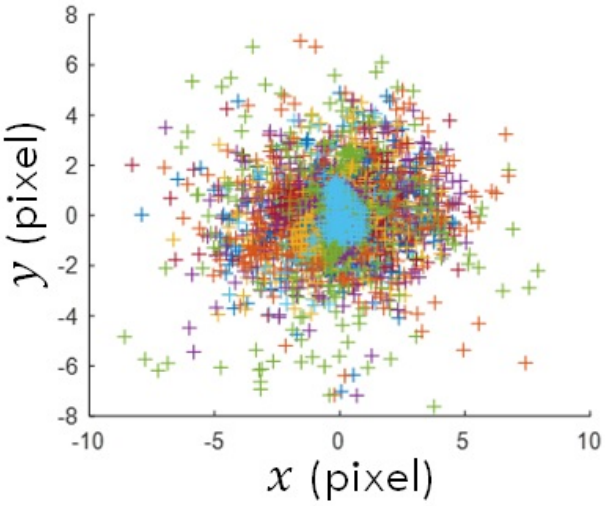


(b) Reprojection errors of checkerboard corners

Figure 7.2: Evaluation of camera parameters calibration

### 7.1.2 Laser Plane Calibration

The experiment aims to evaluate the laser plane calibration. The checkerboard was placed in front of the camera with approximate working distance, which is 800mm in front of the camera. The laser illumination was turned on during the evaluation procedure, leaving a laser line on the checkerboard for each image taken. Figure 7.3(a) shows an example of laser line detection. As it is shown in the figure, only the laser pixels inside the checkerboard are included for laser line detection result. The checkerboard was placed with $K_{lc} = 11$ different poses. As a consequence, $K_{lc} = 11$ laser lines were observed in this procedure. The laser plane was fitted using the $K_{lc} = 11$ laser lines. Figure 7.3(b) shows the relative poses of the laser lines and the laser plane with respect to camera CS. For each image captured, about 1000 pixels were classified as laser pixel, creating a total number of $L_{lc} = 11082$ points to fit the laser plane.

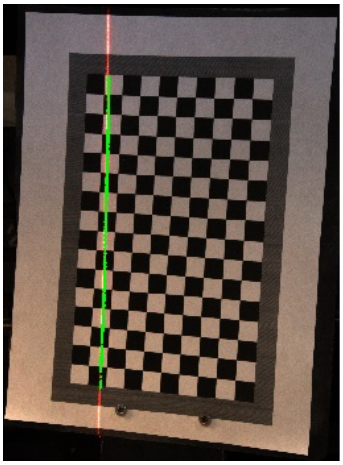

(a) Example of laser line detection

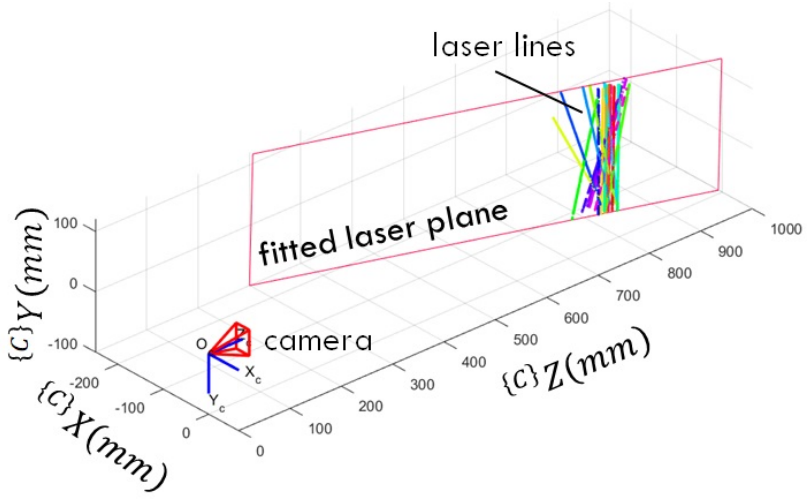


(b) Fitted laser plane using multiple laser lines

Figure 7.3: Evaluation of camera parameters calibration

The distances from the $L_{lc}$ laser points from all the $K_{lc}$ laser lines were used to evaluate the performance of laser plane calibration, which is shown in Figure 7.4. The average distance from laser points to fitted laser plane is $0.095mm$.

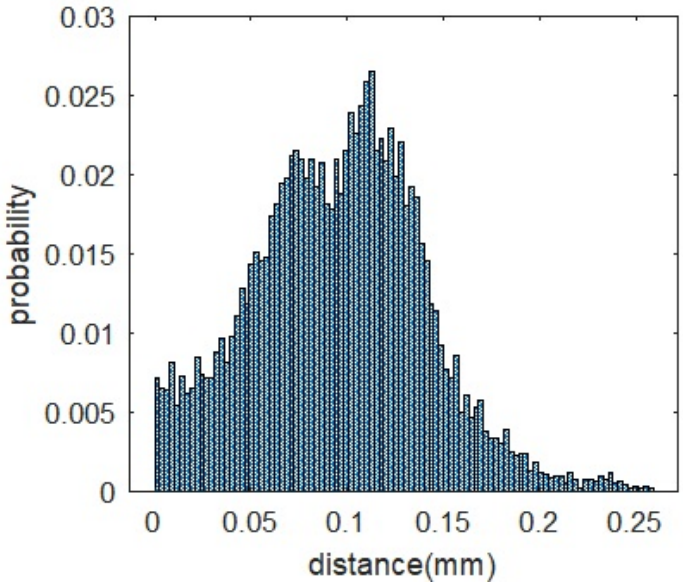


Figure 7.4: histogram of the distances from laser points to fitted laser plane

### 7.1.3 Light Direction Calibration

Figure 7.5 shows the image of chrome balls under one point illumination. The brightest spot is due to the specular reflection of the light source. Fifteen chrome balls were used to calibrate the positions of light sources. For each light source, fifteen lines, which are supposed to pass the light source, are generated. Their intersection is the position of light source. Due to the existence of noise and imperfect specular reflection, The fifteen illumination lines may not share one intersection. To account for that, a distance value, $\|\boldsymbol{d}_{m,k}\|$, is calculated using Equation 6.12. Cost function, Equation 6.13, is used to in the light direction calibration, minimizing which obtains the optimal position of the light source.

$\|\boldsymbol{d}_{i,k}\|$ is used to evaluate the performance of light position calibration. Figure 7.6 shows the box and whisker plot of $\|\boldsymbol{d}_{i,k}\|$. The average distance from the calculated light position to the illumination lines are 1.99mm. Given the fact that 5mm LEDs are used in the proposed system as the light sources, most of the calculated light positions fall inside the led bulb.

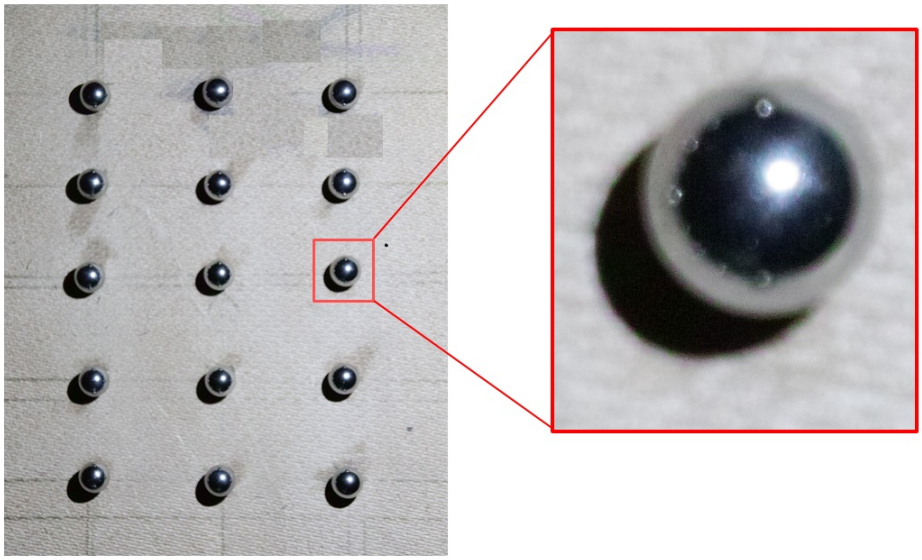

Figure 7.5: Image of chrome balls under point illumination

Given the size of the scene as 215mm×140mm and the LED is 400mm away from the scene, the 1.99mm uncertainty of the light position creates a maximum of 0.2° of uncertainty on light direction.

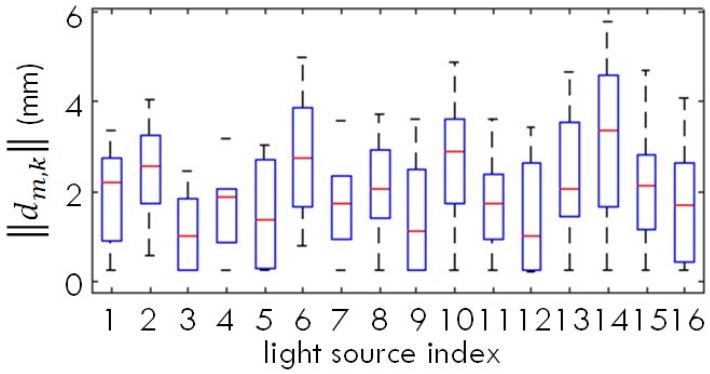


Figure 7.6: Box and whisker plot of $\|\boldsymbol{d}_{m,k}\|$

### 7.1.4 Scene Illumination Calibration Result

Figure 7.7(a) shows the image taken under one point illumination, while Figure 7.7(b) is the corresponding calculated scene illumination map. It is noted that the scene illumination from a point illumination is proportional to the inverse square of the distance from the source. As the LED is placed on the right to the gray card, the scene illumination is highest in the middle of right edge, since it is closest to the LED, and decreases as it goes away from the middle of the right edge, presenting a ring shape.

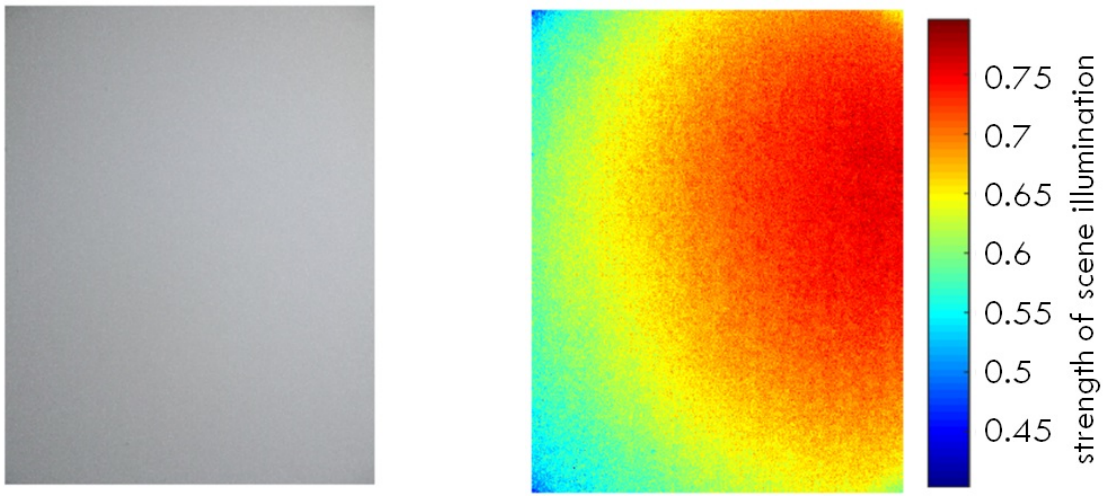


(a) Example of gray card image (b) Calculated scene illumination

Figure 7.7: Evaluation of scene illumination calibration

## 7.2 Results on Real Objects

### 7.2.1 Result from one Filed of View

Figure 7.8(a) shows the tire image of one FoV under one point illumination. As it can be seen from the image, the appearance of the tire surface under one point illumination satisfies the assumptions of SPS, which are 1. low diffuse reflection when the incident light is far

away from the critical incident direction; 2. high specular reflection when the incident light is close to the critical incident direction; 3. large specular highlight region. Figure 7.8(b) shows the rerendering error using the proposed SPS technique, with the colormap giving in Figure 7.8(c). By contrast, the rerendering error using NIPS technique is given in Figure 7.8(d). The result using DPS is not shown here as tire surface highly violates Lambertian assumption and results a large rerendering error if DPS is applied. Through the comparison of Figure 7.8(b) and Figure 7.8(d), the proposed SPS outperforms NIPS. The mean rerendering errors using SPS and NIPS are 12.9% and 21%, respectively. In conclusion, SPS is more suitable for objects with dark surface like tire.

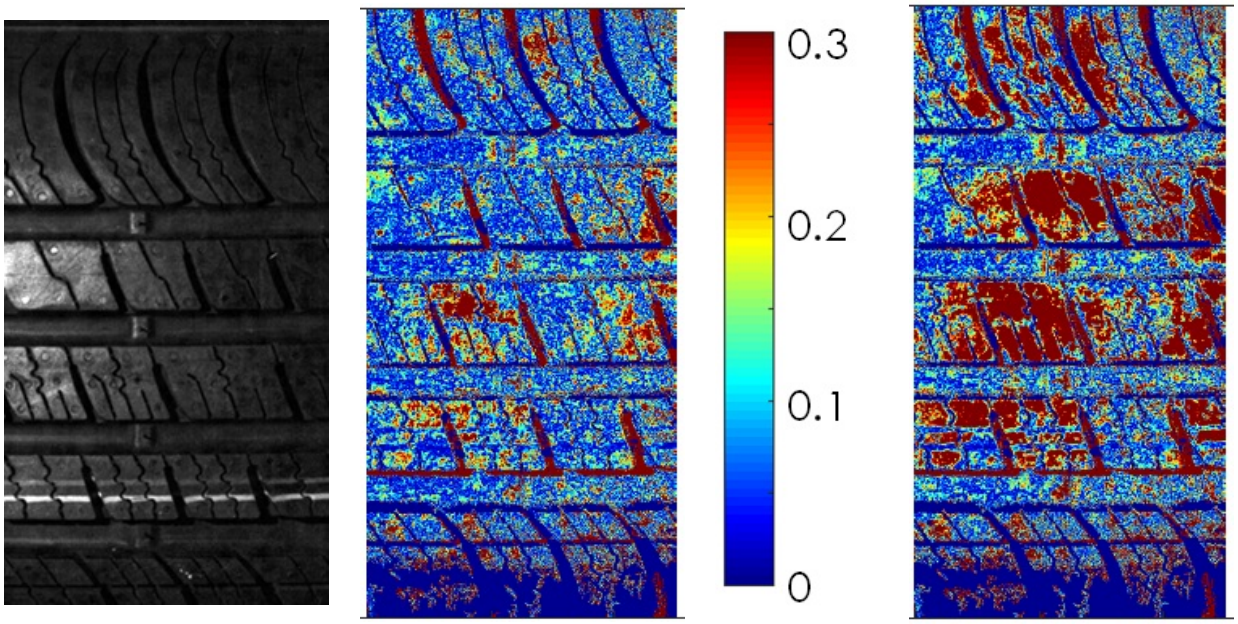


(a) tire image (b) SPS rerender error (c) colormap (d) NIPS rerender error

Figure 7.8: Experimental result from one field of view

Figure 7.9(a) shows the surface normal map calculated using SPS, while Figure 7.9(b) shows the reconstructed surface using SNI described in Section 3.3.4. As it can be seen from the figure, due to the lack of global constraints, the surface presents a swelling trend. Figure 7.9(c) shows the reconstructed surface using the proposed globally bounded 3D profiling

approach, with a figure of the close-up view with more details showing in 7.9(d). This two figures illuminate the strength of the proposed technique of constraining the reconstructed shape globally. With the constraints using the LS measurement, the surface shows more realistic shape of the tire. The sipes on the surface of tire is well reconstructed. It is noted that the surface looks flat due to the measured region is only a small section of the tire surface. The depth deviation is about 20mm inside this region.

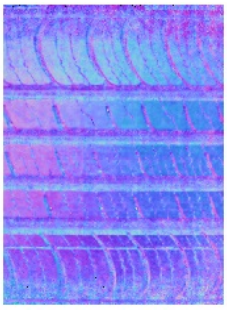

(a) surface normal map using SPS

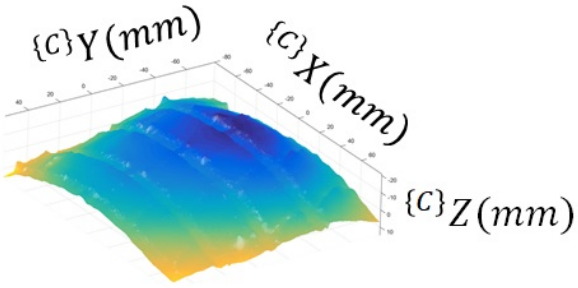


(b) SNI without correction

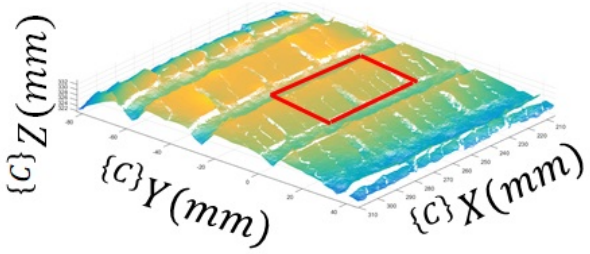


(c) SNI with correction

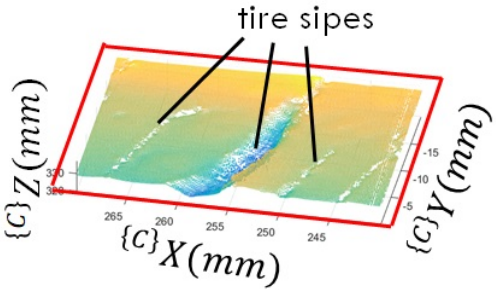


(d) close-up view of (c)

Figure 7.9: Surface reconstruction from one field of view

### 7.2.2 Circumferential Measurement

Table 7.1 shows the parameters for the experimental setup for circumferential measurement. The tire used in this experiment is 215/70R16 which fits the proposed system. The tire's tread was measured after 100miles, 200miles, 300miles usage. LS technique had two hundreds scans over the circumferential surface for each measurement, with 1.8° between two adjacent

scans, while PS technique scans seventeen times for each measurement, with 21° region covered by each scan.

| | **Parameter** | **Value** |
|---|---|---|
| Tire | Specification | 215/70R16 |
| | Distance at measurement (miles) | [100,200,300] |
| Spatial Resolution | Camera Resolution | 7680 pixel × 5120 pixel |
| | One FoV scan region | 215mm × 140mm |
| | Spatial resolution | 31$\mu$m |
| LS technique | Meas. Interval (deg) | 1.8 |
| | No. of scans / measurement | 200 |
| PS technique | # of LEDs | 16 |
| | Meas. Interval (deg) | 21 |
| | No. of scans / measurement | 17 |

Table 7.1: Experimental setup parameters

Figure 7.10 presents the result using the LS method and point registration, In total, two hundreds LS cross section are combined. The circumferential LS result serves as global constraints for the proposed hybrid approach.

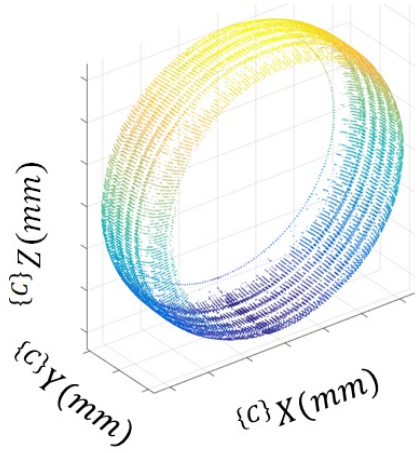


Figure 7.10: Circumferential LS measurement

Figure 7.11 shows the reconstruction result of the whole tire using the proposed approach. Figure 7.11(a)-(c) show the depth map of the tire tread after 100 miles/200 miles/300 miles

usage respectively. The depth map is generated from the 3D profiling with the definition which is shown in Figure 7.11(e). Figure 7.11(d) shows a zoomed view of one section of the depth map of the one after 100 miles usage. Figure 7.11(e) also shows the color quantity for tire depth. As it is shown in the figures, the depth map from 100 miles usage to the one from 300 miles usage shows a decreasing tread depth.

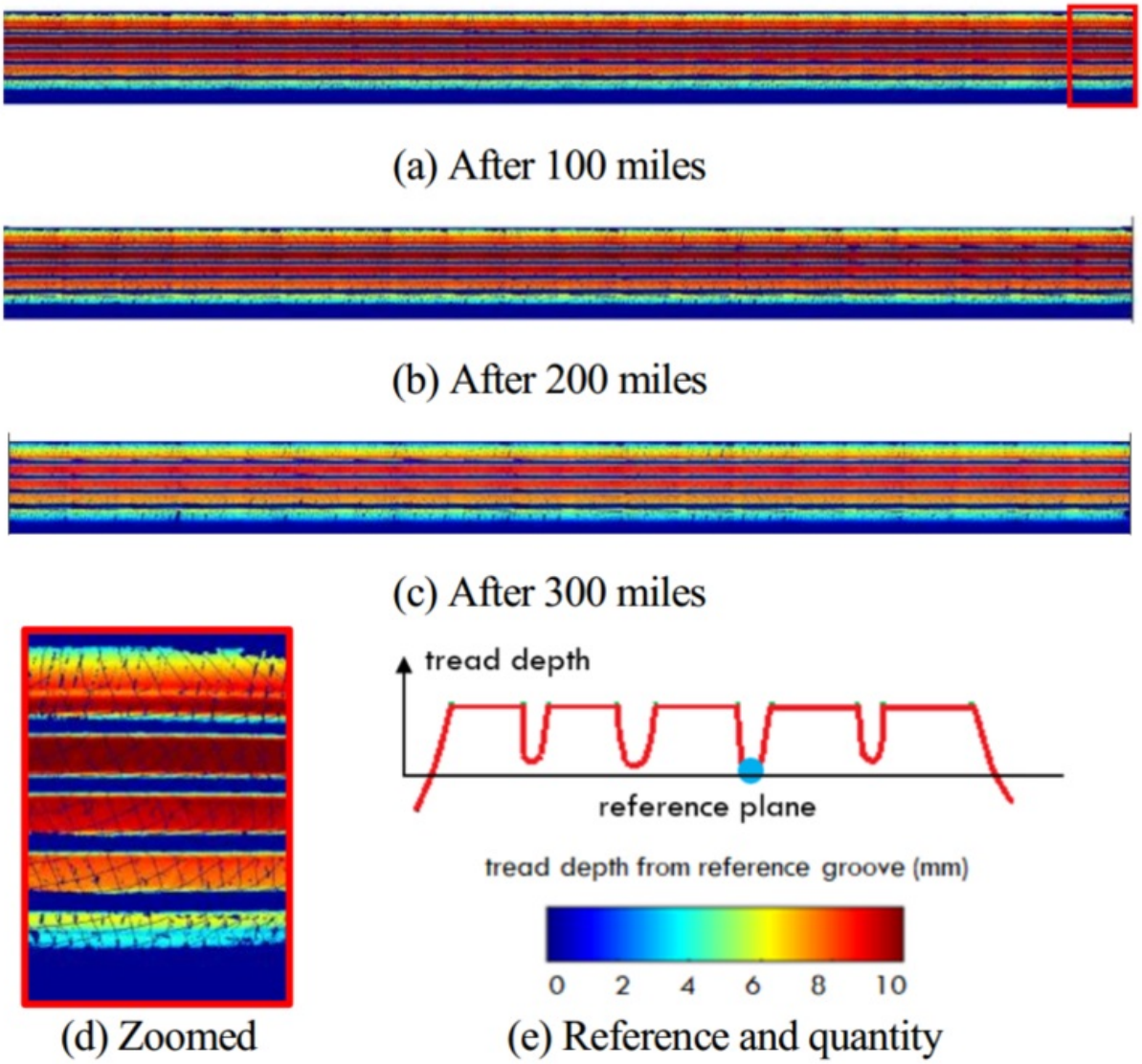


Figure 7.11: (a)-(c) 3D reconstruction result after 100 miles/200 miles/300 miles (d) Zoomed 3D reconstruction result of after 100 miles measurement (e) Reference and quantity

Figure 7.12 shows the tire wear measurement result from 100 miles usage to 200 miles usage. Figure 7.12(a) shows the tire wear result of the whole tire while Figure 7.12(b) gives a zoomed view. Figure 7.12(c) shows the definition of the tire wear measurement from before measurement (green) and after measurement (red), as the reference plane, which is defined by the groove, remain untouched during the tire wear test. The color quantity for the tire wear measurement is shown in Figure 7.12(d). The mean tire wear measured from after 100 miles usage and 200 miles usage is about 0.12mm. As it is shown in the result, the tire wear measurement achieves an accuracy of 100$\mu$m.

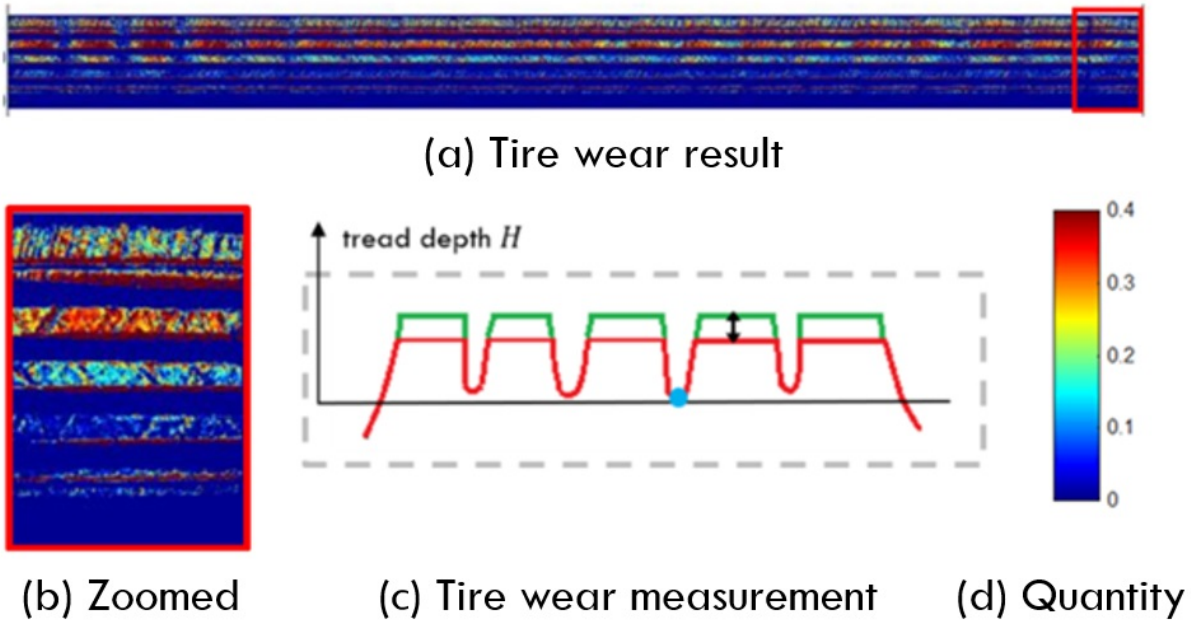


Figure 7.12: (a) Tire wear result between after 100 miles and 200 miles (b) Zoomed tire wear result (c) Tire wear definition (d) Quantity

## 7.3 Conclusions and Future Works

In this chapter, the experiments to validate the calibration procedures have been introduced first with results. The experimental results using the proposed approach and the developed system were then given next for one FoV measurement and the circumferential measurement. As it was shown in the experimental results, the developed system is able to measure the target surface with 31$\mu$m spatial resolution and succeeds circumferentially measuring cylindrical objects. The tire wear measurement using the developed system achieves an accuracy of 100$\mu$m.

The overall performance of the proposed approach and the developed system were evaluated with tire surface. More experiments could be done with more general objects.

# Chapter 8

# Conclusions and Future Work

The dissertation is summarized in this chapter. The chapter starts with the conclusions of the dissertation regarding specular micro-texture photometry for circumferential 3D profiling, and finishes with directions for potential future work.

## 8.1 Conclusions

The dissertation has presented three major contributions. First, the specular component in the micro-texture photometry was investigated to propose the pixel-level 3D profiling. The intensities of the same pixel from different images, which are taken under different lighting conditions are different. The specular components are used to recover the surface normal of the corresponding surface patch of the target surface. Consequently, the proposed specular-photometry-based technique produces pixel-wise measurement on surface normal. The proposed specular photometry-based technique was compared with state-of-the-art technique on dark surfaces, with both synthesized scene and real world surfaces. For this specific application, the proposed technique achieved better performance with shorter processing time.

The second contribution is the usage of the conventional circumferential 3D profiling approach for enhancing the 3D profiling using the proposed specular-photometry-based technique. The problem was well formulated and the methodology of the proposed approach

was explained. The result of 3D profiling from the integration using the surface normal obtained from the proposed specular-photometry-based technique suffers from accumulative error. On the other hand, the result of 3D profiling via the conventional approach is sparse due to its nature. The proposed approach was able to achieve pixel-resolution globally bounded profiling because of the dense surface normal measurement from the proposed specular-photometry-based technique and the constraints from the conventional approach.

The third contribution is the development of a system to apply the proposed circumferential specular-photometry-based 3D profiling approach. The developed system is not only able to acquire data and but also to provide different lighting conditions for both the specular-photometry-based technique and conventional approach using a digital single-lens reflex camera and different lighting devices. With a step motor to rotate the object for three hundreds and sixty degrees, the system is able to achieve circumferential scanning. The mechanical and electrical design of the system were described with details. Four calibration procedures, namely camera parameters calibration, laser plane calibration, light direction calibration, and scene illumination calibration, were explained. Several experiments to validate the performance of the proposed approach and the developed system has been fulfilled. As it was shown in the experimental results, the developed system is able to measure the target surface with 31$\mu$m spatial resolution and succeeds circumferentially measuring cylindrical objects. The developed system has also been used for the purpose of tire wear measurement. The tire wear measurement using the developed system achieves an accuracy of 100$\mu$m.

## 8.2 Future Work

For the proposed photometry-based technique, this dissertation mainly focused on the derivative of SPS. The exploration of applications of this technique is still open. The parameter

studies of how lighting conditions will effect its performance is some direction to explore.

The dissertation finishes the derivative of circumferential 3D profiling in Cartesian CS. Its variation in Cylindrical CS may ease the calculation and improve the accuracy, which remains open for exploration.

For the overall approach and the developed system, the application in this dissertation is restricted due to the requirement of the funded project. The extension to objects with more general size and more general material remains unfinished.

# Bibliography


[1] Jens Ackermann, Fabian Langguth, Simon Fuhrmann, and Michael Goesele. Photometric stereo for outdoor webcams. In *Computer Vision and Pattern Recognition (CVPR), 2012 IEEE Conference on*, pages 262–269. IEEE, 2012.

[2] Neil Alldrin, Todd Zickler, and David Kriegman. Photometric stereo with non-parametric and spatially-varying reflectance. In *2008 IEEE Conference on Computer Vision and Pattern Recognition*, pages 1–8. IEEE, 2008.

[3] Stephen T Barnard. Interpreting perspective images. *Artificial intelligence*, 21(4): 435–462, 1983.

[4] Ronen Basri and David W Jacobs. Lambertian reflectance and linear subspaces. *IEEE transactions on pattern analysis and machine intelligence*, 25(2):218–233, 2003.

[5] Andrew Blake and G Brelstaff. Specular stereo. In *IJCAI*, volume 2, pages 973–976, 1985.

[6] James F Blinn. A generalization of algebraic surface drawing. *ACM transactions on graphics (TOG)*, 1(3):235–256, 1982.

[7] Gary Bradski and Adrian Kaehler. *Learning OpenCV: Computer vision with the OpenCV library.* " O'Reilly Media, Inc.", 2008.

[8] AL Browne. Predicting the effect of tire tread pattern design on thick film wet traction. *Tire Science and Technology*, 5(1):6–28, 1977.

[9] Fabio Bruno, Stefano Bruno, Giovanna De Sensi, Maria-Laura Luchi, Stefania Mancuso, and Maurizio Muzzupappa. From 3d reconstruction to virtual reality: A complete

methodology for digital archaeological exhibition. *Journal of Cultural Heritage*, 11(1): 42–49, 2010.

[10] Joachim Burger. Method and gauge for measuring the tread depth of a motor vehicle tire, April 20 1999. US Patent 5,895,845.

[11] Cong Chen, Mengyu Song, and Tomonari Furukawa. Three-dimensional measurement of crash test frame deformation using high speed camera fusion and motion model. In *JSAE*, 2019.

[12] Cong Chen, Mengyu Song, Tomonari Furukawa, Azusa Nakata, and Shinsuke Shibata. Rnn based online automobile deformation measurement for active safety. In *Fast Zero*, 2019.

[13] Cong Chen, Mengyu Song, Tomonari Furukawa, Azusa Nakata, and Shibata Shinsuke. Automobile structure three-dimensional deformation measurement during crash using multi-camera vision. In *Fast Zero*, 2019.

[14] JR Cho, KW Kim, WS Yoo, and SI Hong. Mesh generation considering detailed tread blocks for reliable 3d tire analysis. *Advances in engineering software*, 35(2):105–113, 2004.

[15] Scott J Coe, Paul B Wilson, and Vladimir Roth. Apparatus and related methods for obtaining tire profiles including the tread and both sidewalls, August 4 1998. US Patent 5,789,668.

[16] E North Coleman Jr and Ramesh Jain. Obtaining 3-dimensional shape of textured and specular surfaces using four-source photometry. *Computer graphics and image processing*, 18(4):309–328, 1982.

[17] Yan Cui, Sebastian Schuon, Derek Chan, Sebastian Thrun, and Christian Theobalt. 3d shape scanning with a time-of-flight camera. In *2010 IEEE Computer Society Conference on Computer Vision and Pattern Recognition*, pages 1173–1180. IEEE, 2010.

[18] Andrew W Fitzgibbon, Geoff Cross, and Andrew Zisserman. Automatic 3d model construction for turn-table sequences. In *European Workshop on 3D Structure from Multiple Images of Large-Scale Environments*, pages 155–170. Springer, 1998.

[19] Christofer Fröhlich, Markus Mettenleiter, et al. Terrestrial laser scanning–new perspectives in 3d surveying. *International archives of photogrammetry, remote sensing and spatial information sciences*, 36(Part 8):W2, 2004.

[20] Jason Geng. Structured-light 3d surface imaging: a tutorial. *Advances in Optics and Photonics*, 3(2):128–160, 2011.

[21] Athinodoros S Georghiades. Incorporating the torrance and sparrow model of reflectance in uncalibrated photometric stereo. In *iccv*, volume 3, page 816, 2003.

[22] Mir Hamid Reza Ghoreishy. Finite element analysis of the steel-belted radial tyre with tread pattern under contact load. *Iranian Polymer Journal*, 15(8):667–674, 2006.

[23] Dan B Goldman, Brian Curless, Aaron Hertzmann, and Steven M Seitz. Shape and spatially-varying brdfs from photometric stereo. *IEEE Transactions on Pattern Analysis and Machine Intelligence*, 32(6):1060–1071, 2010.

[24] Mark F Hansen, Gary A Atkinson, Lyndon N Smith, and Melvyn L Smith. 3d face reconstructions from photometric stereo using near infrared and visible light. *Computer Vision and Image Understanding*, 114(8):942–951, 2010.

[25] Richard Hartley and Andrew Zisserman. *Multiple view geometry in computer vision*. Cambridge university press, 2003.

[26] Carlos Hernández, George Vogiatzis, Gabriel J Brostow, Bjorn Stenger, and Roberto Cipolla. Non-rigid photometric stereo with colored lights. In *2007 IEEE 11th International Conference on Computer Vision*, pages 1–8. IEEE, 2007.

[27] Carlos Hernandez, George Vogiatzis, and Roberto Cipolla. Multiview photometric stereo. *IEEE Transactions on Pattern Analysis and Machine Intelligence*, 30(3):548–554, 2008.

[28] Aaron Hertzmann and Steven M Seitz. Example-based photometric stereo: Shape reconstruction with general, varying brdfs. *IEEE Transactions on Pattern Analysis and Machine Intelligence*, 27(8):1254–1264, 2005.

[29] Berthold Klaus Paul Horn. Extended gaussian images. *Proceedings of the IEEE*, 72 (12):1671–1686, 1984.

[30] Shih Yen Huang and You Jyun Syu. Based on the texture analysis to inspect the tread worn status on the tire. In *Intelligent Information Hiding and Multimedia Signal Processing (IIH-MSP), 2014 Tenth International Conference on*, pages 431–434. IEEE, 2014.

[31] Shih-Yen Huang, Yen-Cheng Chen, and Jih-Kai Wang. Measurement of tire tread depth with image triangulation. In *2016 International Symposium on Computer, Consumer and Control (IS3C)*, pages 303–306. IEEE, 2016.

[32] Katsushi Ikeuchi. Determining surface orientations of specular surfaces by using the photometric stereo method. *IEEE Transactions on Pattern Analysis and Machine Intelligence*, (6):661–669, 1981.

[33] David Jenn. *Radar and laser cross section engineering*. American Institute of Aeronautics and Astronautics, Inc., 2005.

[34] Hong Jin, Fupei Wu, Chun Yang, Lian Chen, and Shengping Li. A review of 3-d reconstruction based on machine vision. In *International Conference on Intelligent Robotics and Applications*, pages 195–203. Springer, 2014.

[35] Thomas M Kaiser and Horst Katterwe. The application of 3d-microprofilometry as a tool in the surface diagnosis of fossil and sub-fossil vertebrate hard tissue. an example from the pliocene upper laetolil beds, tanzania. *International Journal of Osteoarchaeology*, 11(5):350–356, 2001.

[36] Christos A Kapoutsis, CP Vavoulidis, and Ioannis Pitas. Morphological iterative closest point algorithm. *IEEE Transactions on Image Processing*, 8(11):1644–1646, 1999.

[37] Anatolij Borisovič Katok and Vaughn Climenhaga. *Lectures on Surfaces:(almost) everything you wanted to know about them*, volume 46. American Mathematical Soc., 2008.

[38] Greg Kay and Terry Caelli. Estimating the parameters of an illumination model using photometric stereo. *Graphical models and image processing*, 57(5):365–388, 1995.

[39] Csaba Kazó and Levente Hajder. High-quality structured-light scanning of 3d objects using turntable. In *2012 IEEE 3rd International Conference on Cognitive Infocommunications (CogInfoCom)*, pages 553–557. IEEE, 2012.

[40] Yair Kipman. Non-contact vision based inspection system for flat specular parts, February 25 2003. US Patent 6,525,810.

[41] Stijn Klijn, Nicolaas J Reus, Charlotte M van der Sommen, and Victor Arni DP Sicam. Accuracy of a novel specular reflection technique for measurement of total

corneal astigmatism. *Investigative Ophthalmology & Visual Science*, 56(7):1903–1903, 2015.

[42] SH Koehne, B Matute, and R Mundl. Evaluation of tire tread and body interactions in the contact patch. *Tire Science and Technology*, 31(3):159–172, 2003.

[43] Pradeep Lall, Shantanu Deshpande, Junchao Wei, and Jeff Suhling. Non-destructive crack and defect detection in sac solder interconnects using cross-sectioning and x-ray micro-ct. In *2014 IEEE 64th Electronic Components and Technology Conference (ECTC)*, pages 1449–1456. IEEE, 2014.

[44] Jack L Lancaster, Nicolas Walsh, and Virgil Faulkner. Basic theory, design, and preliminary evaluation of a laser scanner for shape sensing below-the-knee amputees. *Medical physics*, 17(2):305–310, 1990.

[45] Douglas Lanman, Daniel Crispell, and Gabriel Taubin. Surround structured lighting for full object scanning. In *Sixth International Conference on 3-D Digital Imaging and Modeling (3DIM 2007)*, pages 107–116. IEEE, 2007.

[46] Olivier Le Maitre, Manfred Süssner, and Cesar Zarak. Evaluation of tire wear performance. Technical report, SAE Technical Paper, 1998.

[47] Boren Li and Tomonari Furukawa. Microtexture road profiling system using photometric stereo. *Tire Science and Technology*, 43(2):117–143, 2015.

[48] Boren Li and Tomonari Furukawa. Photometric stereo under dichromatic reflectance framework dealing with non-lambertian surfaces. In *Multisensor Fusion and Integration for Intelligent Systems (MFI), 2015 IEEE International Conference on*, pages 139–144. IEEE, 2015.

[49] Hao Li. Analysis of off-road tire-soil interaction through analytical and finite element methods. 2013.

[50] Kaiming Li, Lei Guo, Gang Li, Jingxin Nie, Carlos Faraco, Qun Zhao, Stephen Miller, and Tianming Liu. Gyral folding pattern analysis via surface profiling. In *International Conference on Medical Image Computing and Computer-Assisted Intervention*, pages 313–320. Springer, 2009.

[51] Chen Liang, Guolin Wang, Dengfeng An, and Yinwei Ma. Tread wear and footprint geometrical characters of truck bus radial tires. *Chinese Journal of Mechanical Engineering*, 26(3):506–511, 2013.

[52] Fotios Logothetis, Roberto Mecca, and Roberto Cipolla. A differential volumetric approach to multi-view photometric stereo. *arXiv preprint arXiv:1811.01984*, 2018.

[53] Wan-Chun Ma, Tim Hawkins, Pieter Peers, Charles-Felix Chabert, Malte Weiss, and Paul Debevec. Rapid acquisition of specular and diffuse normal maps from polarized spherical gradient illumination. In *Proceedings of the 18th Eurographics conference on Rendering Techniques*, pages 183–194. Eurographics Association, 2007.

[54] Daisuke Miyazaki, Kenji Hara, and Katsushi Ikeuchi. Median photometric stereo as applied to the segonko tumulus and museum objects. *International Journal of Computer Vision*, 86(2-3):229, 2010.

[55] Euan Morrison. The development of a prototype high-speed stylus profilometer and its application to rapid 3d surface measurement. *Nanotechnology*, 7(1):37, 1996.

[56] Sanjay Noronha and Ramakant Nevatia. Detection and modeling of buildings from multiple aerial images. *IEEE Transactions on pattern analysis and machine intelligence*, 23(5):501–518, 2001.

[57] Matteo Novara, Kees Joost Batenburg, and Fulvio Scarano. Motion tracking-enhanced mart for tomographic piv. *Measurement science and technology*, 21(3):035401, 2010.

[58] Xufang Pang, Rynson WH Lau, Zhan Song, Yangyan Li, and Shengfeng He. A tool-free calibration method for turntable-based 3d scanning systems. *IEEE computer graphics and applications*, 36(1):52–61, 2014.

[59] Soon-Yong Park and Murali Subbarao. A multiview 3d modeling system based on stereo vision techniques. *Machine Vision and Applications*, 16(3):148–156, 2005.

[60] Tomas Plachetka. Pov ray: persistence of vision parallel raytracer. In *Proc. of Spring Conf. on Computer Graphics, Budmerice, Slovakia*, volume 123, 1998.

[61] Rodrigo de Oliveira Plotze, Maurício Falvo, Juliano Gomes Pádua, Luís Carlos Bernacci, Maria Lúcia Carneiro Vieira, Giancarlo Conde Xavier Oliveira, and Odemir Martinez Bruno. Leaf shape analysis using the multiscale minkowski fractal dimension, a new morphometric method: a study with passiflora (passifloraceae). *Canadian Journal of Botany*, 83(3):287–301, 2005.

[62] C Poelma, JM Mari, N Foin, M-X Tang, R Krams, CG Caro, PD Weinberg, and J Westerweel. 3d flow reconstruction using ultrasound piv. *Experiments in fluids*, 50 (4):777–785, 2011.

[63] Beatriz Remeseiro, Javier Tarrío-Saavedra, Mario Francisco-Fernández, Manuel G Penedo, Salvador Naya, and Ricardo Cao. Automatic detection of defective crankshafts by image analysis and supervised classification. *The International Journal of Advanced Manufacturing Technology*, 105(9):3761–3777, 2019.

[64] Fabio Remondino. From point cloud to surface: the modeling and visualization prob-

lem. *International Archives of photogrammetry, Remote Sensing and spatial information sciences*, 34, 2003.

[65] Fabio Remondino and Sabry El-Hakim. Image-based 3d modelling: a review. *The Photogrammetric Record*, 21(115):269–291, 2006.

[66] Mingjun Ren, Xi Wang, Gaobo Xiao, Minghan Chen, and Lin Fu. Fast defect inspection based on data-driven photometric stereo. *IEEE Transactions on Instrumentation and Measurement*, 68(4):1148–1156, 2018.

[67] Roland Ruiters and Reinhard Klein. Heightfield and spatially varying brdf reconstruction for materials with interreflections. In *Computer Graphics Forum*, volume 28, pages 513–522. Wiley Online Library, 2009.

[68] Joaquim Salvi, Jordi Pages, and Joan Batlle. Pattern codification strategies in structured light systems. *Pattern recognition*, 37(4):827–849, 2004.

[69] Joaquim Salvi, Sergio Fernandez, Tomislav Pribanic, and Xavier Llado. A state of the art in structured light patterns for surface profilometry. *Pattern recognition*, 43(8): 2666–2680, 2010.

[70] Steven A Shafer. Using color to separate reflection components. *Color Research & Application*, 10(4):210–218, 1985.

[71] Y-Q Shen and TJ Ypma. Solving nonlinear systems of equations with only one nonlinear variable. *Journal of computational and applied mathematics*, 30(2):235–246, 1990.

[72] Mengyu Song and Tomonari Furukawa. Specular photometric stereo for surface normal estimation of dark surfaces. In *Science and Information Conference*, pages 619–637. Springer, 2019.

[73] Mengyu Song, Cong Chen, Tomonari Furukawa, and Azusa Nakata. In-crash toeboard deformation measurement in vehicle crash tests with recursive estimation. *International Journal of Crashworthiness*.

[74] Mengyu Song, Tomonari Furukawa, Boren Li, and Notomi Shinya. A system for measuring microscopic tire wear using hybrid photometric stereo / light section method. In *JSAE*, 2018.

[75] Mengyu Song, Cong Chen, Tomonari Furukawa, Azusa Nakata, and Shinsuke Shibata. A sensor suite for toeboard three-dimensional deformation measurement during crash. *Stapp Car Crash Journal*, 63:331–342, 2019.

[76] Mengyu Song, Cong Chen, Tomonari Furukawa, Azusa Nakata, and Shibata Shinsuke. In-crash toeboard deformation measurement towards active crash control. In *Fast Zero*, 2019.

[77] Mengyu Song, Tomonari Furukawa, and Notomi Shinya. High-resolution circumferential tire tread three-dimensional profiling using laser section method and photometric stereo method. *SAE International Journal of Commercial Vehicles*, 1(1):1–26, 2020.

[78] Misha Sra, Sergio Garrido-Jurado, Chris Schmandt, and Pattie Maes. Procedurally generated virtual reality from 3d reconstructed physical space. In *Proceedings of the 22nd ACM Conference on Virtual Reality Software and Technology*, pages 191–200, 2016.

[79] Tomáš Svoboda, Daniel Martinec, and Tomáš Pajdla. A convenient multicamera self-calibration for virtual environments. *Presence: Teleoperators & virtual environments*, 14(4):407–422, 2005.

[80] Sh Taheri, C Sandu, S Taheri, E Pinto, and D Gorsich. A technical survey on terramechanics models for tire–terrain interaction used in modeling and simulation of wheeled vehicles. *Journal of Terramechanics*, 57:1–22, 2015.

[81] Gabriel Taubin, Daniel Moreno, and Douglas Lanman. 3d scanning for personal 3d printing: build your own desktop 3d scanner. In *ACM SIGGRAPH 2014 Studio*, page 27. ACM, 2014.

[82] Jing Tong, Jin Zhou, Ligang Liu, Zhigeng Pan, and Hao Yan. Scanning 3d full human bodies using kinects. *IEEE transactions on visualization and computer graphics*, 18 (4):643–650, 2012.

[83] Matthew M Torok, Mani Golparvar-Fard, and Kevin B Kochersberger. Image-based automated 3d crack detection for post-disaster building assessment. *Journal of Computing in Civil Engineering*, 28(5):A4014004, 2013.

[84] Adrien Treuille, Aaron Hertzmann, and Steven M Seitz. Example-based stereo with general brdfs. In *European Conference on Computer Vision*, pages 457–469. Springer, 2004.

[85] Nick Van Gestel, Steven Cuypers, Philip Bleys, and Jean-Pierre Kruth. A performance evaluation test for laser line scanners on cmms. *Optics and lasers in engineering*, 47 (3-4):336–342, 2009.

[86] Frank Verbiest and Luc Van Gool. Photometric stereo with coherent outlier handling and confidence estimation. In *2008 IEEE Conference on Computer Vision and Pattern Recognition*, pages 1–8. IEEE, 2008.

[87] João L Vilaça, Jaime C Fonseca, ACM Pinho, and Elisabete Freitas. 3d surface profile

equipment for the characterization of the pavement texture–texscan. *Mechatronics*, 20 (6):674–685, 2010.

[88] Chau-Chang Wang and Dajun Tang. Seafloor roughness measured by a laser line scanner and a conductivity probe. *IEEE Journal of Oceanic Engineering*, 34(4):459–465, 2009.

[89] Jun Wang, Dongxiao Gu, Zeyun Yu, Changbai Tan, and Laishui Zhou. A framework for 3d model reconstruction in reverse engineering. *Computers & Industrial Engineering*, 63(4):1189–1200, 2012.

[90] LiangCai Wang, Wanping Zhang, and Weihu Zhu. Study on profile measurement of extruding tire tread by laser. In *Automated Optical Inspection for Industry*, volume 2899, pages 22–26. International Society for Optics and Photonics, 1996.

[91] M Weiss, S Tsujimoto, and H Yoshinaga. Belt construction optimization for tire weight reduction using the finite element method. *Tire Science and Technology*, 21(2):120–134, 1993.

[92] Robert J Woodham. Photometric method for determining surface orientation from multiple images. *Optical engineering*, 19(1):191139, 1980.

[93] Chenglei Wu, Yebin Liu, Qionghai Dai, and Bennett Wilburn. Fusing multiview and photometric stereo for 3d reconstruction under uncalibrated illumination. *IEEE transactions on visualization and computer graphics*, 17(8):1082–1095, 2010.

[94] Tai-Pang Wu and Chi-Keung Tang. Dense photometric stereo by expectation maximization. In *European Conference on Computer Vision*, pages 159–172. Springer, 2006.

[95] Shihui Ying, Jigen Peng, Shaoyi Du, and Hong Qiao. A scale stretch method based on icp for 3d data registration. *IEEE Transactions on Automation Science and Engineering*, 6(3):559–565, 2009.

[96] Chanki Yu, Yongduek Seo, and Sang Wook Lee. Photometric stereo from maximum feasible lambertian reflections. In *European Conference on Computer Vision*, pages 115–126. Springer, 2010.

[97] X Yu and E Salari. Pavement pothole detection and severity measurement using laser imaging. In *Electro/Information Technology (EIT), 2011 IEEE International Conference on*, pages 1–5. IEEE, 2011.

[98] Xie Zexiao, Wang Jianguo, and Zhang Qiumei. Complete 3d measurement in reverse engineering using a multi-probe system. *International Journal of Machine Tools and Manufacture*, 45(12-13):1474–1486, 2005.

[99] Li Zhang, Brian Curless, and Steven M Seitz. Rapid shape acquisition using color structured light and multi-pass dynamic programming. In *Proceedings. First International Symposium on 3D Data Processing Visualization and Transmission*, pages 24–36. IEEE, 2002.

[100] Zhengyou Zhang. A flexible new technique for camera calibration. *IEEE Transactions on pattern analysis and machine intelligence*, 22, 2000.

# Appendices

# Appendix A

# User Manual for Tire Wear Measurement System

## A.1 System Description

### A.1.1 Mechanical Design

Figure A.1 shows the mechanical design of the tire wear measurement system.

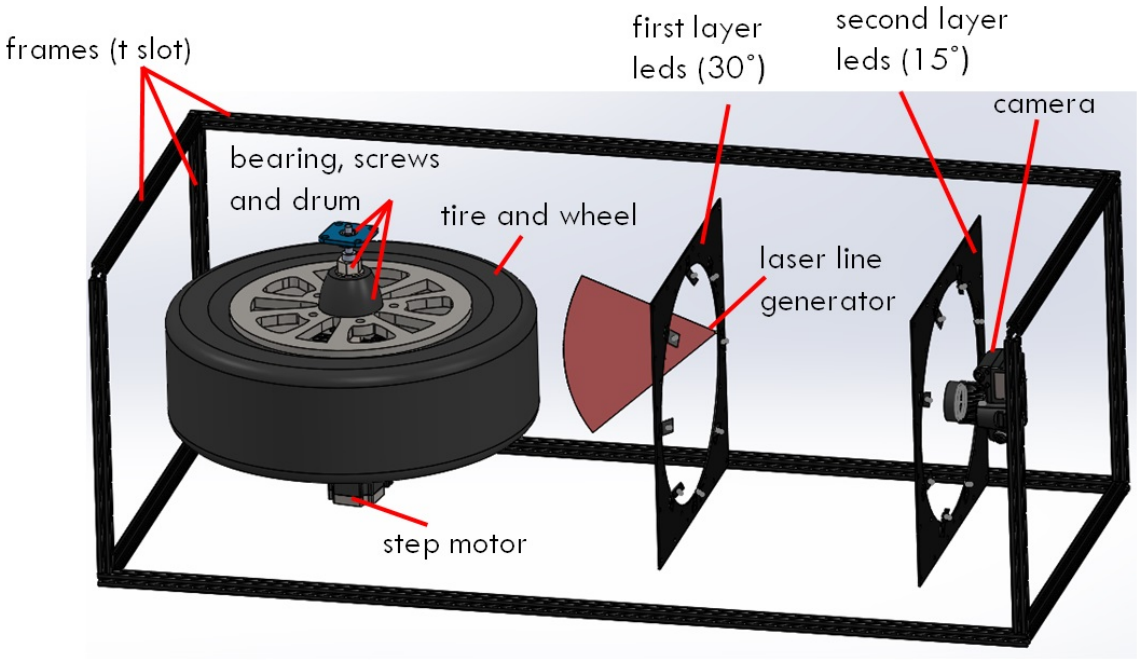


Figure A.1: Mechanical design

The dimension of the system is 1700mm×760mm×610mm (67"×30"×24"). Sigma SD Quattro H is employed in the system, which has a resolution of 7680×5120 pixels. T-slotted aluminum frame is applied in the proposed system, for the purpose of easy-assembly and disassembly. The system is enclosed by black covers, so that the influence of ambient light is minimized. 16 LEDs are distributed in two layers (8 LEDs for 30° illumination and 8 for 15° illumination) to improve the accuracy of photometric stereo. 30° illumination is the optimum lighting direction for regular surface normal measurement using photometric stereo. 15° illumination is utilized to project light into the groove. The tire is mounted to a step motor through a rim and a connector. Two bearings are used to guarantee smooth and stable rotation. The step motor ensures that the wheel can move by a fixed small angle (2.2°) for every rotation. A laser line generator is used to project a red line on the surface of tire. The camera observes the red line from another direction, so that triangulation can be applied to measure the tire surface.

Figure A.2 shows the appearance of the tire wear measurement system with the control panel highlighted. The customized metal cover, which is made by ProtoCase, is used to block ambient light to improve the performance of the system. The system is powered by 110V, which is through a power cable from the top of the system. The control panel, which is on the top of the system next to the power cable, contains 3 pushbuttons and 2 LEDs (green and red). The usage of the pushbuttons and LEDs are introduced in the following section.

### A.1.2 Electrical Design

A micro control unit (MCU, Arduino Mega) is applied here to synchronize the camera, the LEDs, the laser line generator, and the step motor so that the whole system could run

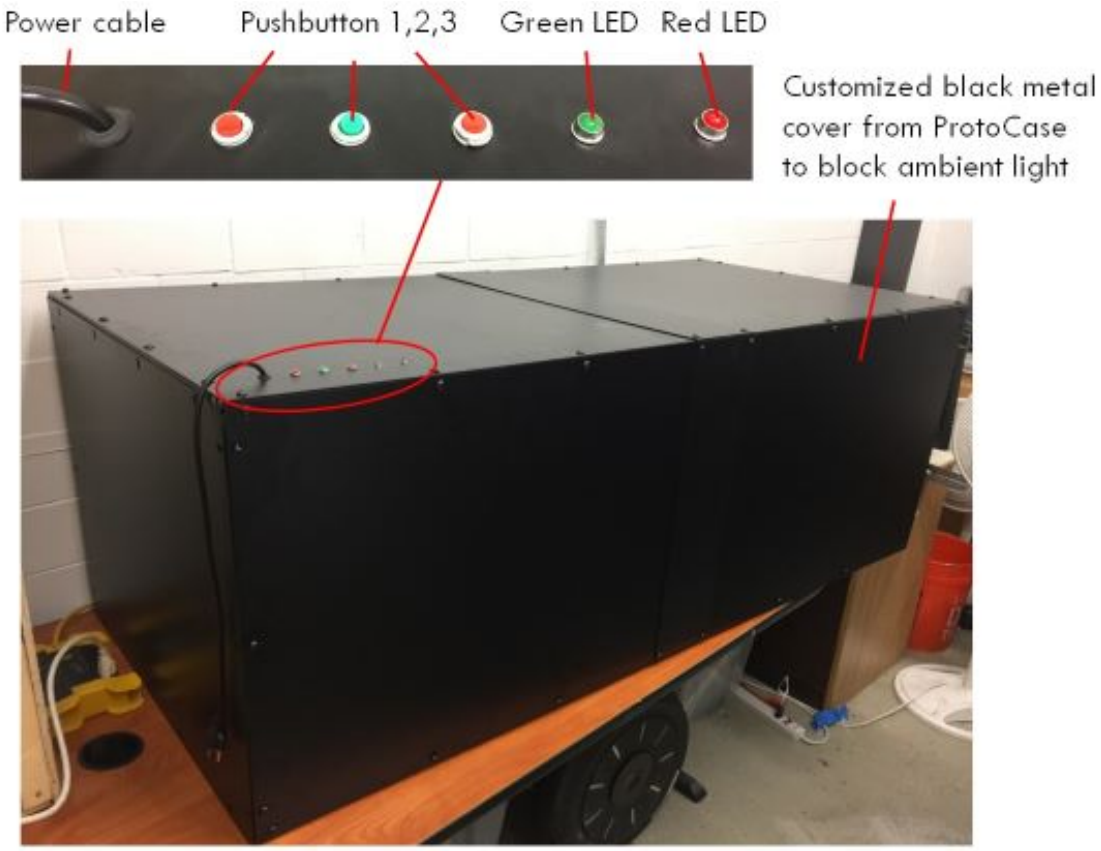


Figure A.2: Tire wear measurement system

autonomously. The pushbuttons are used as inputs for different actions and the LEDs are used as state indicators of the system.

Figure A.3 shows the program diagram of the tire wear system. The two LEDs work as state indicator of the system: green LED on and red LED off indicates the system is READY to use, green LED off and red LED on indicates the system is BUSY. green LED off and red LED off indicates the whole system is OFF. When the system is BUSY or OFF, pressing any pushbutton will do nothing. When the system is READY and one of the pushbutton is pressed, the system will start to take corresponding action, and the system will turn busy until the desired action is done.

Figure A.4(a)∼(c) shows the program diagram for the 3 actions. The first action is a laser

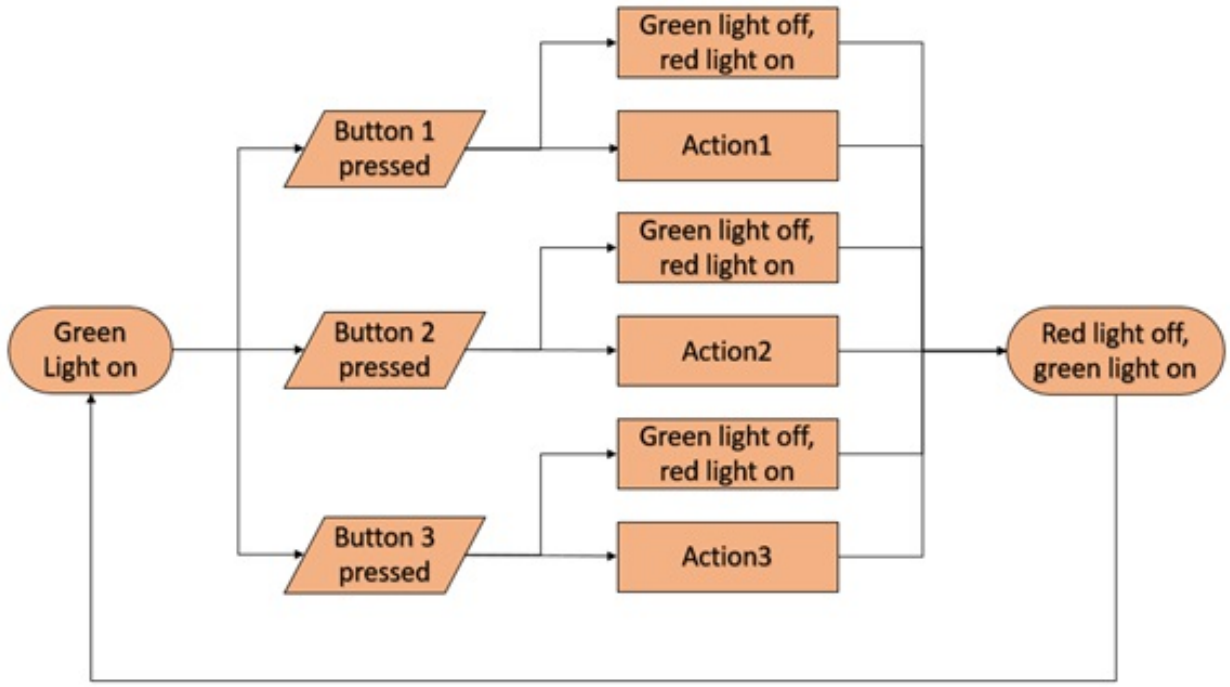


Figure A.3: System program diagram

scanning action. It only turns on laser light first and takes one picture. The second action is a photometric stereo action. It takes pictures with the illumination of LEDs for photometric stereo one by one under only one LED illumination at one time. The third action is a measurement action. It first takes 360° Laser Section (LS) measurement and then takes 360° Photometric Stereo (PS) measurement.

As shown in the figure, pushbotton 1 is for one LS measurement while pushbotton 2 is for one PS measurement. These two buttons are mainly used for calibration. Pushbotton 3, on the other hand, when pressed will trigger the whole tire measurement.

### A.1.3 Camera Setting

The Camera used for the system is Sigma SD Quattro H, with a resolution of 7680×5120 pixels (Figure A.5(a)). The lens for this project is Sigma 18-250mm f/3.5-6.3 DC Macro OS

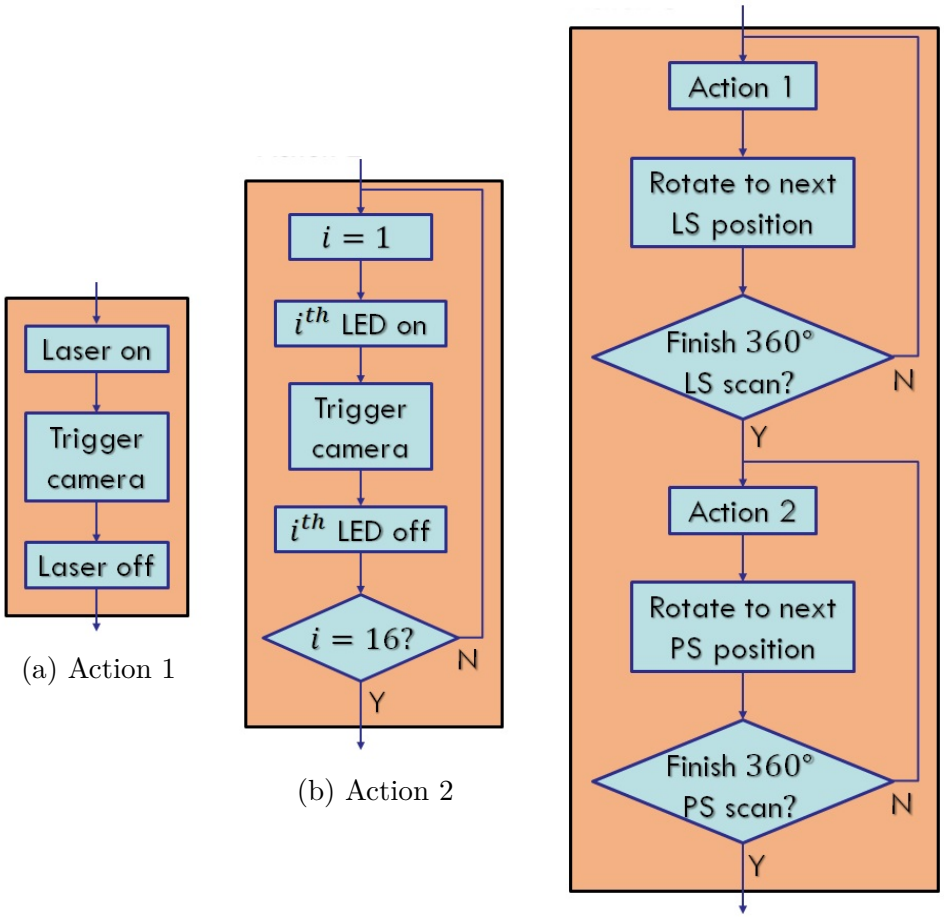


(a) Action 1

(b) Action 2

(c) Action 3

Figure A.4: Action diagram

HSM (Figure A.5(b)). The reason to choose a wide range camera is to encounter all kinds of situation. The parameter of camera chosen for this project is: ISO-1600, f/6.3, 1.3s exposure time, 62mm focal length.


(a) Sigma SD Quattro H

(b) Sigma 18-250mm f/3.5-6.3 DC Macro OS HSM

Figure A.5: Camera and lens

## A.2 Operation Instruction

### A.2.1 Remove and Place Tire

Figure explains the structure for removing and placing tire.

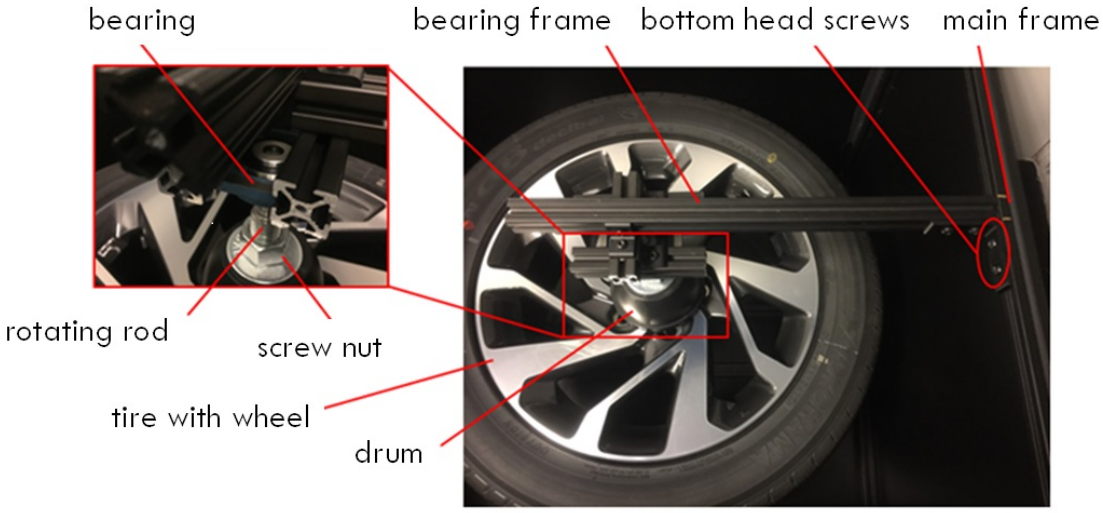


Figure A.6: Remove and Place Tire

The operation steps to remove a tire from the proposed system are described as following:

1. Remove the two bottom head screws that connecting the bearing frame and main

frame.

2. Remove the bearing from the rotating rod with the bearing frame.

3. Remove the screw nut from the rotating rod.

4. Remove the drum from the rotating rod.

5. Remove the tire from the rotating rod with the wheel.

The operation steps to place a tire on the proposed system are reverse of the operation steps to remove a tire:

1. Place the tire on the rotating rod, try to make the tire as level as possible.

2. Place the drum through the rotating rod on the top of the wheel.

3. Insert the end of the rotating rod through the bearing hole.

4. Fasten the screw nut towards rotating rod until the wheel is tightly connected to the rotating rod.

5. Use the two bottom head screws to connect the bearing frame and main frame.

### A.2.2 Camera and Laser Calibration

The details of camera and laser calibration are introduced in this section. 30 images are used for camera and laser calibration. The total time for collecting this 30 images is about 20 minutes. The operation steps are described as following:

1. Place the tire which need to be measured on the rotation rod.

2. Adjust the zoom ring (Figure A.7(a)), so that the tire will take the 2/3 to 3/4 of the image.

3. Adjust the focus ring, so that the tire surface is clear in the image.

4. Adjust the calibration board holder (Figure A.7(b)) to an appropriate pose, then put checkerboard (Figure A.7(c)) for camera and laser on the calibration board holder.

5. Close the covers of the system, to make the inside of the system completely dark.

6. Press pushbutton 1, wait till the green light turned on again.

7. Repeat 4-6 for 30 times.


(a) Lens


(b) Position of calibration board holder

(c) Checkerboard

Figure A.7: Camera and laser calibration

### A.2.3 Light Position Calibration

The details of light position calibration are introduced in this section. 1 figure of reference plane will be captured, along with 1 set of photometric stereo figures. In total, 17 images are

obtained, and the total time for collecting this 17 images is about 3 minutes. The operation steps are described as following:

1. Adjust the calibration board holder to a place so that the board on it will be leveled and as close to the tire surface as possible.
2. Put checkerboard on the calibration board holder.
3. Press pushbutton 1, wait till the green light turned on again.
4. Remove the checkerboard, place the ball board (Figure A.8) on calibration board holder.
5. Close the covers of the system, to make the inside of the system completely dark.
6. Press pushbutton 2, wait till the green light turned on again.

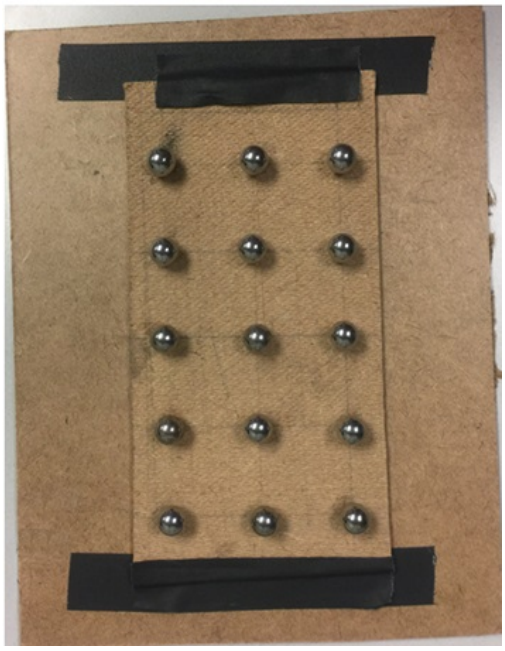

Figure A.8: Ball board

### A.2.4 Light Illumination Calibration

The details of light illumination calibration are introduced in this section. 1 figure of reference plane is captured, along with 1 set of photometric stereo figures. In total, 17 images are obtained, and total time for collecting this 17 images is about 3 minutes. The operation steps are described as following:

1. Adjust the calibration board holder to a place so that the board on it will be leveled and as close to the tire surface as possible.
2. Put checkerboard on the calibration board holder.
3. Press pushbutton 1, wait till the green light turned on again.
4. Remove the checkerboard, place the whiteboard (Figure A.9) on calibration board holder.
5. Close the covers of the system, to make the inside of the system completely dark.
6. Press pushbutton 2, wait till the green light turned on again.

### A.2.5 Start Measurement

The whole tire measurement data collection takes about 1.5 hours. The operation steps to start the measurement are described as following:

1. Place the tire in the system.
2. Close the covers of the system, to make the inside of the system completely dark.
3. Press pushbutton 3, wait till the green light turned on again.

Figure A.9: Whiteboard

## A.3 Data Processing

Figure A.10 shows the customized user interface of the data processing procedure of the tire wear measurement system. The data processing procedure is written in Matlab. To make it easy to use, even for users who are not familiar with Matlab, the user interface uses only buttons to set parameters, run programs and generate results. The main interface is started automatically by default. By clicking any button in the interface, the program will open another interface, or open a pop-up window for parameter setting, or execute a certain data processing step. To make the system easy to maintain and update, the program adapts a modularized manner.

The intermediate processed data and output images and results are automatically stored in the result folder for easy analysis, as shown in Figure A.11.

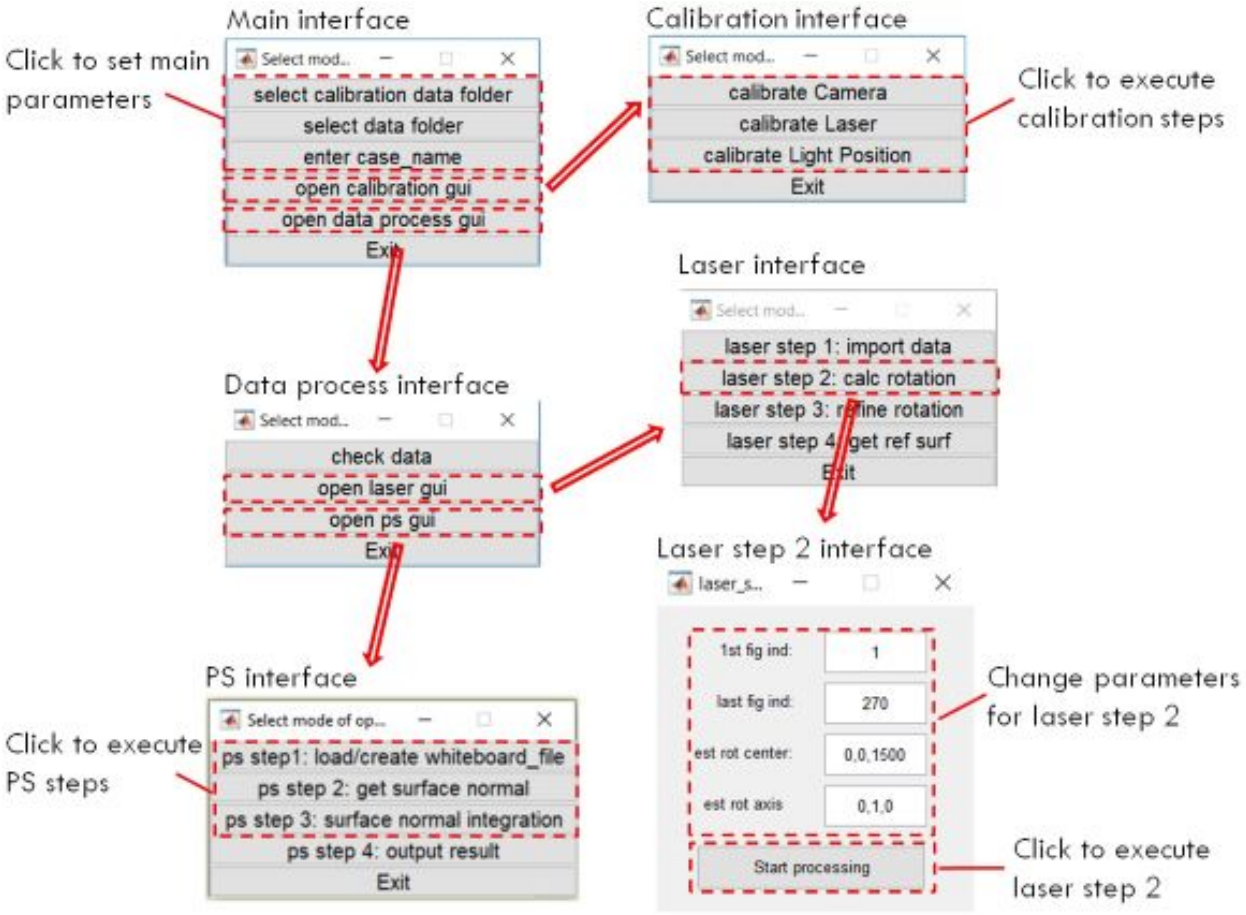


Figure A.10: Data processing user interface

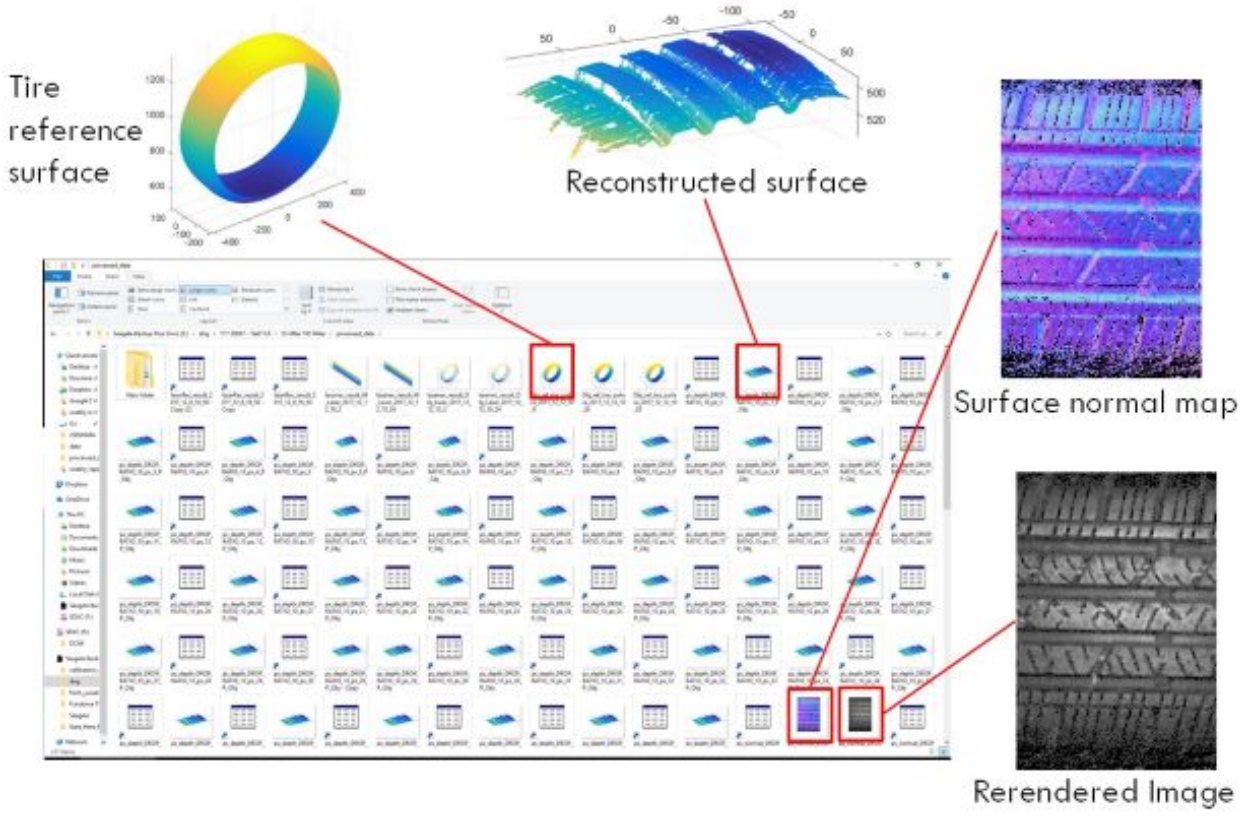


Figure A.11: Result folder